



Attribution–NonCommercial–NoDerivs 2.0 KOREA

You are free to :

- **Share** — copy and redistribute the material in any medium or format

Under the following terms :



Attribution — You must give [appropriate credit](#), provide a link to the license, and [indicate if changes were made](#). You may do so in any reasonable manner, but not in any way that suggests the licensor endorses you or your use.



NonCommercial — You may not use the material for [commercial purposes](#).



NoDerivatives — If you [remix, transform, or build upon](#) the material, you may not distribute the modified material.

You do not have to comply with the license for elements of the material in the public domain or where your use is permitted by an applicable exception or limitation.

This is a human-readable summary of (and not a substitute for) the [license](#).

[Disclaimer](#) 

Doctoral Thesis

**Synthesis of Multifunctional Two-Dimensional
Structures and Their Applications**

Javeed Mahmood

Department of Energy Engineering

Graduate School of UNIST

2015

Synthesis of Multifunctional Two-Dimensional Structures and Their Applications

Javeed Mahmood

Department of Energy Engineering

Graduate School of UNIST

Synthesis of Multifunctional Two-Dimensional Structures and Their Applications

A thesis/dissertation
submitted to the Graduate School of UNIST
in partial fulfillment of the
requirements for the degree of
Doctor of Philosophy

Javeed Mahmood

07. 06. 2015

Approved by



Advisor

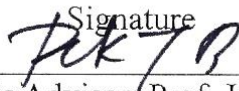
Jong-Beom Baek

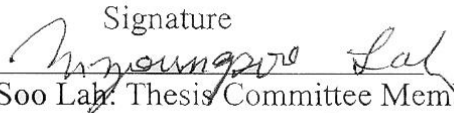
Synthesis of Multifunctional Two-Dimensional Structures and Their Applications

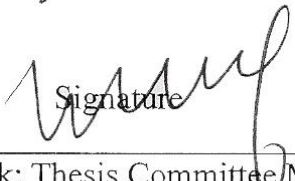
Javeed Mahmood


This certifies that the thesis of Javeed Mahmood is approved.


07. 06. 2015

Signature

Thesis Advisor: Prof. Jong-Beom Baek

Signature

Prof. Myoung Soo Lah: Thesis Committee Member #1

Signature

Prof. Noejung Park: Thesis Committee Member #2

Signature

Prof. Hyung-Joon Shin: Thesis Committee Member #3

Signature

Prof. Joon Hak Oh: Thesis Committee Member #4;

Abstract

Two dimensional (2D) materials with uniformly decorated heteroatoms represent a huge challenge and aroused immense interest beyond graphene due to their exceptional electronic and optoelectronic properties. The most widely studied 2D materials graphene and hexagonal boron nitride (*h*-BN) are the monoatomic layered materials with similar geometry and quite different electronic structure and properties. Graphene is metallic due to extremely high carrier mobility and *h*-BN is wide band gap insulator, which limits their potential application in electronics. Despite recent explorations in materials science, an easy and scalable way to produce uniformly doped 2D materials are limited. To overcome these problems, I first designed and synthesized a suitable monomer, hexaaminobenzene (HAB) hydrochloride, for the first time in crystalline form by using an easy procedure. The needle like crystal structure of the HAB hydrochlorides was confirmed by single crystal X-ray diffraction study. HAB was further used to fabricate a new layered 2D network structure with uniformly distributed holes and nitrogen atoms and the overall stoichiometry is thought to be C_2N . The 2D structure can be efficiently prepared by simple wet-chemical reaction from the logically designed monomers. The structure of the C_2N was confirmed by scanning tunneling microscopy (STM) and the calculated and experimental band-gaps are in the semiconductor region about 1.7 and 2.0 eV, suggesting a clear advantage over conducting graphene and insulating *h*-BN. I synthesized another 2D structure with C_3N stoichiometry with uniformly placed nitrogen atoms in the carbon framework by carbonization of hexaaminobenzene hydrochloride single crystal at 500 °C. The topological and electronic structure of the C_3N 2D structure was studied by scanning tunneling microscopy. C_3N structure could be a new class of 2D materials with novel properties that can be emerged from the unique structure. C_2N structure was used to encapsulate iron particles by *in situ* reducing and subsequent annealing to give $Fe@C_2N-h2D$. $Fe@C_2N-h2D$ material shows interesting oxygen reduction reaction ability both in acid and alkaline solution. C_2N structure was also used to encapsulate cobalt oxide by the same way for catalytic hydrogen evolution from the sodium borohydride solution. $Co@C_2N$ shows outstanding property of hydrogen evolution compared to the pure metal catalysts. Moreover, I also designed and synthesized organic conjugated triazine polymer demonstrating room temperature ferromagnetism derived from purely organic compounds. The polymer was synthesized through self-polymerization of tetracyanoquinodimethane (TCNQ). Electron spin resonance and magnetic characterization revealed the presence of spin $\frac{1}{2}$ moments, which partially lead to ferromagnetic ordering with a critical temperature that is higher than room temperature.

Table of Contents

Abstract	I
Table of Contents	II
List of Figures	V
List of Tables	XIII
Abbreviations	XIV
I. Large-Scale Synthesis of Pure and Stable Hexaaminobenzene Trihydrochloride	1
1.1 Abstract.....	1
1.2 Introduction.....	1
1.3 Materials and Instrumentation	2
1.4 Synthesis of 2,4,6-trinitroaniline (TNA, 1).....	2
1.5 Synthesis of 1,3,5-triamino-2,4,6-trinitrobenzene (TATB, 2)	2
1.6 Synthesis of hexaaminobenzene trihydrochloride (HAB, 3)	3
1.7 Single crystal X-ray diffraction study	4
1.8 Results and Discussion.....	5
1.9 Conclusions.....	7
1.10 References.....	8
II. C₂N holey two-dimensional crystal	11
2.1 Abstract.....	11
2.2 Introduction.....	11
2.3 Materials	12
2.4 Instrumentation	12
2.5 Synthesis of the C ₂ N- <i>h</i> 2D crystal (nitrogen containing holey 2D crystal)	12
2.6 C ₂ N- <i>h</i> 2D crystal as a heterogeneous catalyst (Model reaction).....	13
2.7 First-principle calculations.....	13

2.8 STM experiments.....	13
2.9 Results and Discussion.....	13
2.10 Conclusions.....	36
2.11 References.....	36
III. C₃N 2D structure from carbonized single crystal.....	40
3.1 Abstract.....	40
3.2 Introduction.....	40
3.3 Materials & Instrumentations.....	41
3.4 Synthesis of carbonized single crystal rods (C ₃ N framework)	41
3.5 Measurement of HOMO and LUMO gap	41
3.6 Results and Discussion.....	42
3.7 Conclusions.....	59
3.8 References.....	59
IV. Fe-Cocooned C₂N-<i>h</i>2D Structures as Efficient Oxygen Reduction Catalysts.....	62
4.1 Abstract.....	62
4.2 Introduction.....	62
4.3 Materials	63
4.4 Instrumentation	63
4.5 Synthesis of the iron containing holey 2D crystal (Fe@C ₂ N- <i>h</i> 2D)	63
4.6 Cyclic voltammogram.....	64
4.7 Results and Discussion.....	64
4.8 Conclusions.....	76
4.9 References.....	77
V. C₂N-<i>h</i>2D polymer encapsulated cobalt oxide catalyst for hydrogen evolution	80
5.1 Abstract.....	80
5.2 Introduction.....	80
5.3 Materials	81

5.4 Instrumentation	81
5.5 Synthesis of Co@C ₂ N.....	82
5.6 Catalyst test.....	82
5.7 Catalytic reduction reaction	82
5.8 Results and discussion	82
5.9 Conclusions.....	89
5.10 References.....	89
VI. Organic Ferromagnetism from Self-Polymerized TCNQ.....	93
6.1 Abstract:.....	93
6.2 Introduction.....	93
6.3 Materials & Instrumentations.....	93
6.4 Self-Polymerization of 7,7,8,8-tetracyanoquinodimethane (TCNQ).....	94
6.5 Electron spin resonance (ESR) measurements.....	94
6.6 Results and discussion	94
6.7 Conclusions.....	109
6.8 References.....	109
Acknowledgement	111
List of publications.....	113

List of Figures

Figure 1.1. Photograph of crystallized HAB after filtration through Celite and washing with aqueous HCl (0.5M) solution.

Figure 1.2. (a) Digital photograph of the TATB, (b) image of the HAB crystals as one of the best secured samples from reported catalytic reduction of TATB in the presence of H₂ and platinum (10 wt%) on activated carbon (Pd-C),³ (c) HAB trihydrochloride crystal procured from the reduction of TATB in the presence of SnCl₂/HCl system.⁴

Figure 1.3. The synthesis of hexaaminobenzene (HAB) trihydrochloride

Figure 1.4. Mesomerism of TATB in DMSO

Figure 1.5. (a) Digital photograph of HAB trihydrochloride crystals on PTFE filter membrane; (b, c) optical microscopic images of the HAB trihydrochloride crystals; (d) digital photograph of HAB in vial after one year; (e) formula unit of the HAB trihydrochloride; (f) hydrogen-bonding driven molecular packing into the needle-like crystal structure.

Figure 2.1. Schematic presentation of the difference among two-dimensional structures: (a) Graphene (1st generation); (b) Holey graphene (2nd generation, not yet been realized); (c) Holey nitrogenated graphene (3rd generation, designated as C₂N-*h*2D crystal). The synthesis of the C₂N-*h*2D crystal: (d) Hexaaminobenzene (HAB) trihydrochloride. Inset is a polarized optical microscope image of the HAB single crystal; (e) Hexaketocyclohexane (HKH) octahydrate. Digital photographs: (f) as-prepared C₂N-*h*2D crystal; (g) Solution-cast C₂N-*h*2D crystal on SiO₂ surface and heat-treated at 700 °C; (h) Transferred C₂N-*h*2D crystal film (thickness: ~ 330 nm) on PET substrate. Metallic shiny reflection indicates high crystallinity.

Figure 2.2. Schematic presentation for the formation of the C₂N-*h*2D crystal with edge groups and thermodynamics of reaction. Reaction enthalpy (ΔH), calculated with the PBE density functional theory, is found to be -89.7 kcal/unit mol. After heat-treatment, bound small molecules (H₂O, O₂, and etc.) and edge groups from structure 1 could be thermally stripped off to give the heat-treated C₂N holey structure 2.

Figure 2.3. Solubility of the C₂N-*h*2D crystal in various solvents: (a) After 30s. (b) After 1 week. (1) water; (2) acetic acid; (3) MeOH; (4) 1M HCl; (5) NMP; (6) DMF; (7) DMSO; (8) DMAc; (9) acetone; (10) toluene; (11) THF; (12) 1M NaOH; (13) benzene; (14) dichlorobenzene.

Figure 2.4. Analysis of the as-prepared C₂N-*h*2D crystal: (a) Powder XRD pattern from the as-prepared sample; (b) XPS survey spectrum showing C1s, N1s and O1s. High resolution XPS spectra

for C1s, N1s and O1s are presented in Fig. S3. TGA thermograms obtained with a heating rate of 10 °C/min in air and argon: (c) As-prepared sample; (d) Heat-treated sample at 700 °C.

Figure 2.5. Deconvoluted XPS spectra of the C₂N-*h*2D crystal: (a) C 1s. (b) N 1s. (c) O 1s.

Figure 2.6. XPS survey spectrum of the heat-treated C₂N-*h*2D crystal at 700 °C, showing C 1s, N 1s and reduced O1s compared with as-prepared spectrum (Figure 2.4b).

Figure 2.7. SEM images of the C₂N-*h*2D crystal: (a) As-prepared sample. (b) Heat-treated flakes. (c) Edge-on view of heat-treated flakes. TEM images of the C₂N-*h*2D crystal: (d) At low-magnification. (e) At high-magnification. (f) The interlayer distance ($d = 0.327$ nm) estimated along the dark green line in (e). The interlayer distance of 0.327 nm is very close to that obtained from XRD pattern (0.328 nm, Fig. 4a).

Figure 2.8. Energy-filtered TEM images of the as-prepared C₂N-*h*2D crystal: (a) Zero-loss image. (b) Carbon mapping. (c) Nitrogen mapping. (d) Oxygen mapping. (e) Energy dispersive X-ray spectroscopy (EDX) spectrum showing the elemental composition (C, N and O) from the TEM image (a). (f) Electron energy loss spectroscopy (EELS) spectrum from the TEM image (a). Respective values of carbon, nitrogen and oxygen contents are very close to theoretical values.

Figure 2.9. SEM images obtained from cross-section of the C₂N-*h*2D crystal films on SiO₂(300 nm)/Si wafer with different thickness: (a) 330. (b) 370. (c) 290. (d) 80 nm.

Figure 2.10. Atomic-resolution imaging of C₂N-*h*2D crystal: (a) An STM topography image of C₂N-*h*2D on Cu(111); (b) Theoretically calculated image; (c) Topographic height profile along the sky blue line marked in (A); (d) 2D fast Fourier Transformation of (a). The STM image was obtained at the sample bias of 0.7 V, and the tunneling current of 300 pA. The scale bars in (a), (b) and (d) are 1.6, 1.9 nm and 1.9 nm⁻¹, respectively.

Figure 2.11. Comparison of interlayer distances: (a) Graphite. (b) *h*-BN. (c) C₂N-*h*2D crystal. Due to the differences in atomic sizes (covalent radii, B = 85, C = 77, N = 70 picometers), stacking patterns and charge polarizations, graphite and *h*-BN have very similar interlayer distance of 3.35 Å, while the C₂N-*h*2D crystal has lower interlayer distance (3.28 Å). Structures of representative single layer 2D crystals: (d) Graphene. (e) *h*-BN. (f) C₂N-*h*2D crystal.

Figure 2.12. (a) Optical band-gap calculation and the absorbance squared vs. photon energy ($h\nu$) extrapolated to zero absorption. Inset is UV absorption curve. (b) Cyclic voltammograms of the C₂N-*h*2D crystal at a scan rate of 100 mVs⁻¹ using Ag/Ag⁺ reference electrode. (c) The band structure from the zone center to the X point of the 2-D triangular lattice. (d) The density of electronic states. An iso-

surface plot of the Kohn-Sham orbital at the Gamma point: (e) Conduction band minimum state; (f) The doubly degenerate valence band maximum state.

Figure 2.13. Cyclic voltammograms (CV) of the C₂N-*h*2D crystal on GC electrode at a scan rate of 100 mV s⁻¹ using an Ag/Ag⁺ reference electrode under N₂ atmosphere: (a) Whole range curve, showing no oxidation peak for the C₂N-*h*2D crystal. (b) C₂N-*h*2D crystal in the presence of ferrocene, which was used as reference material.

Figure 2.14. Schematic illustration for the film fabrication of the C₂N-*h*2D crystal using a PDMS mold: (a) 3–7 μL of the C₂N-*h*2D crystal solution was drop-coated onto the SiO₂/Si wafer using pipette. (b) The solution was slowly dried. (c) After cooling the sample to room temperature, the sample was annealed at 700 °C for 2 hours under argon atmosphere. (d) PDMS precursor was poured onto the sample film on SiO₂/Si wafer. (e) After curing the PDMS, which was carefully detached from the SiO₂/Si wafer. (f) Film attached to the PDMS after removing SiO₂/Si substrate is shown in the photograph (cyan blue square). Now the film can be transferred to any other desired substrate like SiO₂/Si wafer for device study. The scale bar is 1 cm.

Figure 2.15. Optical images of the C₂N-*h*2D crystals on a SiO₂/Si wafer: (a) The C₂N-*h*2D crystal can be obtained over micron scale size. (b) The C₂N-*h*2D crystal is flexible (folded, cyan blue area). (c) Two C₂N-*h*2D crystal flakes have crossed (cyan blue area). All scale bars are 70 μm.

Figure 2.16. FET device study: (a) AFM image of the C₂N-*h*2D crystal; the scale bar is 7 μm. The height profile (deep-blue line) was obtained along the dark-blue line. (b) Optical microscopy image of a C₂N-*h*2D crystal field-effect transistor (FET) prepared on a SiO₂(300 nm)/n⁺⁺ Si wafer. The channel length (*L*) of the device is 500 nm, and the channel width-to-length (*W/L*) = 13. The inset is an optical microscopy image taken prior to the deposition of Au electrodes on the crystal. The scale bars are 60 μm. (c) Transfer curves of the C₂N-*h*2D crystal FET devices measured at 25 °C under 5 × 10⁻⁶ torr (*V*_{DS} = -30 V).

Figure 2.17. (a) Output curve after annealing at 100 °C under 5 × 10⁻⁶ torr (*V*_{DS} = -30 V). (b) Transfer curve of the C₂N-*h*2D crystal field-effect transistor before annealing. The characterization was performed at 25 °C under 5 × 10⁻⁶ torr.

Figure 2.18. Energy level diagram of the C₂N-*h*2D crystal FET. The *p*-type operation of the FET is favorable with gold electrode according to the energy level diagram. ^a Work function.

Figure 2.19. Photographs: (a) Heat-treated C₂N-*h*2D crystal at 700 °C. (b) As-compressed C₂N-*h*2D crystal pellet by approximately 9000 bars. Inset is side-view of the pallet. (c) After annealing at 700 °C. (d) Graphite ore (http://en.wikipedia.org/wiki/Graphite#cite_note-3). (e) Silicon ore (<http://images-of->

elements.com/silicon.php). (f) Germanium ore (<http://images-of-elements.com/germanium.php>). All cases are showing the surface in the shiny reflected light.

Figure 2.20. Schematic presentation of Knoevenagel condensation reaction of terephthalaldehyde and malononitrile in the presence of the C_2N -*h*2D crystal as a reaction catalyst.

Figure 3.1. Schematic representation of C_3N formation. (a), Single-crystal x-ray packing structure of HAB (1) and schematic representation of the spontaneous transformation of HAB into the 2D C_3N crystal (2, 3, 4); (b), digital photograph of HAB crystals on butter paper; c, optical microscopy image of a needle-like HAB crystal before annealing; (d), SEM image of an HAB single crystal; e, digital image of HAB after annealing at 500 °C; (f), optical microscopy image of HAB crystals after annealing at 500 °C; (g), SEM image of a 2D C_3N single crystal.

Figure 3.2. Single crystal structure of HAB: (a), formula unit; (b), hydrogen-bonded three layers of HAB crystal; (c), hydrogen-bonded packing a-direction view in (b); (d), hydrogen-bonded packing b-direction view in (b); (e), hydrogen-bonded packing c-direction view in (b).

Figure 3.3. Characterisation of the C_3N structure: (a), TGA thermogram of an HAB single crystal with a ramping rate of 10 °C/min; (b), TGA thermogram of a 2D C_3N crystal after annealing at 500 °C; (c), solid-state ^{13}C magic-angle spinning (MAS) NMR spectrum of C_3N crystals; (d), XPS survey spectrum of C_3N crystals. High-resolution XPS spectra are presented in Figure 3.4.

Figure 3.4. High-resolution XPS spectra of C_3N framework: (a), C 1s; (b), N 1s; (c), O 1s.

Figure 3.5. Mechanistic presentation of the C_3N framework with edge groups.

Figure 3.6. (a), Before addition of $AgNO_3$ to the sample; (b), after addition of $AgNO_3$, white precipitation appeared, indicating the presence of chloride ion $HAB + HNO_3 + AgNO_3 \rightarrow AgCl$ (white precipitation in water); (c), Mixture of HAB and NaOH, before heating; (d), after heating the mixture, pH paper at the mouth of the test tube turn deep green, showing the release of ammonia as follow: $NH_4^+Cl^- + Na^+OH^- \rightarrow NaCl + H_2O + NH_3$.

Figure 3.7. SEM images of the pure HAB crystals show well define hexagonal rod like framework from different crystals.

Figure 3.8. SEM energy dispersive X-ray spectroscopy (EDS) showing the elemental composition of the hexaaminobenzene hydrochloride (HAB) (C, Cl, N and O) from the corresponding SEM image.

Figure 3.9. SEM images of the C_3N framework at different magnification showing the stacked layers and the prominent hexagonal rod like morphology is well maintained after annealing at 500 °C.

Figure 3.10. SEM energy dispersive X-ray spectroscopy (EDS) showing the elemental composition of the C_3N frame work (C, N and O) from the corresponding SEM image, showing no chloride peak in the EDS spectrum.

Figure 3.11. STM and theoretical studies of the C_3N structure. (a), STM image of a C_3N crystal ($2.5 \times 2.5 \text{ nm}^2$, $V_s = -1.1 \text{ V}$, $I_t = 1.0 \text{ nA}$); (b), topographic height profile along the white line marked in (a); (c), differential conductance (dI/dV) spectrum of a C_3N crystal; (d), simulated STM image; (e), electronic band structure; (f), PDOS of the carbon (dark-red) and nitrogen (dark-green) atoms.

Figure 3.12. Cyclic voltammograms in acetonitrile containing 0.1 M TBAPF₆: (a), C_3N crystal; (b), C_3N crystal with ferrocene; (c), Pure HAB crystals were also tried to measure the band gap by electrochemically, but HAB molecules are unstable in the electrochemical test condition. It decomposes during the process, so it was not possible to determine HOMO-LUMO by electrochemical method.

Figure 4.1. (a) Schematic presentation of the $Fe@C_2N-h2D$ synthesis; (b) behavior of the $Fe@C_2N-h2D$ in the magnetic field. $Fe@C_2N-h2D$ in vial without magnetic field (left); $Fe@C_2N-h2D$ in vial with magnetic field (right), showing attraction of black $Fe@C_2N-h2D$ particles toward magnet and the particles are accumulated on the side of the glass wall (The image taken from the video clip in Supporting Information); (c) SEM image of $Fe@C_2N-h2D$; (d) low-magnification of HR-TEM image; (e) high-magnification of HR-TEM image, showing the encapsulated Fe nanoparticles. Inset is selected-area electron diffraction (SAED) pattern.

Figure 4.2. $Fe@C_2N-h2D$ energy dispersive X-ray spectroscopy (EDS) spectrum showing the elemental mapping and compositing (C, N, O and Fe) from the SEM image.

Figure 4.3. (a) XPS survey spectrum showing C1s, Fe 2p, N1s and O1s. Deconvoluted XPS spectra of $Fe@C_2N-h2D$ (b) C 1s; (c) N 1s; (d) Fe 2p.

Figure 4.4. XPS and XRD of the $Fe@C_2N-h2D$ samples: (a) Survey XPS spectrum with the inset Fe deconvoluted spectrum; (b) Powder XRD from the $Fe@C_2N-h2D$ in comparison with the simulated Fe_3C XRD.

Figure 4.5. (a,c) HR-TEM images of as-prepared $Fe@C_2N-h2D$; (b) inter layer distance from the red marked line; (d) lattice distance from the Fe nanoparticles from the marked distance.

Figure 4.6. Nitrogen adsorption and desorption isotherm for the $Fe@C_2N-h2D$. The Brunauer-Emmett-Teller (BET) specific surface area is approximately $84.02 \text{ m}^2\text{g}^{-1}$ which is apparently low. The nitrogen adsorption-desorption isotherms exhibit a hysteresis loop of type H4 indicating the presence of slit like pores between the layers.

Figure 4.7. Cyclic voltammograms of Pt/C and Fe@C₂N-h2D in 1 M aq. KOH solution: (a) in oxygen-saturated and (b) in nitrogen-saturated conditions. Polarization curves on a glassy carbon RDE voltammograms for Pt/C and Fe@C₂N-h2D in O₂-saturated 0.1 M aq KOH solution with a scan rate of 0.01 V s⁻¹ at different rotating rates of 600, 900, 1200, 1600, 2000, and 2500 rpm: (c) the Pt/C; (d) Fe@C₂N-h2D. Koutecky-Levich plots for the Fe@C₂N-h2D (inset in c) and Pt/C (inset in d) electrodes at -0.6 V.

Figure 4.8. Cyclic stability of the samples before and after 200 cycles in 1 M aq. KOH solution: (a) Fe@C₂N-h2D in nitrogen condition (b) Pt/C in nitrogen saturated atmosphere (c) Fe@C₂N-h2D in oxygen saturated condition (d) Pt/C in oxygen saturated environment.

Figure 4.9. Cyclic stability of the samples before and after 200 cycles in 1 M aq. H₂SO₄ solution: (a) Fe@C₂N-h2D in nitrogen condition (b) Pt/C in nitrogen saturated atmosphere (c) Fe@C₂N-h2D in oxygen saturated condition (d) Pt/C in oxygen saturated environment.

Figure 4.10. Stability test of the Fe@C₂N-h2D in H₂SO₄ and KOH both in oxygen and nitrogen atmosphere after 10,000 cycles.

Figure 4.11. Stability of the Fe@C₂N-h2D material, capacitance retention after 10,000 cycles.

Figure 4.12. Stability and methanol crossover effect of Pt/C and Fe@C₂N-h2D in oxygen saturated 0.1 M aq. KOH solution: (a) capacity retention as a function of cycle number of 10,000 cycles; (b) methanol tolerance.

Figure 4.13. (a), Displays hysteresis loop of the sample measured at 5 K and 300K. (b), the blocking temperature (T_b) measured at $H = 1000$ Oe was ~ 370 K.

Figure 5.1. (a) Schematic presentation of the Co@C₂N synthesis; (b) the behavior of Co@C₂N in the magnetic field. Co@C₂N in a vial without magnetic field (left); Co@C₂N in the vial with magnetic field (right), revealing magnetic attraction of the black Co@C₂N particles toward magnet and the material is accumulated on the side of the glass wall; (c) SEM image of the Co@C₂N; (d) low-magnification HR-TEM image; (e) high magnification HR-TEM image, disclosing the C₂N polymer encapsulated Co nanoparticles.

Figure 5.2. Co@C₂N energy dispersive X-ray spectroscopy (EDS) showing the elemental mapping and composition (C, N, O and Co) from the SEM image.

Figure 5.3. TGA from the Co@C₂N in air and nitrogen atmosphere.

Figure 5.4. (a) XPS survey spectrum of Co@C₂N showing C1s, Co 2p, N1s and O1s. Deconvoluted spectra of Co@C₂N (b) C1s; (c) N1s; (d) Co 2p.

Figure 5.5. XPS and HP-XRD of the Co@C₂N material. (a) Survey XPS spectrum with the inset Co deconvoluted spectrum; (b) Powder XRD pattern from the Co@C₂N material.

Figure 5.6. Catalytic hydrogen generation of Co@C₂N. (a) Hydrogen generation rate for Co@C₂N at different temperature; (b) Corresponding Arrhenius plot obtained from the data in a.

Figure 5.7. (a) Stability test of Co@C₂N during catalysis at 303 K. (b) Nitrogen absorption and desorption isotherm for Co@C₂N.

Figure 6.1. (a) Schematic presentation of the TCNQ framework with edge groups after aqueous quenching; (b) TCNQ dissolved in TFMSA after stirring at room temperature before self-polymerization; (c) complete gelation of the reaction mixture after polymerization at 155 °C overnight.

Figure 6.2. XPS survey spectrum from the *p*-TCNQ.

Figure 6.3. (a) Schematic representation of the radical formation and its stability in the structure.; (b) solid-state ESR spectrum of the sample under ambient conditions, showing an isotropic singlet; and (c) solid-state NMR revealing the presence of an unusual peak at 40.93 ppm, which is associated with the tertiary radical in the structure (indicated in the inset by a black dot).

Figure 6.4. (a) TGA graph in inert (N₂) and air atmosphere; (b) powder XRD spectrum exhibiting a broad peak centered at $2\theta = 24.9^\circ$, implying the amorphous 3D nature of the material.

Figure 6.5. SEM images from the *p*-TCNQ at different magnification showing compact and irregular morphology.

Figure 6.6. Solid-state ESR measured at -100 °C.

Figure 6.7. Solid-state NMR spectra: (a) as-prepared sample; (b) after annealing at 400 °C, which indicates the destruction of the structure and radicals.

Figure 6.8. ESR spectra after annealing *p*-TCNQ above 400 °C: (a) at room temperature; (b) at -100 °C, showing the decrease in the intensity. These results are in good agreement with the solid-state ¹³C-NMR (Figure 6.7).

Figure 6.9. Magnetization as a function of field recorded at 300 K. Dark red line is the raw experimental data of magnetization. Dark blue line is magnetization after subtracting linear diamagnetic background. Inset displays low field hysteresis loop.

Figure 6.10. Magnetization as a function of the applied field (*H*), recorded at 300 K and 5 K. The linear diamagnetic background was subtracted from all data. Spontaneous magnetization was clearly observed, even at 300 K. The internal hysteresis loops are shown in the inset.

Figure 6.11. Magnetization as a function of field recorded at 300 K. Dark blue line is for data recorded two weeks after the synthesis of material and dark green line is for data recorded five weeks after the synthesis of material.

Figure 6.12. (a) Magnetization as a function of the temperature, recorded at 1000 Oe. Robust spontaneous magnetization persists up to 400 K. The estimated critical temperature is $T_c \sim 495$ K (Figure 6.14). The material also displays Curie-like behavior at low temperatures; (b) magnetization as a function of $\mu_B H/k_B T$ at various temperatures. The linear diamagnetic background and constant ferromagnetic component were subtracted from all data. The cyan line represents a fit to the Brillouin function with $J = S = 1/2$ under the assumption of $g = 2$. All curves collapse well into a single Brillouin function.

Figure 6.13. Determination of the angular momentum quantum number J via Brillouin function fit: (a) the estimated M_{para} component as a function of field H at 5 K (black symbols). Fitting to Brillouin function with $J = 1/2, 1, 3/2$ are indicated with solid lines, respectively. The g value was assumed to be 2 in fitting procedure. Only $J = 1/2$ produces excellent Brillouin function fit to the paramagnetic component M_{para} ; (b) the estimated M_{para} component as a function of field H at different temperatures ($T = 2, 3, 5,$ and 10 K). Solid cyan curves are fits to Brillouin function with $J = 1/2$ and $g = 2$.

Figure 6.14. Field-cooled magnetization as a function of temperature measured at 10 Oe (dark red squares). Black line is fit to conventional critical behavior, $\propto (T_c - T)^\beta$ with recorded data between 350 K and 395 K. The estimated T_c is ~ 495 K. The best fitting parameter for the critical exponent β was 0.48, which is close to the value of the mean field theory.

Figure 6.15. The temperature dependence of field-cooled (FC) vs. zero-field-cooled (ZFC) magnetizations. The measurements were done with applied fields of $H = 10$ (a), 100 (b), and 1000 Oe (c). The ZFC magnetizations were recorded after cooling of the sample in the absence of the magnetic field, while the FC magnetizations were recorded after cooling of the sample in applied magnetic fields (10, 100, and 1000 Oe). Upon reaching the lowest temperature of 5 K, magnetizations were measured on warming the sample in applied magnetic fields. The magnetization exhibited strong irreversibility, given by the divergence of the FC and ZFC magnetization curves below a bifurcation temperature (T_{irr}). The ZFC magnetization exhibited a maximum at a field-dependent temperature $T_{max} < T_{irr}$ and continuously decreased below this temperature. The bifurcation was shifted to lower temperature as H was increased. Strong irreversibility and the shift of T_{irr} to lower T with increasing H are signatures of spin glass like behavior. It is likely that our sample retains randomly distributed spin clusters leading to the glassy behavior.

List of Tables

Table 2.1. Elemental composition of the C_2N -*h*2D crystal from different characterization techniques

Table 2.2. Average (mean) electrical properties of the C_2N -*h*2D crystal field-effect transistors

Table 3.1. Elemental composition of the C_3N framework from different characterization techniques

Table 4.1. Elemental composition from different techniques

Table 5.1. Elemental composition from different techniques

Table 6.1. Elemental composition of the *p*-TCNQ framework from different characterization techniques

Table 6.2. Trace metal analysis of the impurities in the *p*-TCNQ framework determined by ICP-MS

Abbreviations

1. HAB: hexaaminobenzene
2. HCl: hydrochloric acid
3. TATB: 1,3,5-triamino-2,4,6-trinitrobenzene
4. FT-IR: Fourier transformed infrared spectroscopy
5. NMR: Nuclear magnetic resonance
6. EA: elemental analysis
7. TNA: 2,4,6-trinitroaniline
8. PTFE: polytetrafluoroethylene
9. ATA: 4-amino-1,2,4-triazole
10. 2D: two-dimensional
11. C₂N-*h*2D: C₂N holey two-dimensional crystal
12. STM: scanning tunneling microscopy
13. *h*-BN: hexagonal boron nitride
14. DFT: density functional theory
15. TGA: thermogravimetric analysis
16. SEM: scanning electron microscope
17. FE-SEM: field-emission scanning electron microscope
18. XPS: X-ray photoelectron spectroscopy
19. XRD: X-ray diffraction
20. TEM: transmission electron microscopy
21. HR-TEM: high-resolution transmission electron microscopy
22. BF: bright field
23. SAED: selected area electron diffraction
24. AFM: atomic force microscopy
25. DSC: differential scanning calorimetry
26. HKH: hexaketocyclohexane octahydrate
27. TFMSA: trifluoromethanesulfonic acid
28. NMP: N-methyl-2-pyrrolidone
29. VASP: Vienna Ab initio simulation package
30. PAW: projector augmented wave
31. UHV: ultrahigh vacuum
32. PET: polyethylene terephthalate
33. EDS: energy-dispersive X-ray spectroscopy

34. BET: Brunauer-Emmett-Teller
35. EELS: electron energy loss spectroscopy
36. CV: cyclic voltammogram
37. LUMO: lowest unoccupied molecular orbital
38. HOMO: highest occupied molecular orbital
39. TBAPF₆: tetrabutylammonium hexafluorophosphate
40. FET: field-effect transistor
41. PDMS: poly(dimethylsiloxane)
42. MAS-NMR: magic-angle spinning NMR
43. PANI: polyaniline
44. GC-MS: gas chromatography-mass spectrometry
45. Py-GC-MS: pyrolysis coupled GC-MS
46. PDOS: projected density of electronic states
47. GC: glassy carbon
48. IUPAC: international union of pure and applied chemistry
49. ORR: oxygen reduction reaction
50. RDE: rotating disk electrode
51. TCNQ: tetracyanoquinodimethane
52. TCNE: tetracyanoethylene
53. ESR: electron spin resonance
54. ICP-MS: inductively coupled plasma mass spectrometry
55. ZFC: zero-field-cooled
56. MALDI-TOF: Matrix-assisted laser desorption ionization time of flight
57. DI: de-ionized
58. DMAc: *N,N*-dimethylacetamide
59. DMF: *N,N*-dimethylformamide
60. DMSO: dimethyl sulfoxide
61. THF: tetrahydrofuran
62. EtOH: ethanol
63. MeOH: methanol
64. HNO₃: nitric acid
65. H₂SO₄: sulfuric acid
66. HF: hydrofluoric acid
67. KNO₃: potassium nitrate
68. MSA: methanesulfonic acid

I. Large-Scale Synthesis of Pure and Stable Hexaaminobenzene Trihydrochloride

1.1 Abstract

Hexaaminobenzene (HAB) synthesis in pure form with long shelf life has remained as a huge challenge for decades, since it is an interesting synthon for the preparation of aromatic nitrogenous materials having many fascinating applications. Herein, I present an easy synthesis of stable and pure HAB hydrochloride using modified catalytic hydrogenation in aqueous acidic medium. The absolute structure of needle shaped HAB crystals was verified by single crystal X-ray diffraction study. The preparation method could thus be an easy, but effective for the gram-scale synthesis of highly crystalline and stable HAB.

1.2 Introduction

The usability of the hexaaminobenzene (HAB) can be conceived on the ground of the new type of polynitrogenous heterocyclic systems comprising derivatives of hexaazatriphenylene,^{1,2} hexaazacoronene,³ fused benzotriazoles,⁴ benzotris(imidazole),⁵⁻⁶ benzotris[1,2,5]thiadiazole,⁷ benzotris[1,2,5]-selenodiazole,⁷ aromatic hexaamides with the behavior of lyotropic liquid crystals,⁴ and numerous other fascinating materials.⁸⁻¹⁰ This attractive symmetric material has been familiar to organic synthetic research community for many years.¹¹ A lot of attempts have been made to prepare HAB by reducing 1,3,5-triamino-2,4,6-trinitrobenzene (TATB) with phenylhydrazine,² catalytic hydrogenation³ and sodium in liquid ammonia,¹ these are the frequently used protocols. But in all these reported method, the HAB procured is in the form of free amine, which is very susceptible to atmospheric oxygen and light and decomposed into dark brown amorphous impure powder both in light and in the dark just within a few hours even under the inert condition.^{3,12-13} Although HAB trihydrochloride has been realized in single step in an aqueous HCl solution in the presence of SnCl₂,⁴ but its purity and stability are still not up to the standard. Until now, there have thus been no rationally practical literature for the gram-scale preparation of very pure HAB trihydrochloride crystals in an easy and efficient manner, because of the delicacy of HAB. In conclusion, most reported procedures have directly utilized HAB for next reactions without purification to separate reduction catalyst and conceivable impurities, if any.^{1,3}

1.3 Materials and Instrumentation

All the solvents, chemicals and reagents were purchased from Aldrich Chemical Inc., unless otherwise stated. All the reactions were carried out under inert atmosphere using oven dried glassware. All other solvents, reagents and chemicals were used as purchased unless otherwise stated. 2,4,6-Trinitroaniline and 1,3,5-triamino-2,4,6-trinitrobenzene were synthesized according to literature. 4-nitroaniline 99%, Dimethyl sulfoxide 99.9%, Pd/C 10%, Hydrochloric acid 37%, and ethyl acetate (anhydrous) were purchased from Sigma-Aldrich Chemical Inc. Nitric acid 60% was purchased from DC Chemical Co. Ltd. Celite 545 (C0340) was provided by Samchun Pure Chemical Co. Ltd.

Infrared (FT-IR) spectra were measured on Perkin-Elmer Spectrum 100 FT-IR spectrometer. Single crystal X-ray diffraction studies were recorded on R-Axis RAPID II Rigaku Japan. ¹H NMR and ¹³C NMR spectra were taken by using FT-NMR 600 MHz VNMRS 600 (Varian, USA). Mass spectra were carried out using 320-MS Varian, USA. Elemental analysis (EA) was measured on Flash 2000 Thermo Scientific, Netherland. Hydrogenation was measured using shaker type Parr Hydrogenation Apparatus Model-3911. Melting points were measured on KSP1N automatic melting point meter (KRUSS A. Kruss Optronic Germany).

1.4 Synthesis of 2,4,6-trinitroaniline (TNA, 1)

4-Nitroaniline (20 g, 0.088 mol) and H₂SO₄ (100 mL) were taken in a round bottom flask. A solution of potassium nitrate (KNO₃) (70 g, 0.70 mol) in concentrated sulfuric acid (H₂SO₄) (100 mL) was then introduced drop-wise at 50 °C. The reaction mixture was increased to 80 °C and stirred for 3 h and 110 °C for 3 h again. After finishing of the reaction, the reaction mixture was cooled to room temperature and mixed with ice cold water. The precipitates were collected by suction filtration, dried and recrystallized from dilute aqueous HCl solution to get 16.5 g (50% yield) of 2,4,6-trinitroaniline (glassy light yellow crystal). Mp 186-188 °C (Lit.¹⁴, 188 °C). EI-MS (DIP) (S4): *m/z* (%) 229 ([M + H]⁺, 100). Elemental analysis: calcd for C₆H₄N₄O₆ (228.12): C, 31.59; H, 1.77; N, 24.56; O, 42.08. Found: C, 30.51; H, 1.30; N, 20.70; O, 43.86. ¹H NMR (600 MHz, DMSO, δ = ppm) (S5): 8.585 (2H), 5.6 (2H). ¹³C NMR (600 MHz, DMSO, δ = ppm) (S6): 141.86 (C-4), 125.27 (C-2), 124.55 (C-3), 160.62 (C-1).

1.5 Synthesis of 1,3,5-triamino-2,4,6-trinitrobenzene (TATB, 2)

Sodium methoxide (23.8 g, 0.44 mol) was added to a solution of 2,4,6-trinitroaniline (4.56 g, 0.02 mol) and 4-amino-1,2,4-triazole (ATA) (16.8 g, 0.2 mol) in dimethyl sulfoxide (DMSO) (300 mL). The reddish-orange suspension was stirred at room temperature for 3 h. The reaction mixture was then added to ice cold aqueous HCl (0.4 M) solution. The obtained precipitates were gathered by suction filtration, washed with distilled water and dried. The solid after drying was dissolved in DMSO with small amount

of NaOH with moderate heating up to 70 °C, when the product was thoroughly dissolved the solution was added to ice cold aqueous HNO₃ (0.4 M) solution. The compound precipitated was again obtained by suction filtration to give 4.62g (89 % yield) of TATB (deep bright yellow powder). mp > 300 °C (dec.). EI-MS (DIP): m/z (amu) 259.1 ([M + H]⁺, 100). Elemental analysis: calcd for C₆H₆O₆N₆ (258.14): C, 27.9%; H, 2.32%; N, 32.55%; O, 37.2%. Found: C, 28.03%; H, 1.86%; N, 26.57%; O, 44.79%. ¹³C NMR (600 MHz, DMSO, δ = ppm): 113.52 (C-4), 117.48 (C-2), 147.01 (C-3), 157.14 (C-1). The FT-IR reveals asymmetrical N-H stretching absorption peak at 3363 cm⁻¹ and symmetrical N-H stretching at 3225 cm⁻¹ are identifying peak for TATB. Other peaks are N-O asymmetrical stretching at 1560 cm⁻¹, symmetrical N-O stretching at 1201 cm⁻¹, C-N stretching (amino group) 1613 and 798 cm⁻¹, and skeletal stretching of the ring at 1475, 1180, 1053 cm⁻¹.

1.6 Synthesis of hexaaminobenzene trihydrochloride (HAB, 3)

TATB (3.0 g, 0.012 mol) was procured in high pressure hydrogenation glass vessel with palladium on activated carbon (10% Pd/C, 500 mg) and anhydrous ethyl acetate (150 mL) as a solvent. The reaction vessel was fixed in hydrogenation apparatus and shaken under hydrogen (H₂) gas (60 psi) till the whole yellowish color of the reactant vanished thoroughly in three days. Then, concentrated hydrochloric acid (HCl) (90 mL) was poured into the reaction mixture and the reaction was proceeded under H₂ for another 5 h. The reaction mixture was passed through Celite under vacuum to separate the reaction catalyst. The HAB trihydrochloride crystallized out very nicely in high yield (**Figure 1.1**). The precipitates formed were obtained by suction filtration by using polytetrafluoroethylene (PTFE) membrane (0.5 μm pore) and dried in oven at 70 °C for 4 h under vacuum (0.5 mmHg). The white small crystals of HAB were re-dissolved in deionized (DI) water and filtered through PTFE membrane to separate solid impurities, if any, and added 80 ml of concentrated HCl. The flask was tightly closed and put in the freezer until very nice large crystals appeared. The crystals were obtained on PTFE membrane filter in the lab atmosphere and rinsed completely with ethyl acetate and dried in the oven under reduced pressure (**Figure 1.5a**) to afford 3.0 g (92 % yield). mp 250-254°C. EI-MS (DIP): m/z (amu) 169.1 ([M + H]⁺, 78.5), 167.1 ([M - H]⁺, 100). Elemental analysis: calcd for C₆H₁₅N₆Cl₃ (277.58): C, 25.96%; Cl, 38.32%; H, 5.45%; N, 30.28%. Found: C, 26.54%; Cl, 36.54%; H, 4.96%; N, 25.05%; O, 6.89%. FT-IR spectrum (cm⁻¹): 3384.41, 3249.28, 2977.06, 2564.72, 1671.16, 1636, 1582.02, 1554, 1479.74, 1279, 1202.9, 1166.34, 1096.

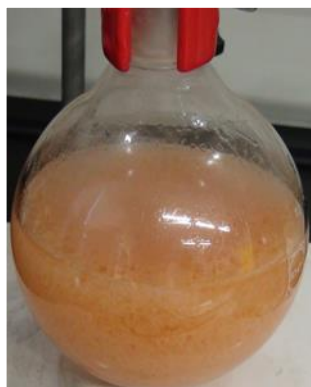


Figure 1.1 Photograph of crystallized HAB after filtration through Celite and washing with aqueous HCl (0.5 M) solution.

1.7 Single crystal X-ray diffraction study

A crystal of **3** (HAB) was coated with paratone oil and the diffraction data measured at 193 K with Mo K α radiation on an X-ray diffraction camera system using an imaging plate equipped with a graphite crystal incident beam monochromator. The Rapid Auto software (Rapid Auto software, R-Axis series, Cat. No. 9220B101, Rigaku Corporation) was used for data collection and data processing. Structure was determined by direct method and refined by full-matrix least-squares calculation with the SHELXTL software package. (G. M. Sheldrick, *SHELXTL-PLUS, Crystal Structure Analysis Package*; Bruker Analytical X-Ray; Madison, WI, USA, **1997**). A cationic molecular ion on a crystallographic $2/m$ symmetry site (Wyckoff symmetry site b), a chloride anion on a crystallographic $m2m$ symmetry site (Wyckoff symmetry site c), and another chloride anion on a crystallographic m symmetry site (Wyckoff symmetry site g) are observed as an asymmetric unit. The non-hydrogen atoms are refined anisotropically; the hydrogen atoms are found in the difference Fourier map and refined isotropically. The site occupancy factors of two hydrogen sites around the N atom on a crystallographic m symmetry site were assigned as 100 and 25% site occupancy factors, respectively, and the site occupancy factors of the three hydrogen sites around another N atom on a general position as 100, 75 and 75% site occupancy factors, respectively, based on two different types of mixed geometries of 50% $-\text{NH}_2$ and 50% $-\text{NH}_3$ structures. Refinement of the structure converged at a final $R1 = 0.0345$, $wR2 = 0.0880$ for 646 reflections with $I > 2\sigma(I)$; $R1 = 0.0447$, $wR2 = 0.0925$ for all 742 reflections. The largest difference peak and hole were 0.332 and $-0.312 \text{ e} \cdot \text{\AA}^{-3}$, respectively.

1.8 Results and Discussion

I extensively surveyed and utilized the literature to achieve highly pure HAB by using a number of these conventional methods for the reduction of nitro groups on TATB (**Figure 1.2a**). Though some amount of HAB was synthesized with low quality in a very poor yield (**Figure 1.2b**), but all procedures not successful during the catalyst separation and purification. The highly low stability of free HAB was the prominent major reason for the poor yield and low quality material and its color quickly turns into dark brown. Kohne, *et al.* have narrated the preparation of HAB trihydrochloride crystal.¹³ But, the method is so tiring, time-wasting and demands very carefulness. Any small mistake can crash the all endeavors, and thus securing pure HAB in gram-scale has been very difficult. However, the quality of HAB trihydrochloride crystal is the best among reported protocols, while the crystal quality is still insufficient for high quality polymer synthesis (**Figure 1.2c**). After failures again and again to prepare sufficiently pure HAB crystals, I revised a clear and useful method for the preparation of this delicate material in stable form via modified catalytic reduction.

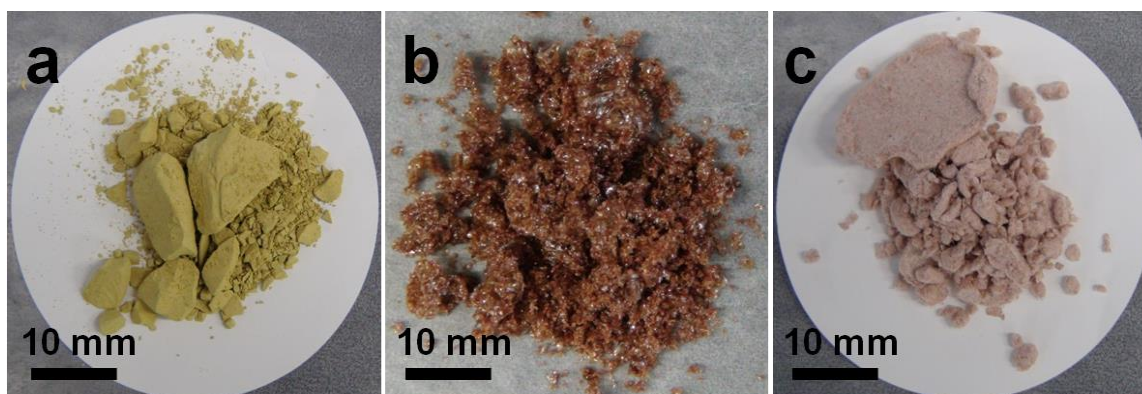


Figure 1.2. (a) Digital photograph of the TATB, (b) image of the HAB crystals as one of the best secured samples from reported catalytic reduction of TATB in the presence of H_2 and platinum (10 wt%) on activated carbon (Pd-C),³ (c) HAB trihydrochloride crystal procured from the reduction of TATB in the presence of $SnCl_2/HCl$ system.⁴

The synthesis initiated with the famous nitration of *p*-nitroaniline into 2,4,6-trinitroaniline in concentrated sulfuric acid in the presence of potassium nitrate (**Figure 1.3**).¹⁴ The recrystallized 2,4,6-trinitroaniline was reacted with 4-amino-1,2,4-triazole (ATA) and sodium methoxide in dimethyl sulfoxide (DMSO) in vicarious nucleophilic reaction condition and later acid treatment with 0.4 M HCl produced 1,3,5-triamino-2,4,6-trinitrobenzene (TATB) in high yield.¹⁵ Amazingly, the TATB in DMSO exhibits an interesting mesomeric form (amine to imine mesomer) to ease a bit of its steric strain by

donating its lone pair electron on nitrogen into the aromatic ring (**Figure 1.4**) and it was confirmed by ^{13}C -NMR. Eventually, the TATB was hydrogenated to make HAB trihydrochloride by a modified protocol to gain extremely neat creamy white needle-like crystals (**Figure 1.5a**) with fairly transparent and reflective (**Figure 1.5b**), showing the good condition of crystals. The crystal length dimensions are larger than 1 mm (**Figure 1.5c**) and a few crystals are even larger than 5 mm from the optical microscope image. The crystals remained stable in a sealed bottle for more than one year (**Figure 1.5d**). The complete crystal structure of HAB trihydrochloride was resolved for the first time by single crystal X-ray crystallography (**Figure 1.5e and 1.5f**). Accordingly, the gram-scale synthesis of highly neat and clean HAB trihydrochloride crystals was realized by modified and enhanced synthetic method.

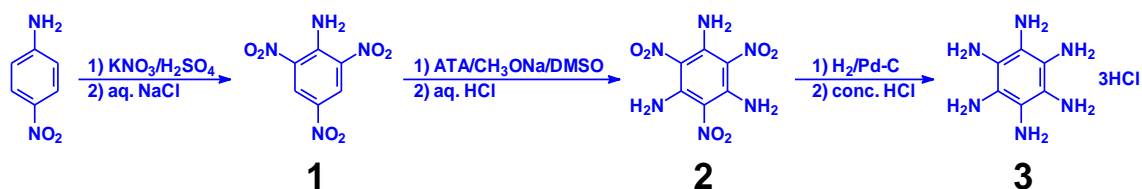


Figure 1.3. The synthesis of hexaaminobenzene (HAB) trihydrochloride.



Figure 1.4. Mesomerism of TATB in DMSO.

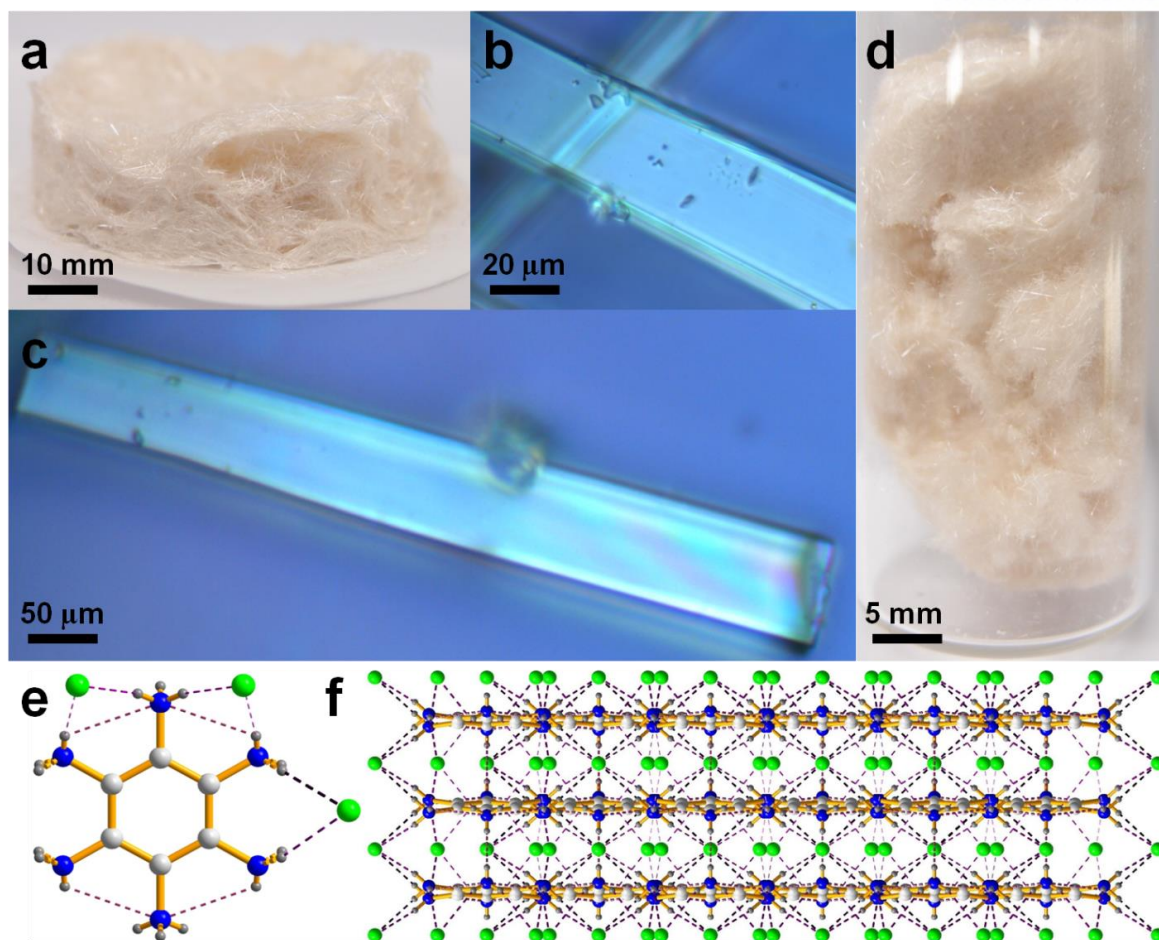


Figure 1.5. (a) Digital photograph of HAB trihydrochloride crystals on PTFE filter membrane; (b, c) optical microscopic images of the HAB trihydrochloride crystals; (d) digital photograph of HAB in a bottle after one year; (e) formula unit of the HAB trihydrochloride; (f) hydrogen-bonding driven molecular packing into the needle-like crystal structure.

The HAB could be an interesting component for the fabrication of discotic liquid crystals,¹⁶⁻¹⁹ materials with small barrier to both electron and hole transport for possible applications in organic/polymer electronics,²⁰ preparation of macrocyclic materials,²¹ hexaazatriphenylene based donor-acceptor molecules,^{8,22} electron deficient extended-electron systems,²³ ferromagnetic organic salts,^{3,24} fluorescence sensor for cadmium (II),²⁵ and so forth.

1.9 Conclusions

In summary, I have a firm believe that my procedure would be fairly handy for fabrication of other sensitive aromatic amines from their parent polynitroarenes. Though the optimized nitro group reduction procedure, presented here has not been utilized on other polynitroarene molecules, but it

would be of huge significance for the reduction of other delicate materials with this newly formulated method. Furthermore, crystalline HAB could be a vital constituent for the preparation of numerous aesthetic and application-specific materials.

1.10 References

- (1) Rogers, D. Z. Improved Synthesis of 1,4,5,8,9,12-Hexaazatriphenylene. *J. Org. Chem.* **1986**, *51*, 3904-3905.
- (2) Kohne, B.; Praefcke, K. ine neue und einfache Synthese des Dipyrazino[2,3-f:2',3'-h]-chinoxalin-Ringsystems. *Liebigs Ann. Chem.* **1985**, *1985*, 522-528.
- (3) Breslow, R.; Maslak, P.; Thomaidis, J. S. Synthesis of the hexaaminobenzene derivative hexaazaoctadecahydrocoronene (HOC) and related cations. *J. Am. Chem. Soc.* **1984**, *106*, 6453-6454.
- (4) Khisamutdinov, G. K.; Korolev, V. L.; Kondyukov, I. Z.; Abdrakhmanov, I. S.; Smirnov, S. P.; Fainzilberg, A. A.; Dorokhov, V. G. The synthesis of fused benzotriazoles based on hexaaminobenzene derivatives. *Rus. Chem. Bull.* **1993**, *42*, 136-138.
- (5) Kohne, B.; Praefcke, K.; Derz, T.; Gondro, T.; Frolow, F. Benzotri(imidazole)—a New Ring System Derived from Benzenehexamine. *Angew. Chem. Int'l Ed.* **1986**, *25*, 650-651.
- (6) Wolff, J. J.; Limbach, H.-H. Synthesis and spectroscopic characterization of ¹⁵N-labeled hexaaminobenzene derivatives. *Liebigs Ann. Chem.* **1991**, *1991*, 691-693.
- (7) Praefcke, K.; Kohne, B.; Korinth, F. Benzotris[1,2,5]thiadiazol in einer Eintopfreaktion aus Benzolhexamin. *Liebigs Ann. Chem.* **1990**, *1990*, 203-204.
- (8) Juárez, R.; Ramos, M.; Segura, J. L.; Orduna, J. s.; Villacampa, B. n.; Alicante, R. Synthesis and Electrochemical and Theoretical Studies of V-Shaped Donor–Acceptor Hexaazatriphenylene Derivatives for Second Harmonic Generation. *J. Org. Chem.* **2010**, *75*, 7542-7549.
- (9) Ishi-i, T.; Murakami, K.-i.; Imai, Y.; Mataka, S. Self-Assembled Fluorescent Hexaazatriphenylenes That Act as a Light-Harvesting Antenna. *J. Org. Chem.* **2006**, *71*, 5752-5760.
- (10) Ishi-i, T.; Murakami, K.-i.; Imai, Y.; Mataka, S. Light-Harvesting and Energy-Transfer System Based on Self-Assembling Perylene Diimide-Appended Hexaazatriphenylene. *Org. Lett.* **2005**, *7*, 3175-3178.
- (11) Flurschein, B.; Holmes, E. L. Hexa-aminobenzene. *J. Chem. Soc.* **1929**, 330-337.

- (12) Thomaidēs, J.; Maslak, P.; Breslow, R. Electron-rich hexasubstituted benzene derivatives and their oxidized cation radicals, dications with potential triplet ground states, and polycations. *J. Am. Chem. Soc.* **1988**, *110*, 3970-3979.
- (13) Kohne, B.; Praefcke, K. Isolierung farblosen Benzolhexamins. *Liebigs Ann. Chem.* **1987**, *1987*, 265-265.
- (14) Wang You-bing, W. B.-z., Ye Zhi-hu, Shang Yan, Qin Hui, Li Ya-nan. Synthesis of TATB by VNS Method. *Chinese J. Energ. Mate.* **2011**, *19*, 142-146.
- (15) Alexander R. M.; Philip F. P.; Robert D. S. Vicarious Nucleophilic substitution using 4-amino-1,2,4-triazole, Hydroxyleamine or O-alkylhydroxylamine to prepare 1,3-diamino-2,4,6-trinitrobenzene or 1,3,5-triamino-2,4,6-trinitrobenzenesynthesis and purification of 1,3,5-triamino-2,4,6-trinitrobenzene. *U.S. Patent* 5633406, **1997**.
- (16) Ong, C. W.; Liao, S.-C.; Chang, T. H.; Hsu, H.-F. Rapid synthesis of new discotic liquid crystals based on diquinoxalino[2,3-a:2',3'-c]phenazine containing hexakis(alkoxy) side arms. *Tetrahedron Lett.* **2003**, *44*, 1477-1480.
- (17) Yeh, M.-C.; Liao, S.-C.; Chao, S.-H.; Ong, C. W. Synthesis of polyphilic hexaazatrinaphthylenes and mesomorphic properties. *Tetrahedron* **2010**, *66*, 8888-8892.
- (18) Ong, C. W.; Liao, S.-C.; Chang, T. H.; Hsu, H.-F. In Situ Synthesis of Hexakis(alkoxy)diquinoxalino[2,3-a:2',3'-c]phenazines: Mesogenic Phase Transition of the Electron-Deficient Discotic Compounds. *J. Org. Chem.* **2004**, *69*, 3181-3185.
- (19) Ishi-i, T.; Hirayama, T.; Murakami, K.-i.; Tashiro, H.; Thiemann, T.; Kubo, K.; Mori, A.; Yamasaki, S.; Akao, T.; Tsuboyama, A.; Mukaide, T.; Ueno, K.; Mataka, S. Combination of an Aromatic Core and Aromatic Side Chains Which Constitutes Discotic Liquid Crystal and Organogel Supramolecular Assemblies. *Langmuir* **2005**, *21*, 1261-1268.
- (20) Barlow, S.; Zhang, Q.; Kaafarani, B. R.; Risko, C.; Amy, F.; Chan, C. K.; Domercq, B.; Starikova, Z. A.; Antipin, M. Y.; Timofeeva, T. V.; Kippelen, B.; Brédas, J.-L.; Kahn, A.; Marder, S. R. Synthesis, Ionisation Potentials and Electron Affinities of Hexaazatrinaphthylene Derivatives. *Chem. –Euro. J.* **2007**, *13*, 3537-3547.
- (21) Secondo, P.; Fages, F. Design and Synthesis of Bismacrocylic Hexaazatriphenylene Derivatives. *Org. Lett.* **2006**, *8*, 1311-1314.

(22) Juárez, R.; Ramos, M. M.; Segura, J. L. synthesis of non-centrosymmetric donor–acceptor–donor hexaazatriphenylene (HAT) derivatives. *Tetrahedron Lett.* **2007**, *48*, 8829-8833.

(23) Ishii, T.; Hirashima, R.; Tsutsumi, N.; Amemori, S.; Matsuki, S.; Teshima, Y.; Kuwahara, R.; Mataka, S. Expanded π -Electron Systems, Tri(phenanthro)hexaazatriphenylenes and Tri(phenanthro)hexaazatriphenylenes, That Are Self-Assembled To Form One-Dimensional Aggregates. *J. Org. Chem.* **2010**, *75*, 6858-6868.

(24) Breslow, R.; Jaun, B.; Kluttz, R. Q.; Xia, C.-z. Ground state Pi-electron triplet molecules of potential use in the synthesis of organic ferromagnets. *Tetrahedron* **1982**, *38*, 863-867.

(25) Zhao, Q.; Li, R.-F.; Xing, S.-K.; Liu, X.-M.; Hu, T.-L.; Bu, X.-H. A Highly Selective On/Off Fluorescence Sensor for Cadmium(II) *Inorg. Chem.* **2011**, *50*, 10041-10046.

II. C₂N holey two-dimensional crystal

2.1 Abstract

Graphene and hexagonal boron nitride (*h*-BN) are the thinnest materials with a similar monoatomic two dimensional (2D) geometry, but their electronic structures are in the opposite extreme; one is metal and the other has wide band-gaps, limiting the interest and their potential applications of them. Design of unique versatile, flexible two-dimensional (2D) fused aromatic materials with proper control and a finite band-gap has become a huge challenge. Herein, I present a new layered 2D network structure with uniformly distributed holes and nitrogen atoms, and the overall stoichiometry is thought to be C₂N. The 2D structure can be readily synthesized by an uncomplicated wet-chemical reaction from the thoughtfully functionalized monomers. Different characterization techniques, including the use of scanning tunneling microscopy (STM), confirm the structure of the holey 2D crystal and the calculated and experimental band-gaps are in the semiconductor region about 1.7 and 2.0 eV, respectively, suggesting clear advantages over the most widely investigated conducting graphene and insulating hexagonal boron nitride (*h*-BN).

2.2 Introduction

The recent advent of graphene has aroused the scientists in different fields, chiefly because of its unique inherent electronic structure to the monoatomic 2D crystal¹. The peculiar traits of graphene pledge numerous applications such as nanoelectronics², hydrogen storage³, batteries⁴, and sensors⁵. The ample scientific debates in the field of graphene have ignited great involvement in new 2D ordered crystals fabricated by incorporation of elements other than carbon⁶. Researchers all over the world are dreaming for the preparation of 2D crystals using bottom-up approach with tunable structures and properties^{7,8}. One of the immense motivation is to establish a definite dimension stable band-gap⁹ in such well-defined 2D structure¹⁰, which is one of crucial requirement for applications to any active switching components in electronics^{11,12}. Different architectural alterations, including doping of heteroatoms, have been researched in this prospective. Among them the exchange of nitrogen (N) atom seems to be a good option, because the atomic size and five-electron valence structure (*sp*² hybridization) can naturally fit to the strong covalent framework structure of carbon atoms¹³. The versatility of the scientific applications of the band-gap generated 2D materials that can help to look for simple and facile directions to produce N-containing 2D structures. Recently, a number of techniques have been utilized for obtaining N-containing 2D crystals that come from graphene^{14,15} and graphene oxide¹⁶, which involve the poor control, toxicity, harsh reaction conditions and metal contamination. Very notably, however, the structures of N-containing 2D materials are not precise for use in practice. In consequence,

developing a properly controlled large-scale production procedure for an N-containing 2D network has grown into a huge challenging task for the researchers community^{7,8,17}. The band-gap of the newly-prepared 2D crystal with evenly distributed holes and nitrogen atoms were studied by using different experimental techniques and density functional theory (DFT). Moreover, synthesis of the N-containing holey 2D crystal is believed to be a base material for forthcoming advancement of versatile 2D crystals.

2.3 Materials

All the solvents, chemicals and reagents were acquired from Aldrich Chemical Inc., unless otherwise stated. Anhydrous NMP and glacial acetic acid were degassed with nitrogen purging before use. All the reactions were carried out under nitrogen condition using oven dried glassware. 2,4,6-Trinitroaniline, 1,3,5-triamino-2,4,6-trinitrobenzene and 1,2,3,4,5,6-hexaaminobenzene trihydrochloride¹⁸ were synthesized according to modified literature procedures. Trifluoromethanesulfonic acid (TFMSA) was freshly distilled before use.

2.4 Instrumentation

Thermogravimetric analysis (TGA) was performed in air and argon atmospheres at a heating rate of 10 °C/min using a Thermogravimetric Analyzer Q200 TA Instrument, USA. Scanning electron microscope (SEM) images were captured using Field Emission Scanning Electron Microscope Nanonova 230 FEI, USA. X-ray photoelectron spectroscopy (XPS) was carried out on X-ray Photoelectron Spectroscopy Thermo Fisher K-alpha (UK). X-ray diffraction (XRD) studies were done on High Power X-Ray Diffractometer D/MAZX 2500V/PC (Cu-K α radiation, 35 kV, 20 mA, $\lambda = 1.5418 \text{ \AA}$) Rigaku, Japan. High resolution transmission electron microscopy (TEM) was accomplished by using JEOL, Japan under an operating voltage of 200 keV. The samples for TEM were made by dropping NMP dispersion on Quantifoil holey carbon TEM grid and dried in vacuum oven at 80 °C.

2.5 Synthesis of the C₂N-h2D crystal (nitrogen containing holey 2D crystal)

Hexaaminobenzene trihydrochloride (HAB, 2g, 7.20 mmol) and hexaketocyclohexane octahydrate (HKH, 2.248g, 7.20 mmol) were placed in a 3-necked round bottom flask under nitrogen condition and put in ice bath. N-methyl-2-pyrrolidone (NMP, 80 mL) with a few drops of sulfuric acid or freshly distilled trifluoromethanesulfonic acid (TFMSA, 80 mL) was added slowly. The reaction flask was slowly warm up to ambient temperature for 2h. The ice bath was interchanged with oil bath and raised the temperature to 175 °C for 8h. Then, the flask was allowed to cool to ambient condition and water was added. Then the black product that precipitated was obtained by suction filtration using PTFE (0.5

μm) filter membrane. The resultant black solid was further Soxhlet extracted with methanol and water, respectively, and freeze-dried at $-120\text{ }^{\circ}\text{C}$ under vacuum (0.05 mmHg) for three days.

2.6 $\text{C}_2\text{N-}h2\text{D}$ crystal as a heterogeneous catalyst (Model reaction)

The $\text{C}_2\text{N-}h2\text{D}$ crystal efficiently catalyzes the Knoevenagel condensation reaction. Terephthaldehyde (2.00 g, 14.91 mmol) and malononitrile (1.97 g, 19.82 mmol) reacted in benzene (50 mL) in the presence of the $\text{C}_2\text{N-}h2\text{D}$ crystal (100 mg) as a reaction catalyst. The reaction mixture was kept on stirring at room temperature overnight under nitrogen atmosphere. Then the reaction mixture was filtered to simply remove the insoluble catalyst. The filtrate was dried by rotary evaporator to give a yellowish solid residue in quantitative yield. After recrystallized from ethanol, purified was 95%. The recovered $\text{C}_2\text{N-}h2\text{D}$ crystal was repeatedly used three times, showing almost the same catalytic efficiency. ^1H NMR (600 MHz, DMSO) δ 8.08 (4H), 8.32 (2H); ^{13}C NMR (600 MHz, DMSO) δ 84.71, 112.75, 113.81, 130.85, 135.34, 159.81; HR-MS (ESI⁺) Calcd. for ($\text{C}_{14}\text{H}_6\text{N}_4^+$) 230.0592, Found, 230.0591.

2.7 First-principle calculations

For computations, the Vienna *Ab initio* simulation package (VASP) was used to calculate the ground state of many electrons system in the frame work of density functional theory³²⁻³⁵. The plane-wave basis set with an energy cut-off of 400 eV and the PBE-type gradient-corrected exchange-correlation potential were employed³⁶. The ions were described by the projector augmented wave (PAW) potentials. In the self-consistent-field total energy calculations, the k-points are uniformly sampled over the reciprocal space of the two-dimensional triangular lattice with mesh 21 by 21. All the atomic positions of were relaxed within residual forces smaller than $0.0\text{eV}/\text{\AA}$.

2.8 STM experiments

The STM experiments were conducted in a UHV low-temperature scanning tunneling microscope (SPECS JT-STM) at 77 K. The Cu(111) single crystal was cleaned by a few cycles of Ar^+ sputtering and annealing. After cleaning the Cu(111) substrate, the as-synthesized $\text{C}_2\text{N-}h2\text{D}$ crystal was deposited on the pre-cleaned Cu(111) substrate by *in-situ* thermal evaporation under UHV condition. The sample evaporation temperature was about 600 K, and the temperature of the substrate was maintained at room temperature.

2.9 Results and Discussion

The difference between graphene (**Figure 2.1a**) and holey graphene (**Figure 2.1b**), which is not yet been realized, is evenly distributed periodic holes in fused aromatic network structure. The newly-

fabricated holey nitrogenated 2D crystal has not only evenly distributed holes, but also the holes and phenyl rings are surrounded by aromatic nitrogen atoms of the fused pyrazine like rings (pink balls in **Figure 2.1c**). Unlike the entirely conjugated π -electron network of graphene (**Figure 2.1a**), an articulate insertion of uniform holes and nitrogen atoms is likely to stretch the gap between the valence and conduction bands (band-gap) to optimal level for band-gap opened material, which is, for example, useful for semiconductor application. The peculiar N-containing holey 2D crystal was easily prepared by reacting hexaaminobenzene (HAB) trihydrochloride (**Figure 2.1d**)¹⁸ and hexaketocyclohexane

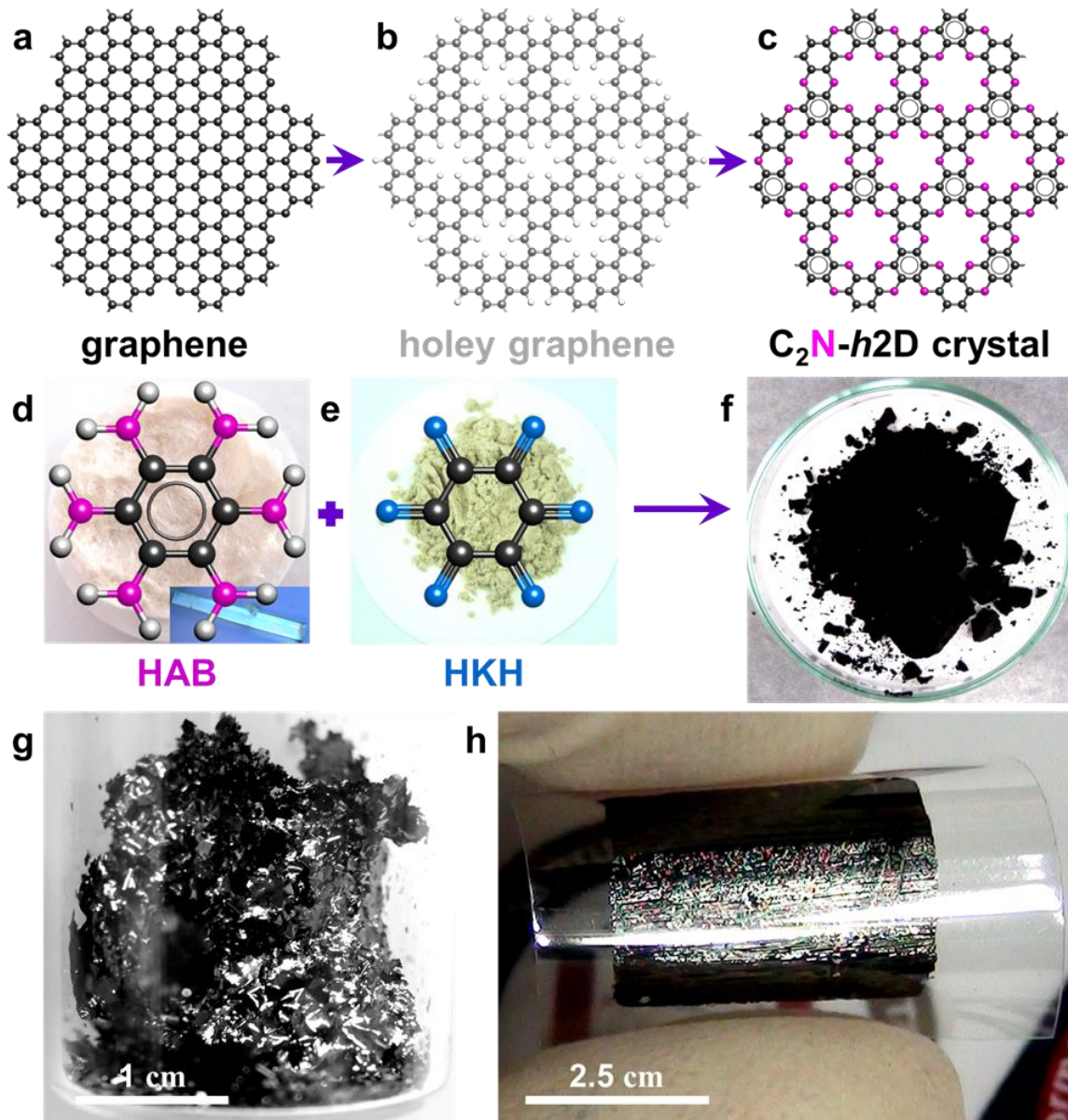


Figure 2.1. Schematic presentation of the difference among two-dimensional structures: (a) Graphene (1st generation); (b) Holey graphene (2nd generation, not yet been realized); (c) Holey nitrogenated graphene (3rd generation, designated as C₂N-*h*2D crystal). The synthesis of the C₂N-*h*2D

crystal: (d) Hexaaminobenzene (HAB) trihydrochloride. Inset is a polarized optical microscope image of the HAB single crystal; (e) Hexaketocyclohexane (HKH) octahydrate. Digital photographs: (f) as-prepared C₂N-*h*2D crystal; (g) Solution-cast C₂N-*h*2D crystal on SiO₂ surface and heat-treated at 700 °C; (h) Transferred C₂N-*h*2D crystal film (thickness: ~ 330 nm) on PET substrate. Metallic shiny reflection indicates high crystallinity.

Hexaketocyclohexane (HKH) octahydrate (**Figure 2.1e**) in *N*-methyl-2-pyrrolidone (NMP) with a few drops of sulfuric acid (H₂SO₄ or in freshly distilled trifluoromethanesulfonic acid (TFMSA). The tremendous potential energy gain by aromatization (*ca.* -89.7 kcal/unit mol, calculated with the DFT, **Figure 2.2**) is the driving force for the spontaneous polycondensation between HAB and HKH and leads to the development of a crystalline 2D framework structure¹⁹. The obtained dark black graphite-like solid (**Figure 2.1f**), a strong signal of the creation of a conjugated layered 2D crystal, was Soxhlet extracted with water and methanol, respectively, to thoroughly remove the small mass impurities, if any, and finally freeze-dried at -120 °C under vacuum (0.05 mmHg). When the solution of the material was cast on a SiO₂ substrate and annealed at 700 °C under an argon condition and obtained by etching in hydrofluoric acid, the material has more shiny flakes with a strong light reflection (**Figure 2.1g**). A large-area film could also be cast and transferred on a flexible polyethylene terephthalate (PET) substrate (**Figure 2.1g**).

The empirical formulas of the structure are C₂N for the repeating unit in basal plane (structure **2** in **Figure 2.2**) and C₆H₂N₃O for the whole material including edge functional groups (structure **1** in **Figure 2.2**). Different elemental analyses using various techniques have confirmed the chemical formula of the molecule (**Table 2.1**). Thus, the new 2D crystal has been named “C₂N holey 2D crystal” and designated as “C₂N-*h*2D crystal”, whose solubility has been tested to be well soluble in different commonly used solvents, showing colloidal scattering (**Figure 2.3**).

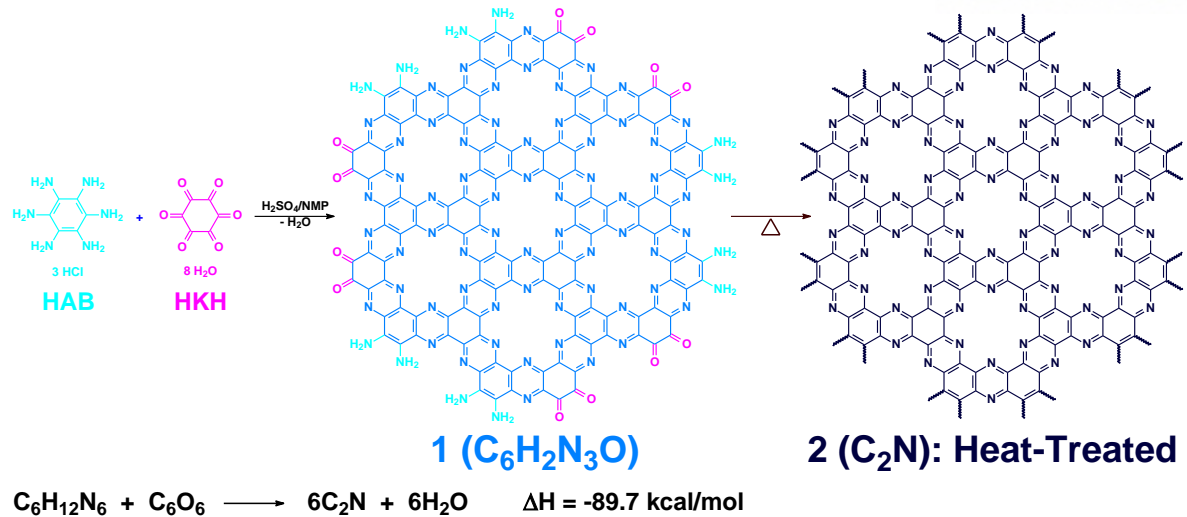


Figure 2.2. Schematic presentation for the formation of the C₂N-*h*2D crystal with edge groups and thermodynamics of reaction. Reaction enthalpy (ΔH), calculated with the PBE density functional theory, is found to be -89.7 kcal/unit mol. After heat-treatment, bound small molecules (H₂O, O₂, and etc.) and edge groups from structure 1 could be thermally stripped off to give the heat-treated C₂N holey structure 2.

Table 2.1. Elemental composition of the C₂N-*h*2D crystal from different characterization techniques

Technique	C	H	N	O	Total
Theoretical (wt%)	54.54	1.54	31.81	12.11	100
EA (wt%)^a	49.53	3.04	20.90	26.46	99.93
XPS (at%)^b	66.49		17.89	15.62	100
SEM EDS (wt%)	47.07		31.44	21.49	100
TEM EDS (wt%)	52.93		35.96	11.11	100

^a EA is most reliable element counts for bulk sample. The lower carbon content and the higher oxygen and hydrogen contents than theoretical calculation should be due to trapped small molecules (moisture, oxygen, and etc.) in the holes and interlayers of the C₂N-*h*2D crystal.

^b XPS is more sensitive to surface chemical composition.

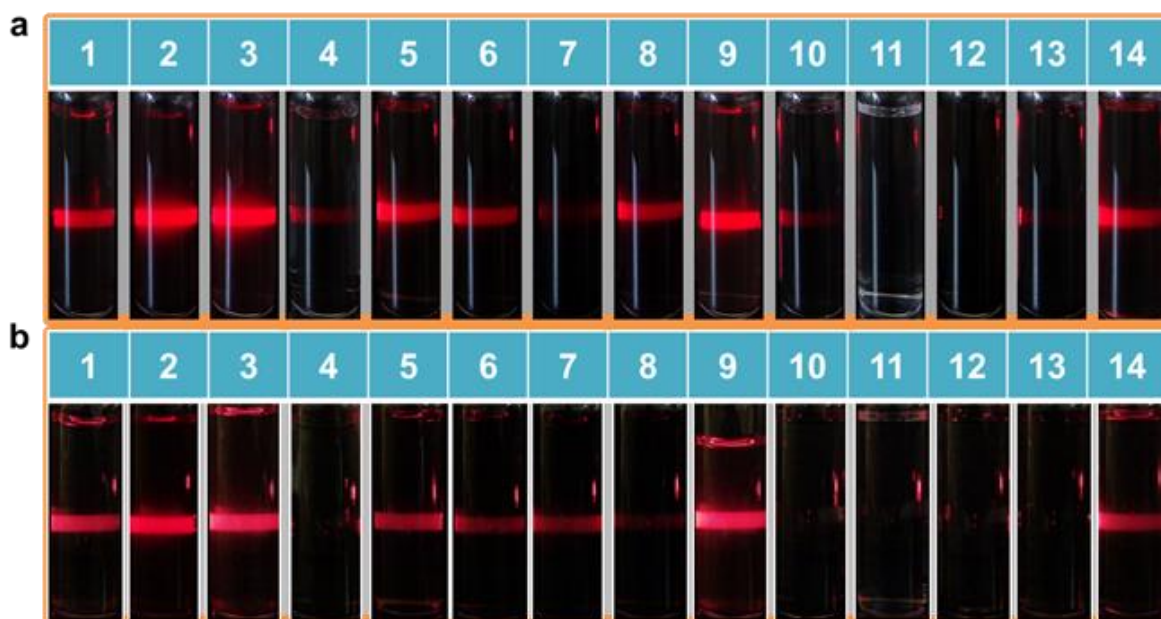


Figure 2.3. Solubility of the C₂N-*h*2D crystal in various solvents: (a) After 30s. (b) After 1 week. (1) water; (2) acetic acid; (3) MeOH; (4) 1M HCl; (5) NMP; (6) DMF; (7) DMSO; (8) DMAc; (9) acetone; (10) toluene; (11) THF; (12) 1M NaOH; (13) benzene; (14) dichlorobenzene.

The powder x-ray diffraction (XRD) pattern of the C₂N-*h*2D crystal reveals a readily layered structure with high crystallinity. Like graphite, this crystal also reveals a single diffraction peak at 27.12° (**Figure 2.4a**), whose value related to the interlayer distance (*d*-spacing) of 0.328 nm. Yet, its *d*-spacing is smaller than that of graphite (*d* = 0.335 nm)²⁰. The narrower *d*-spacing of the C₂N-*h*2D crystal is thought to be originated from the uniformly distributed nitrogen atoms. Nitrogen has a smaller atomic size (70 pm) and stronger polarity (electronegativity $\chi = 3.07$) than carbon (77 pm and $\chi = 2.55$).

X-ray photoelectron spectroscopy (XPS) measurement was performed to probe the chemical composition of the new material. The characteristic band for the K-edge of nitrogen appeared at 399 eV, revealing the *sp*²-hybridized nitrogen atoms in the holey 2D structure. The survey scan spectrum from the XPS analysis exhibited the occurrence of C1s, N1s, and O1s without any other impurities (**Figure 2.4b**). In the high resolution C1s spectrum, the dominant C1s signals are centered at approximately 285.55 eV (graphitic *sp*²C-C and *sp*²C-N). The C1s spectra can be deconvoluted into 285.13, 286.23 and 288.8 eV (**Figure 2.5a**). The peaks at 285.55 and 286.23 eV are assigned to *sp*²C-C and *sp*²C-N, respectively, in the aromatic ring, whereas the minor peak at 288.8 eV is attributed to the C-heteroatom, e.g., *sp*²C=O, *sp*²C-NH₂ at the edges (see structure **1** in **Figure 2.2**). The N1s spectrum shows only one major peak at 399.56 eV for the pyrazine-like nitrogen in the system and a very small peak at 398.36 eV for the C-NH₂ at the edges (**Figures 2.4a and 2.5b**)^{21,22}. The presence of

O1s peak in the C_2N -*h*2D crystal can be attributed to the trapped substances such as moisture and O_2 in the holey structure (**Figure 2.5c**), as well as the residual carbonyl (C=O) groups at the edges (see structure **1** in **Figure 2.2**)²³. Indeed, the heat-treated sample at 700 °C displayed a significantly reduced intensity of O1s peak, while that of N1s peak remained almost constant (**Figure 2.6**). The result implies that the O1s peak before annealing has mostly contributed to the trapped substances in the holes and interlayers. Thermogravimetric analysis (TGA) showed that the as-prepared C_2N -*h*2D crystal displayed a continuous weight loss from the start (**Figure 2.4c**). On the other hand, the heat-treatment C_2N -*h*2D crystal at 700 °C under an argon condition displayed high thermal stability in both air and argon (**Figure 2.4d**), showing that the early weight loss of as-prepared sample was because of the entrapped volatile compounds in the holes. As a result, the Brunauer-Emmett-Teller (BET) specific surface areas of the before and after heat-treated samples were 26 and 281 m^2g^{-1} , respectively.

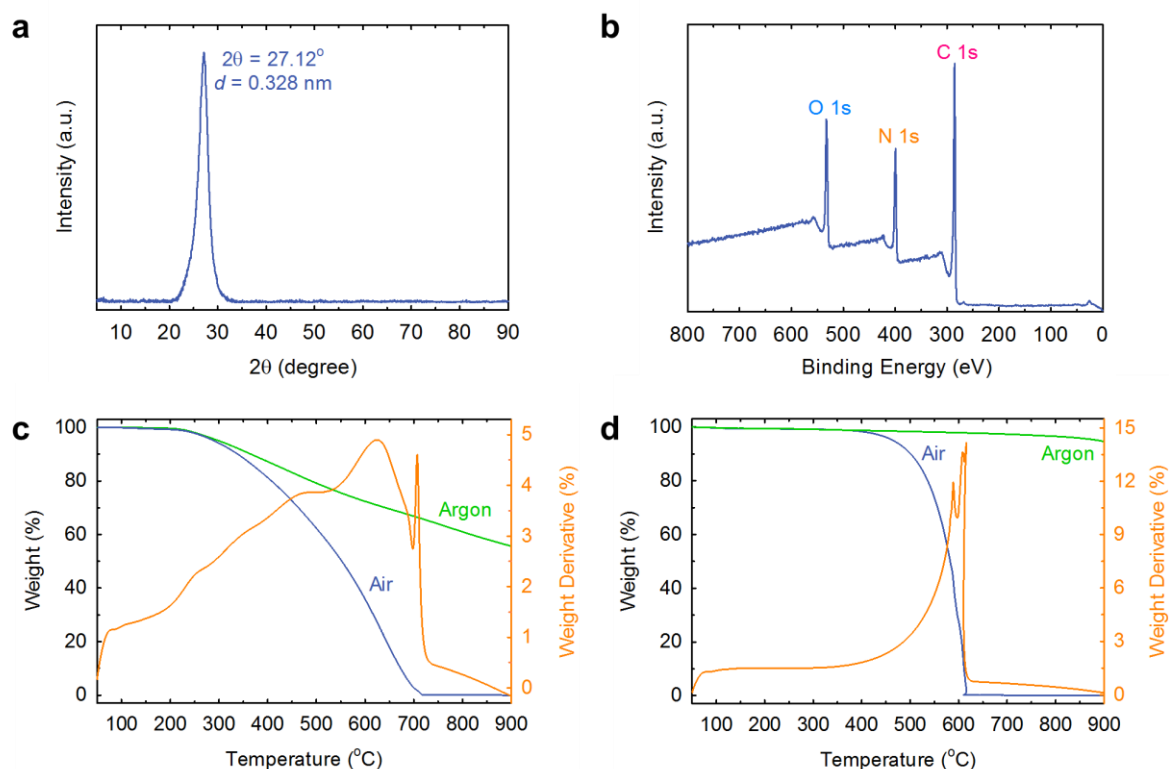


Figure 2.4. Analysis of the as-prepared C_2N -*h*2D crystal: (a) Powder XRD pattern from the as-prepared sample; (b) XPS survey spectrum showing C1s, N1s and O1s. High resolution XPS spectra for C1s, N1s and O1s are presented in Fig. S3. TGA thermograms obtained with a heating rate of 10 °C/min in air and argon: (c) As-prepared sample; (d) Heat-treated sample at 700 °C.

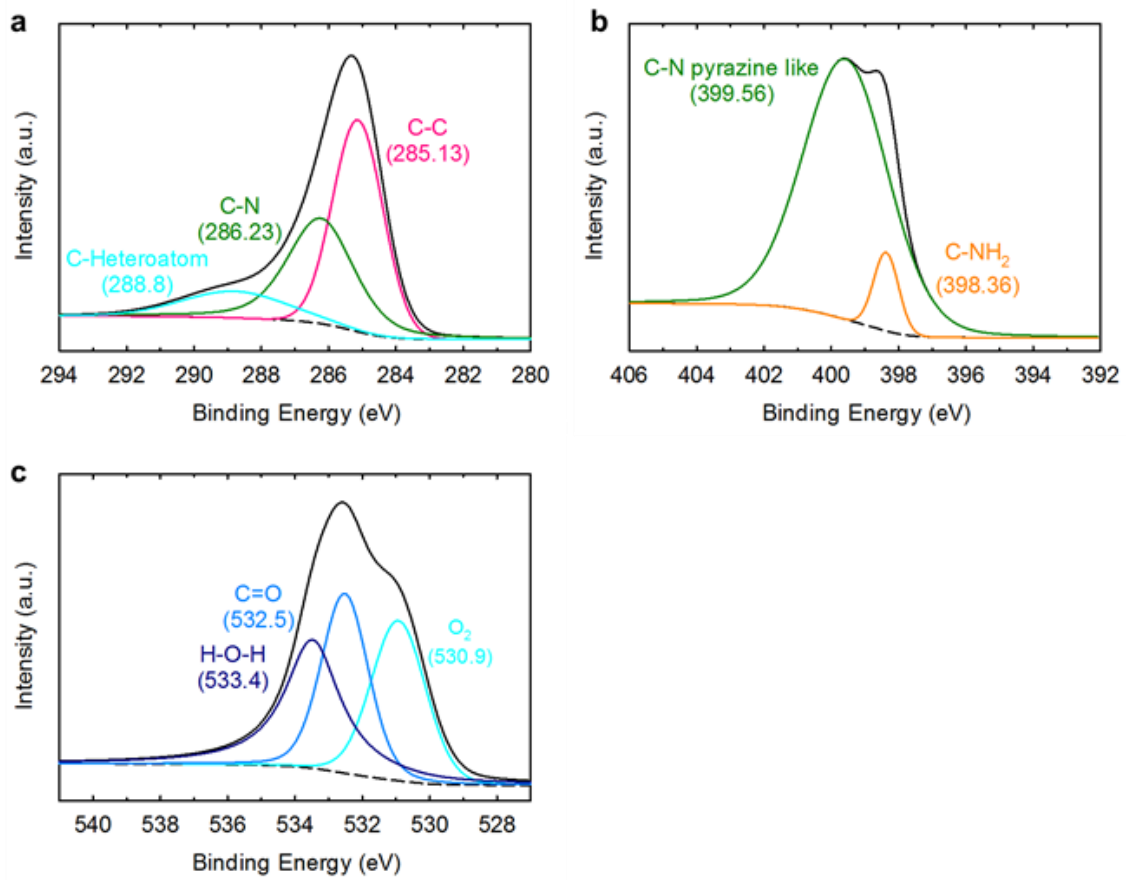


Figure 2.5. Deconvoluted XPS spectra of the C_2N - h_2D crystal: (a) C 1s. (b) N 1s. (c) O 1s.

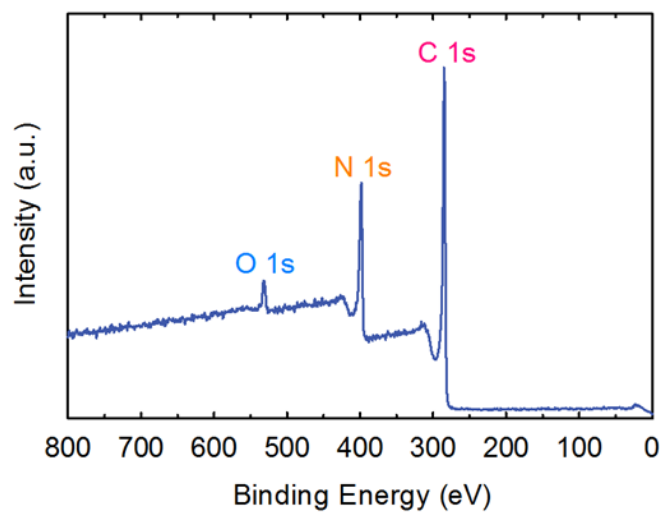


Figure 2.6. XPS survey spectrum of the heat-treated C_2N - h_2D crystal at 700 °C, showing C 1s, N 1s and reduced O1s compared with as-prepared spectrum (**Figure 2.4b**).

The bulk morphologies of the 2D crystal were probed with field emission scanning electron microscopy (FE-SEM). The grain size of as-prepared and heat treated samples are as large as a few hundred microns (**Figures 2.7a, 2.7b and 2.7c**). Transmission electron microscope (TEM) images were explored from the dispersed sample shown to be wrinkled morphology (**Figure 2.7d**), which can be associated to the flexible nature of the holey 2D structure²⁴. High magnification TEM image shows good crystallinity (**Figure 2.7e**) with interlayer d -spacing of 0.327 nm (**Figure 2.7f**), which is in good agreement with XRD result (0.328 nm). TEM element mappings obtained by energy-dispersive X-ray spectroscopy (EDS) and electron energy loss spectroscopy (EELS) demonstrate that element compositions of the sample are in accordance with theoretical counts (**Figure 2.8**). Uniform films with different thicknesses could also be cast on a SiO₂(300 nm)/Si wafer substrate (**Figures 2.1h and 2.9**).

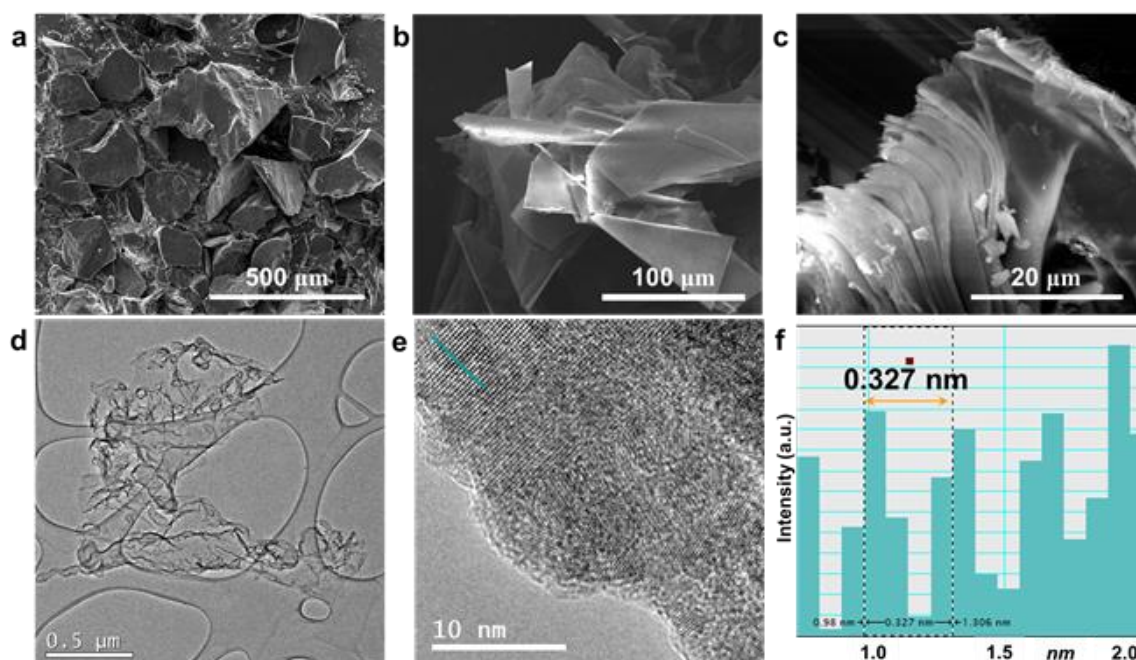


Figure 2.7. SEM images of the C₂N-*h*2D crystal: (a) As-prepared sample. (b) Heat-treated flakes. (c) Edge-on view of heat-treated flakes. TEM images of the C₂N-*h*2D crystal: (d) At low-magnification. (e) At high-magnification. (f) The interlayer distance ($d = 0.327$ nm) estimated along the dark green line in (e). The interlayer distance of 0.327 nm is very close to that obtained from XRD pattern (0.328 nm, **Figure. 2.4a**).

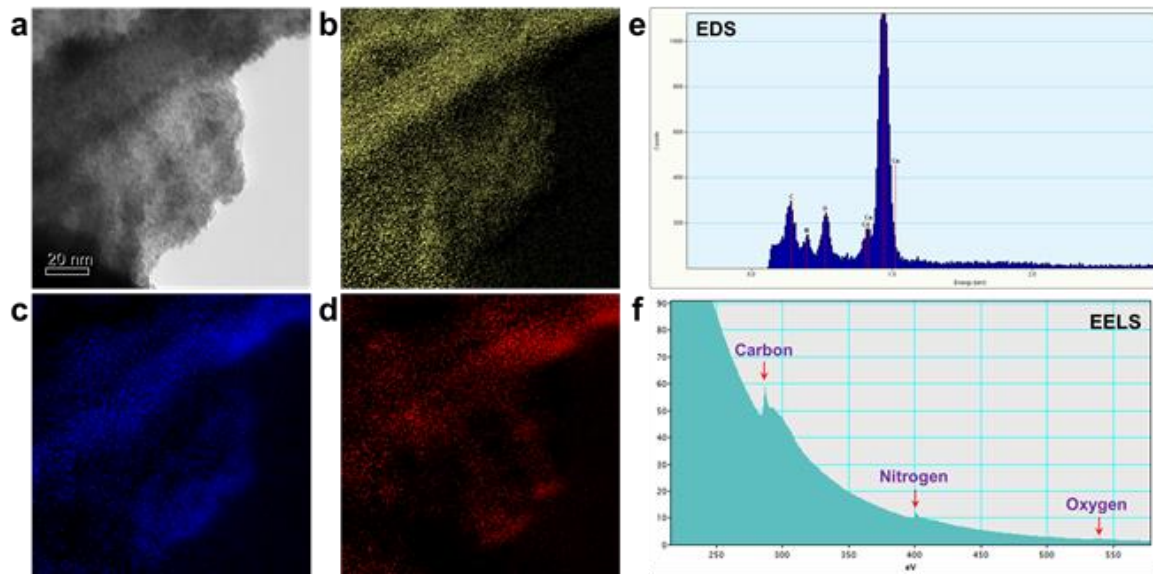


Figure 2.8. Energy-filtered TEM images of the as-prepared C_2N-h_2D crystal: (a) Zero-loss image. (b) Carbon mapping. (c) Nitrogen mapping. (d) Oxygen mapping. (e) Energy dispersive X-ray spectroscopy (EDX) spectrum showing the elemental composition (C, N and O) from the TEM image (a). (f) Electron energy loss spectroscopy (EELS) spectrum from the TEM image (a). Respective values of carbon, nitrogen and oxygen contents are very close to theoretical values.

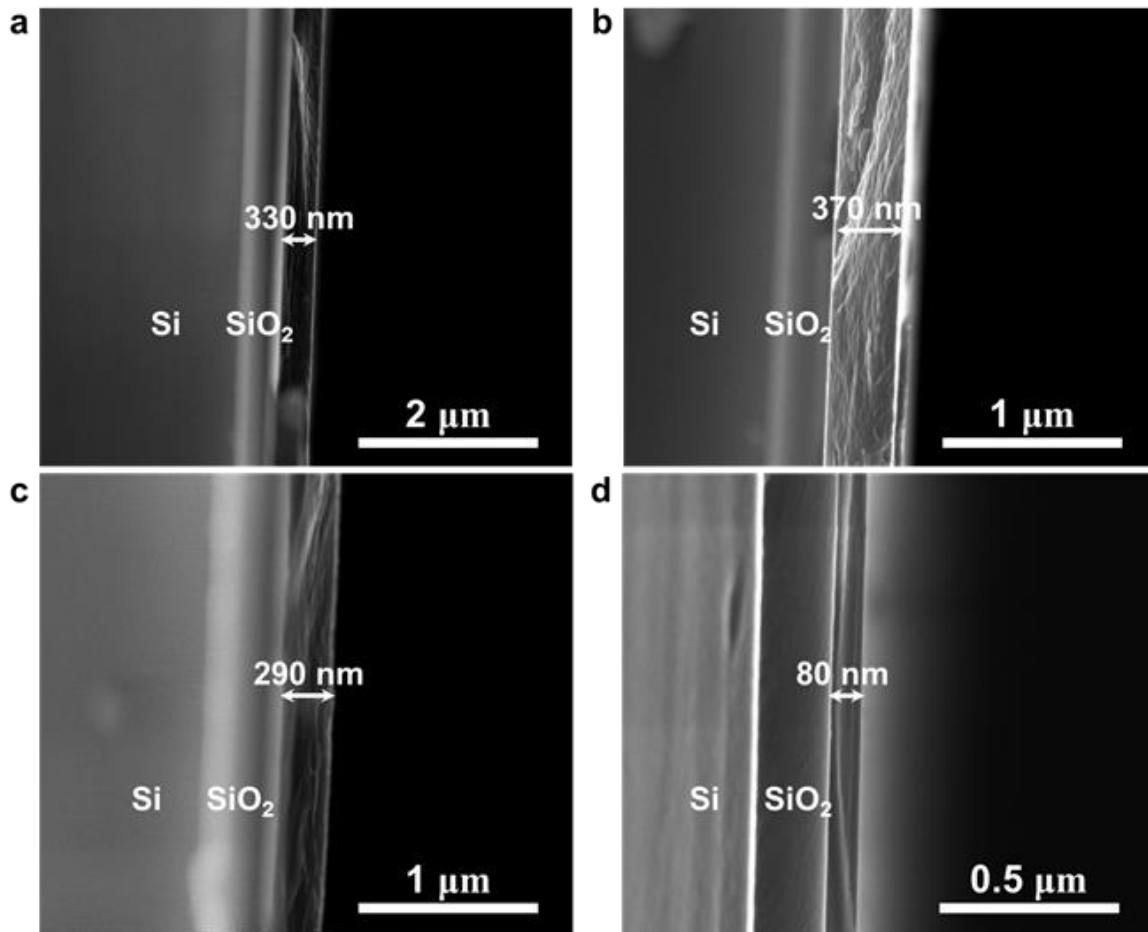


Figure 2.9. SEM images obtained from cross-section of the C_2N - $h2D$ crystal films on $SiO_2(300\text{ nm})/Si$ wafer with different thickness: (a) 330. (b) 370. (c) 290. (d) 80 nm.

In order to confirm the molecular structure of C_2N - $h2D$ crystal, I performed STM experiments. The single layer C_2N sample was deposited thermally on Cu(111) substrate under ultrahigh vacuum (UHV) condition. **Figure 2.10a** shows the high-resolution STM image of C_2N - $h2D$ monolayer on the Cu(111) substrate. The STM image obviously shows the evenly distributed hole structure in hexagonal arrays, which is precisely matched with theoretically obtained image (**Figure 2.10b**). The inter-hole distance obtained from the height profiles and 2D-FFT image is about $8.24 \pm 0.96 \text{ \AA}$ (**Figures 2.10c and 2.10d**). The height difference between hole and hexagonal lattice is $2.68 \pm 0.17 \text{ \AA}$, and the carbon rings were imaged slightly higher than C-N regions, which is contributed to the narrower interlayer d -spacing than those of graphite and h -BN (**Figures 2.11a and 2.11b**). The result is correlated to the XRD (3.28 \AA , **Figure 2.4a**) and TEM results (3.27 \AA , **Figure 2.7f**).

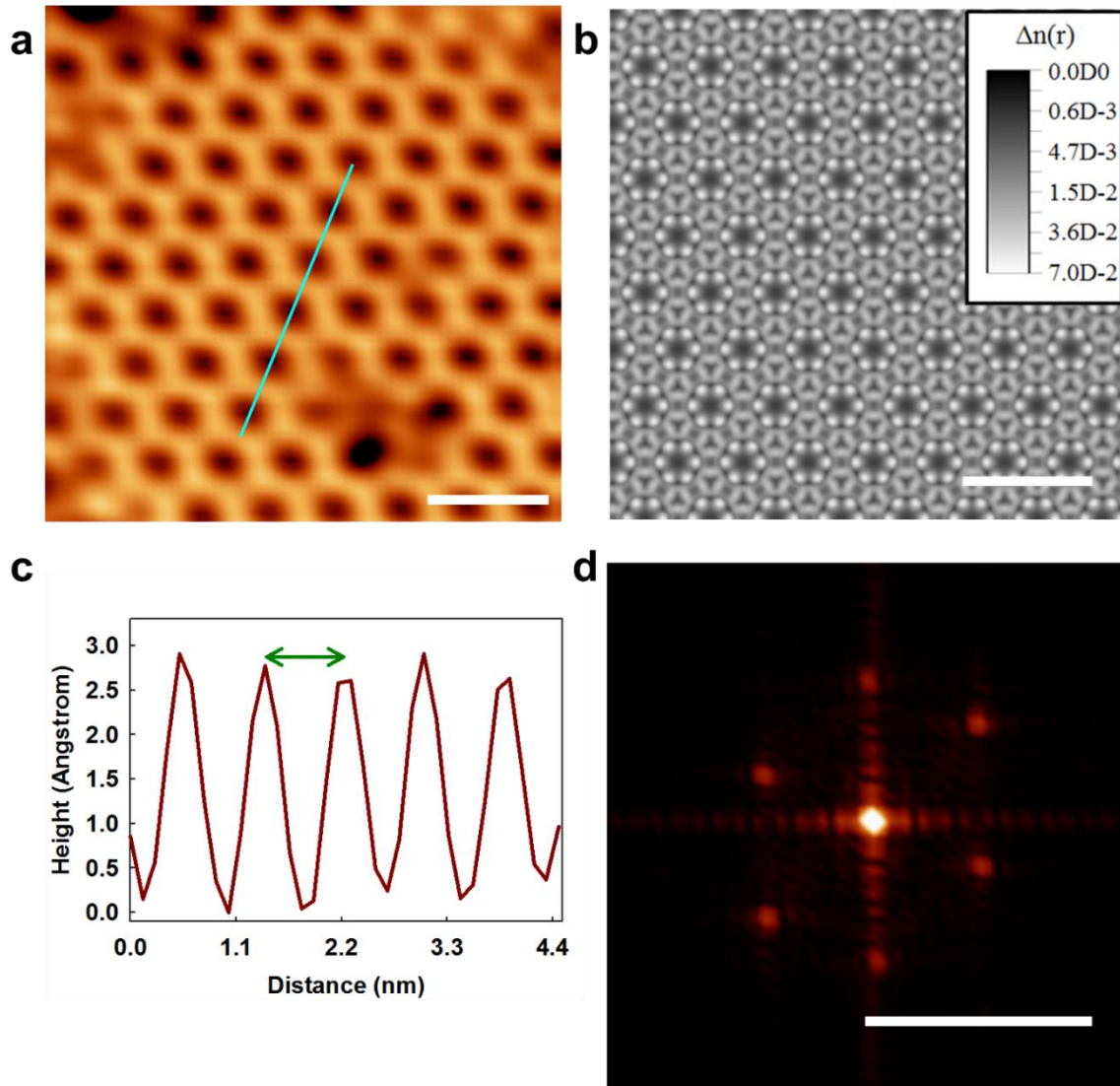


Figure 2.10. Atomic-resolution imaging of C_2N - $h2D$ crystal: (a) An STM topography image of C_2N - $h2D$ on Cu(111); (b) Theoretically calculated image; (c) Topographic height profile along the sky blue line marked in (a); (d) 2D fast Fourier Transformation of (a). The STM image was obtained at the sample bias of 0.7 V, and the tunneling current of 300 pA. The scale bars in (a), (b) and (d) are 1.6, 1.9 nm and 1.9 nm^{-1} , respectively.

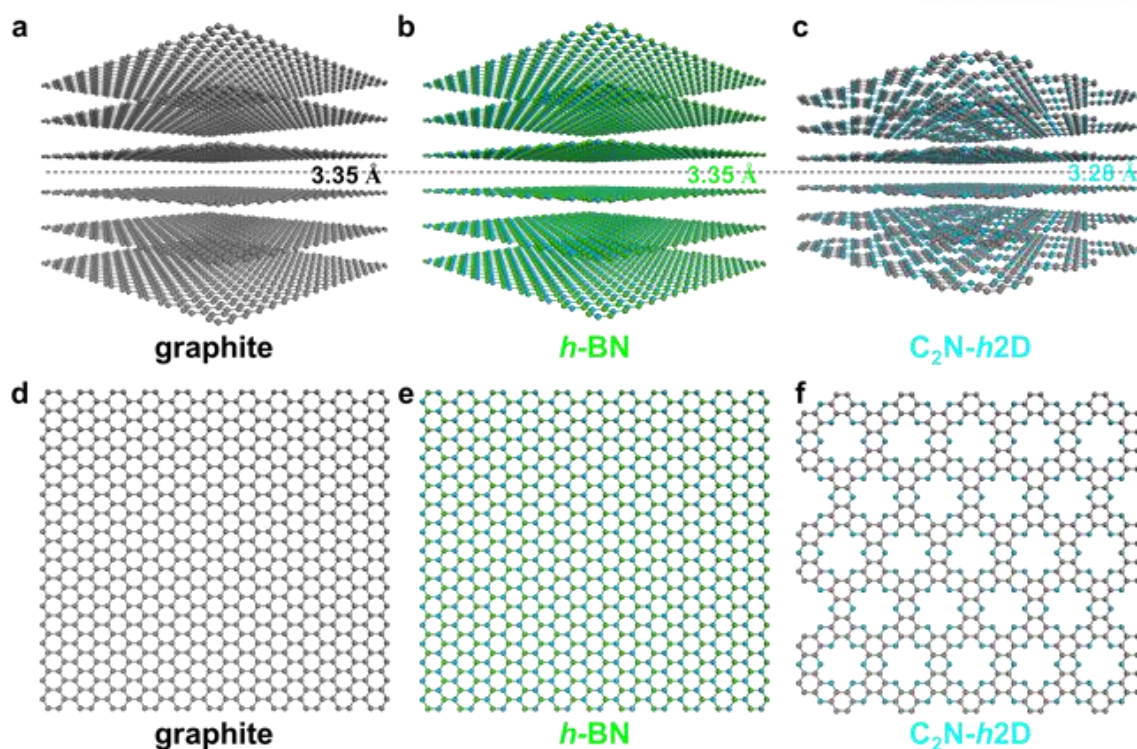


Figure 2.11. Comparison of interlayer distances: (a) Graphite. (b) *h*-BN. (c) C₂N-*h*2D crystal. Due to the differences in atomic sizes (covalent radii, B = 85, C = 77, N = 70 picometers), stacking patterns and charge polarizations, graphite and *h*-BN have very similar interlayer distance of 3.35 Å, while the C₂N-*h*2D crystal has lower interlayer distance (3.28 Å). Structures of representative single layer 2D crystals: (d) Graphene. (e) *h*-BN. (f) C₂N-*h*2D crystal.

The mostly investigated 2D crystals such as graphene (**Figures 2.11a and 2.11d**) and *h*-BN (**Figures 2.11b and 2.11e**) are radically distinct in terms of electronic structure in spite of the very close geometrical resemblance. For example, graphene is a conductor with a vanishing band-gap²⁵, while *h*-BN is an insulator with a wide band-gap of 5.05-6.40 eV²⁵. Thus, it is interesting to investigate the electronic structure of newly-explored C₂N-*h*2D crystal. I have empirically determined the direct band-gap from the UV-vis spectroscopy (**Figure 2.12a**). It is ~2.00 eV, which is well in the range of semiconductor²⁶. To obtain the band structure of C₂N-*h*2D crystal, cyclic voltammograms (CV) was employed to investigate the onset reduction potential, which corresponds to the bottom of the conduction band, lowest unoccupied molecular orbital (LUMO). To acquire CV, C₂N-*h*2D was deposited on the glassy carbon working electrode. Relative to a Ag/Ag⁺ reference electrode, the onset reduction potential appears at -0.81 V. The LUMO was determined to be -3.63 eV, calculated from the reduction potential (**Figure 13**). From the direct optical band-gap of C₂N-*h*2D crystal (**Figure 12a**),

the top of the valence band, highest occupied molecular orbital (HOMO), was calculated to be at -5.63 eV. To investigate the LUMO energy level of the C₂N-*h*2D crystal, the cyclic voltammogram was measured by using a standard three-electrode system, which consists of a glassy carbon as the working electrode, a platinum mesh as the counter electrode, and a silver wire as the reference electrode. Acetonitrile containing 0.1 M tetrabutylammonium hexafluorophosphate (TBAPF₆) was used as the supporting electrolyte. The LUMO energy level of the C₂N-*h*2D crystal was calculated according to the following equations.

$$\text{Fc/Fc}^+: 0.36 \text{ V vs. Ag/Ag}^+$$

$$\text{LUMO (eV)} : -4.8 - (E_{\text{onset}} - \text{Fc/Fc}^+) = -4.8 - (-0.81 - 0.36) = -3.63 \text{ eV}$$

All electrochemical measurements were carried out under an ambient pressure and nitrogen atmosphere.

- Working electrode: glassy carbon
- Counter electrode: Pt mesh
- Reference: Ag wire
- Electrolyte: 0.1 M TBAPF₆ in acetonitrile
- Scan rate: 100 mV/s
- Preparation of the C₂N-*h*2D crystal on glassy carbon electrode: dropping and drying
- Fe/Fe⁺: 0.36 vs. Ag/Ag⁺
- E_{red} as -0.81 V,
- LUMO (eV) : -4.8 - (E_{onset} - Fc/Fc⁺) = -4.8 - (-0.81 - 0.36) = **-3.63 eV**
- HOMO (eV): -3.63 eV - 1.96 eV* = -5.59 eV

* The optical band-gap of -1.96 eV was used to estimate HOMO value.

The optical HOMO-LUMO gap was found to be 1.96 eV. The LUMO value can also be experimentally estimated by onset of the redox potentials taking the known reference level for ferrocene, 4.8 eV below the vacuum level according to the equation. In my experiments, ferrocene exhibits an E_{1/2}

with a 0.36 V vs. Ag/Ag⁺. The onset reduction potential of -0.81 V vs. Ag/Ag⁺ was determined by electrochemical measurements of the C₂N-*h*2D crystal. Based on these data, the HOMO and LUMO can be calculated to be -5.59 and -3.63 eV, respectively. HOMO was calculated using the optical band-gap of 1.96 eV.

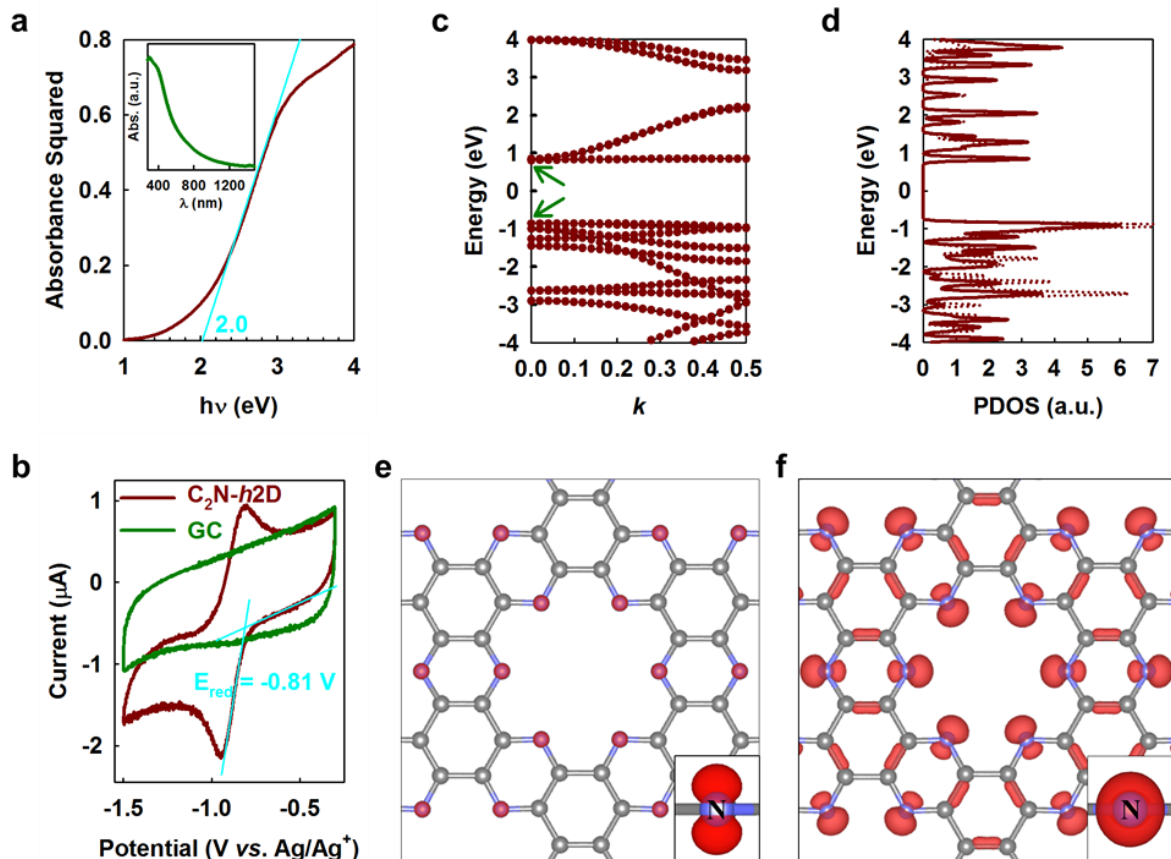


Figure 2.12. (a) Optical band-gap calculation and the absorbance squared vs. photon energy ($h\nu$) extrapolated to zero absorption. Inset is UV absorption curve. (b) Cyclic voltammograms of the C₂N-*h*2D crystal at a scan rate of 100 mVs⁻¹ using Ag/Ag⁺ reference electrode. (c) The band structure from the zone center to the X point of the 2-D triangular lattice. (d) The density of electronic states. An iso-surface plot of the Kohn-Sham orbital at the Gamma point: (e) Conduction band minimum state; (f) The doubly degenerate valence band maximum state.

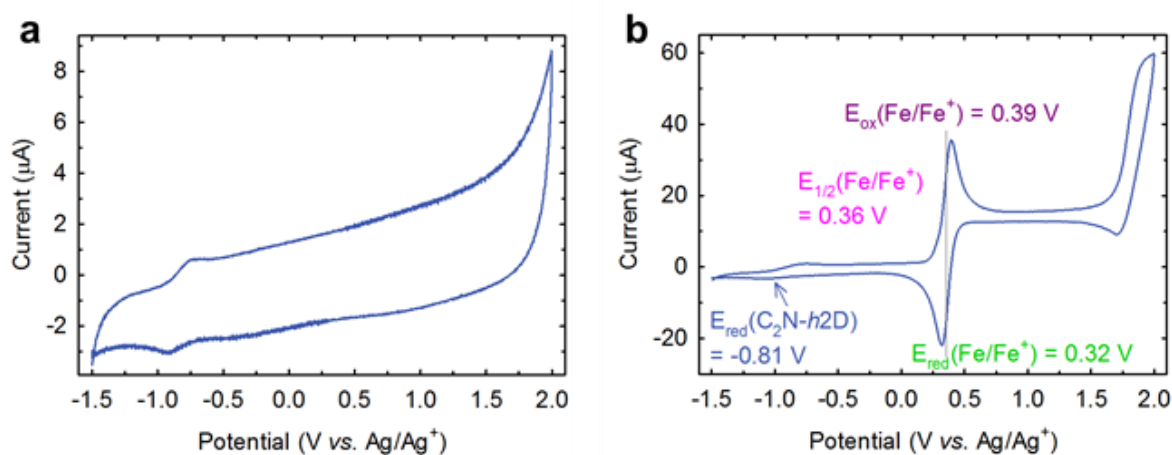


Figure 2.13. Cyclic voltammograms (CV) of the C_2N-h2D crystal on GC electrode at a scan rate of 100 mV s^{-1} using an Ag/Ag^+ reference electrode under N_2 atmosphere: (a) Whole range curve, showing no oxidation peak for the C_2N-h2D crystal. (b) C_2N-h2D crystal in the presence of ferrocene, which was used as reference material.

The first-principles density-functional theory (DFT) calculations were also done to look into the electronic structure of the C_2N-h2D crystal. The band structure along the symmetry line in the Brillouin zone and the density of electronic states are shown in **Figures 2.12c and 2.12d**, respectively. As a result of the gradient-corrected DFT calculations, the C_2N-h2D crystal shows a finite band-gap of $\sim 1.70 \text{ eV}$ (**Figure 2.12c**), whose value is smaller (by about $\sim 0.30 \text{ eV}$) than the optically determined value. The underestimation of the Kohn-Sham treatment of the DFT is well appreciated²⁷. The magnitude of the band-gap and the appearance of flat bands near the Fermi levels suggest that the C_2N-h2D crystal is an absolutely different 2D material compare with graphene and h -BN. In the C_2N-h2D crystal, the benzene rings are bridged by pyrazine like rings (six-membered D_{2h} ring with two nitrogen atoms facing each other (**Figures 2.1c and 2.2**). As such, the π electronic structure of the benzene ring is isolated, resulting in unusual flat bands (please note that graphene has cone-shaped bands) near the edges of the valence and conduction bands. The conduction band minimum consists of a flat band that originated from the localized p orbital of the nitrogen atoms (**Figure 2.12e**) and one dispersive band delocalized over the entire plane. The valence band maximum consists of doubly-degenerated flat bands, which mainly originated from the non-bonding σ states localized at the nitrogen atoms (**Figure 2.12f**). The flat bands near the band edges can be manipulated to create attractive phenomena. For example, an amount of hole-doping could result in a magnetic state whose spins originated from the two flat bands. Therefore, this material can offer complementary characteristics in comparison with the widely-studied graphene that has a vanishing band-gap (conductor) and an h -BN that has a wide band-gap (insulator).

To illustrate the electrical properties, field-effect transistors (FETs) were fabricated using C_2N - $h2D$ crystals as the active layer. A schematic of the details of film preparation by solution casting and device fabrication are presented in **Figure 2.14**. An elastomeric PDMS molds were synthesized by curing PDMS precursor (Sylgard 184, Dow Corning Corp) on a heat treated thin film of the C_2N - $h2D$ crystal on SiO_2/Si substrate in a flat plastic petri dish. The PDMS precursor and curing agent (10:1 by weight) were mixed and degassed under vacuum to completely remove the bubbles. After curing overnight at 70 °C under vacuum, the film was transferred to the PDMS stamp from the SiO_2/Si substrate. The PDMS stamp is then positioned over the SiO_2/Si substrate and is pressed gently for about 20 second. Then the stamp is slowly removed so that the thinner flakes of C_2N will remain on the cleaned SiO_2/Si substrate for device fabrication. By PDMS stamping I was able to get very thin sheet of C_2N for device fabrication and transport studies. In brief, 3-7 μL of solution (concentration, 0.1 mg mL^{-1}) in trifluoromethanesulfonic acid (TFMSA) was drop casted onto a SiO_2/Si wafer. After the slow evaporation of the solvent at 140 °C, the SiO_2/Si wafer was annealed at 700 °C. Then, a small amount of poly(dimethylsiloxane) (PDMS) precursor was poured onto the sample. After curing the PDMS, the SiO_2/Si wafer was detached away to obtain the sheets of the C_2N - $h2D$ crystal on another SiO_2/Si wafer substrate on gently pressing. The resulting C_2N - $h2D$ crystal flakes could be prepared over micron scale sizes (**Figure 2.15a**) with mechanical flexibility (**Figure 2.15b**). The crossing area of the stacked crystals was brighter than the other thin part (**Figure 2.15c**).

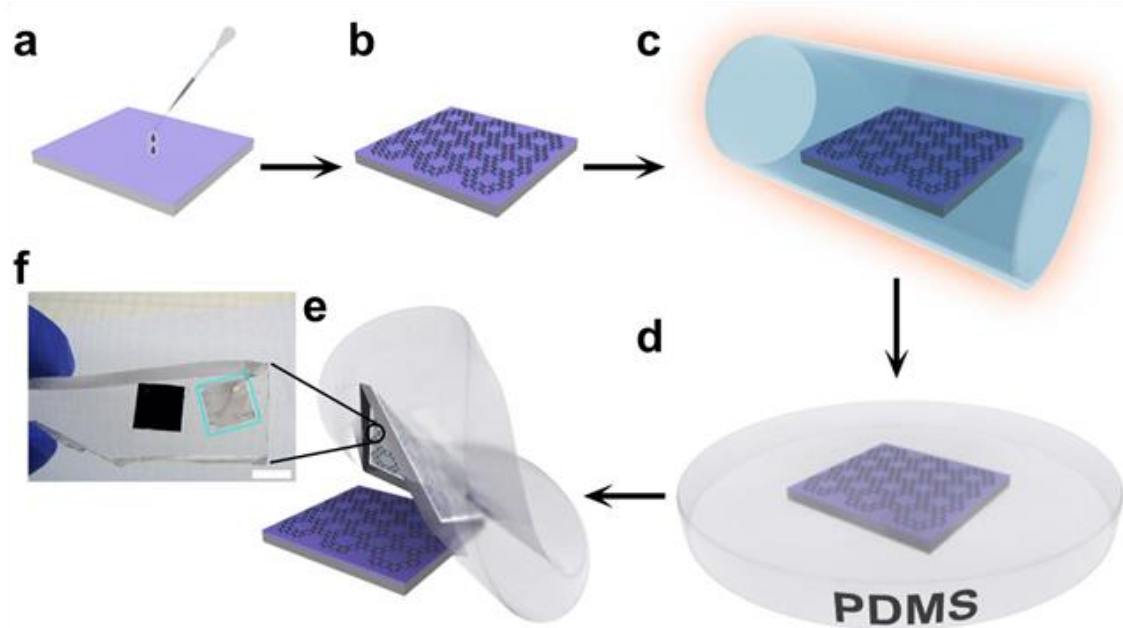


Figure 2.14. Schematic illustration for the film fabrication of the C_2N-h2D crystal using a PDMS mold: (a) 3–7 μL of the C_2N-h2D crystal solution was drop-coated onto the SiO_2/Si wafer using pipette. (b) The solution was slowly dried. (c) After cooling the sample to room temperature, the sample was annealed at 700 $^\circ\text{C}$ for 2 hours under argon atmosphere. (d) PDMS precursor was poured onto the sample film on SiO_2/Si wafer. (e) After curing the PDMS, which was carefully detached from the SiO_2/Si wafer. (f) Film attached to the PDMS after removing SiO_2/Si substrate is shown in the photograph (cyan blue square). Now the film can be transferred to any other desired substrate like SiO_2/Si wafer for device study. The scale bar is 1 cm.

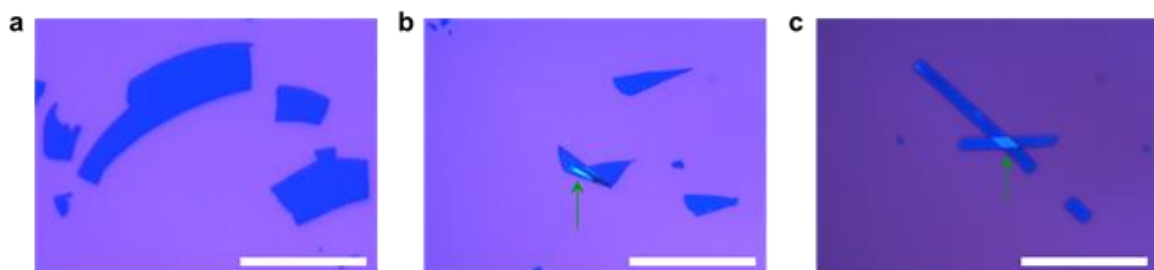


Figure 2.15. Optical images of the C_2N-h2D crystals on a SiO_2/Si wafer: (a) The C_2N-h2D crystal can be obtained over micron scale size. (b) The C_2N-h2D crystal is flexible (folded, cyan blue area). (c) Two C_2N-h2D crystal flakes have crossed (cyan blue area). All scale bars are 70 μm .

The optical images of typical C_2N-h2D crystal flakes are presented in **Figure 2.15**. Due to robust interlayer interactions, the isolation of a single layer was not possible using this method. Atomic force microscopy (AFM) analysis of the C_2N-h2D crystal flakes indicated that the average (mean) thickness of the sample (out of 10 samples) was 8.0 ± 3.5 nm (**Figure 2.16a**), implying that multilayers of the C_2N-h2D crystal were stacked. **Figure 2.16b** shows the optical image of the fabricated FET device, and the inset shows the C_2N-h2D crystals prior to the deposition of gold electrodes. The devices were annealed at 100 °C under reduced pressure (5×10^{-6} torr) to remove chemical impurities that might have been trapped and/or adsorbed into holes and interlayers during the fabrication process.

Typical transfer curves of the C_2N-h2D crystal FET devices are presented in **Figure 2.16c**, and the electrical properties of the C_2N-h2D crystals are summarised in **Table 2.2**. The on/off current ratio of the transistor was defined as the ratio between the maximum and minimum drain currents; the maximum on/off current ratio obtained from 50 FET devices was 4.6×10^7 .

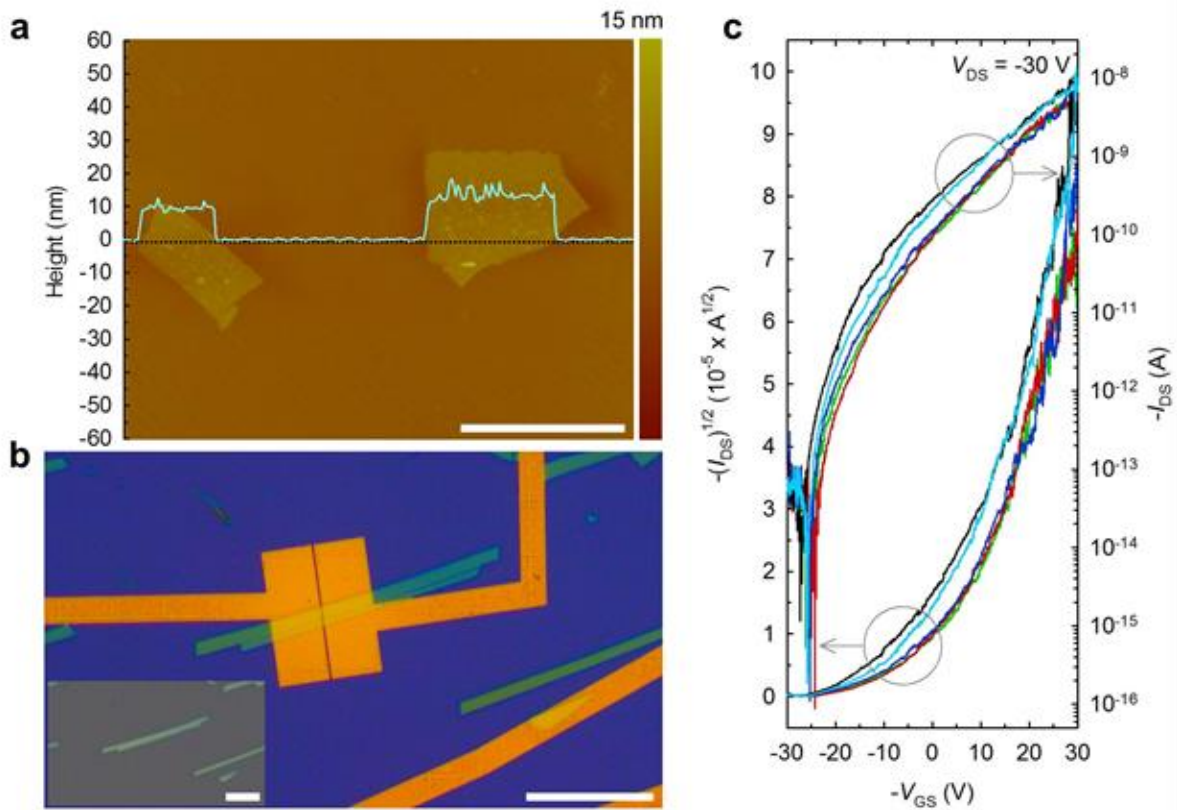


Figure 2.16. FET device study: (a) AFM image of the C₂N-h₂D crystal; the scale bar is 7 μm. The height profile (deep-blue line) was obtained along the dark-blue line. (b) Optical microscopy image of a C₂N-h₂D crystal field-effect transistor (FET) prepared on a SiO₂(300 nm)/n⁺⁺ Si wafer. The channel length (*L*) of the device is 500 nm, and the channel width-to-length (*W/L*) = 13. The inset is an optical microscopy image taken prior to the deposition of Au electrodes on the crystal. The scale bars are 60 μm. (c) Transfer curves of the C₂N-h₂D crystal FET devices measured at 25 °C under 5 × 10⁻⁶ torr (*V*_{DS} = -30 V).

Furthermore, when the off current was defined as the average drain current prior to the turn-on state, the average on/off current ratio remained as high as 2.1×10^5 with a standard deviation of $\pm 3.9 \times 10^5$. These results clearly reveal that the C₂N-h₂D crystals carry a band-gap. In addition, the corresponding output characteristics displayed well-defined field-effect characteristic under hole-enhanced operation (**Figure 2.17a**). As the work function of gold (approximately 5.10 eV) is much nearer to the HOMO level (-5.59 eV) of the C₂N-h₂D crystal than to its LUMO level (-3.63 eV), p-type operation is clearly favourable with gold electrodes (see **Figure 2.18** for the energy-level diagram). Interestingly, the C₂N-h₂D crystal exhibited semimetallic (graphene-like) behaviour before annealing (**Figure 2.17b**), showing ambipolar charge transport with a Dirac point of -7 V, an electron mobility of 13.5 cm²V⁻¹s⁻¹

and a hole mobility of $20.6 \text{ cm}^2\text{V}^{-1}\text{s}^{-1}$. The semimetallic behaviour is attributed to the unintentional doping effects by the trapped impurities and/or adsorbed gases in the holey $\text{C}_2\text{N-h2D}$ crystal structure, thereby indicating that the electronic properties of the $\text{C}_2\text{N-h2D}$ crystal are tuneable.

Table 2.2. Average (mean) electrical properties of the $\text{C}_2\text{N-h2D}$ crystal field-effect transistors

Electrical Characteristics ^a	Electrical Performance
Average off current ^b (A)	$7.1 (\pm 4.1)^c \times 10^{-14}$
Maximum on/off ratio ^d	4.6×10^7
Average on/off ratio ^e	$2.1 (\pm 3.9) \times 10^5$
Maximum mobility ($\text{cm}^2\text{V}^{-1}\text{s}^{-1}$)	1.3×10^{-2}
Average mobility ($\text{cm}^2\text{V}^{-1}\text{s}^{-1}$)	$6.5 (\pm 0.2) \times 10^{-3}$

^a 50 FET devices were measured under 5×10^{-6} torr.

^b The off current was averaged over the turn-off state.

^c The standard deviation.

^d Calculated with the minimum off current.

^e Calculated with the average off current.

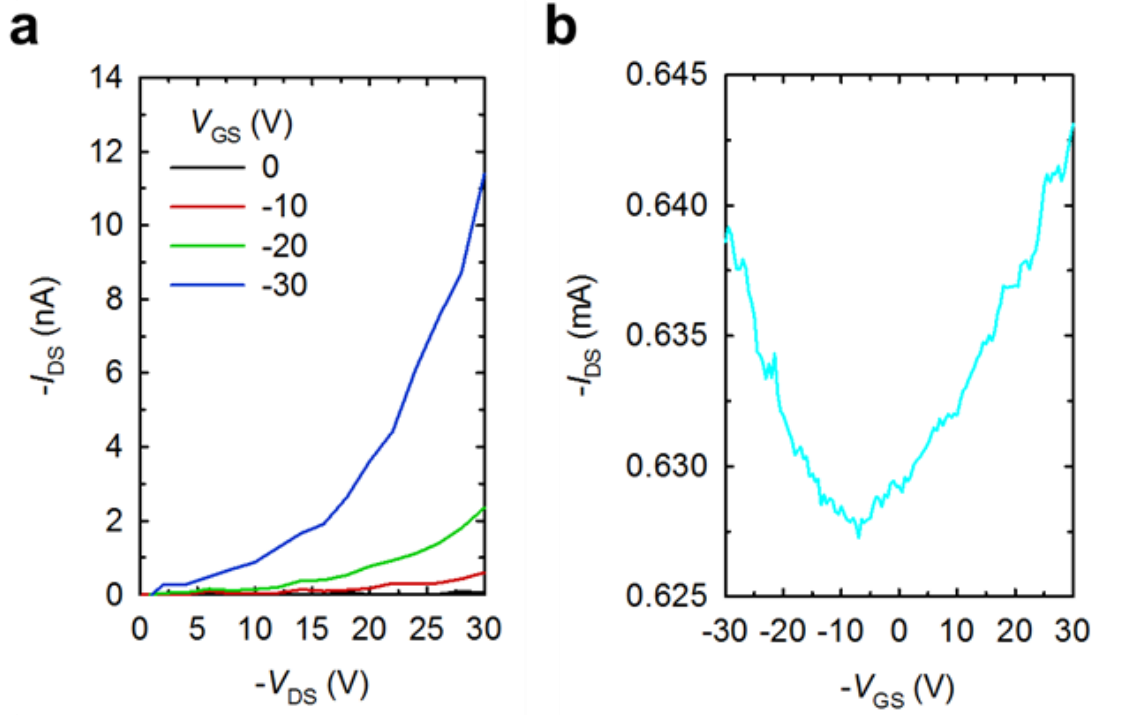


Figure 2.17. (a) Output curve after annealing at 100 °C under 5×10^{-6} torr ($V_{DS} = -30$ V). (b) Transfer curve of the C_2N-h2D crystal field-effect transistor before annealing. The characterization was performed at 25 °C under 5×10^{-6} torr.

Gold electrodes of the transistors were patterned with conventional e-beam lithography (the typical channel width-to-length ratio (W/L) = 13, $L = 500$ nm) to construct bottom-gate top-contact FET. The hole mobilities were extracted from the saturation regime of the transfer characteristics using the following equation:

$$I_{DS} = \frac{1}{2} \mu \frac{W}{L} C_i (V_{GS} - V_{th})^2$$

where I_{DS} is the drain current, μ is the field-effect mobility, C_i is the specific capacitance of the dielectric, V_{GS} is the gate voltage, V_{th} is the threshold voltage, and W and L are channel width and length.

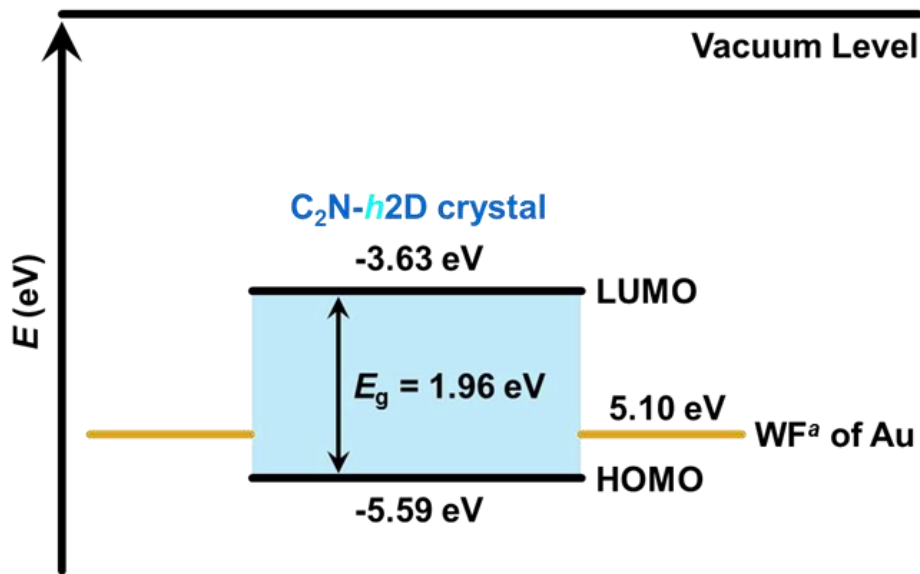


Figure 2.18. Energy level diagram of the C_2N-h2D crystal FET. The p -type operation of the FET is favorable with gold electrode according to the energy level diagram. ^a Work function.

As far as I know, the present work is the first preparation of a micron-size 2D holey crystal with a good crystallinity *via* a simple wet-logical reaction as a bottom-up approach without template assistance. The peculiar geometric and electronic structure of the C_2N-h2D crystal can be further explored as a lead to many applications, for which graphene and h -BN have inherent limitations. The comparisons between the C_2N-h2D crystal and other associated materials are given in **Figure 2.19**. For example, versatility stemming from evenly distributed holes and nitrogen atoms can be very interesting for many novel applications. For examples, purely organic non-metal magnetism after engineering a hole-doping level ²⁸, the size and shape selective absorption of transition metals and biomolecules *via* coordinative interactions ²⁹⁻³¹, and catalysis for the oxygen reduction reaction (ORR) ¹⁵. C_2N-h2D crystal has been preliminarily tested as a catalyst for simple organic reaction in benzene, model reaction is shown in **Figure 2.20**.

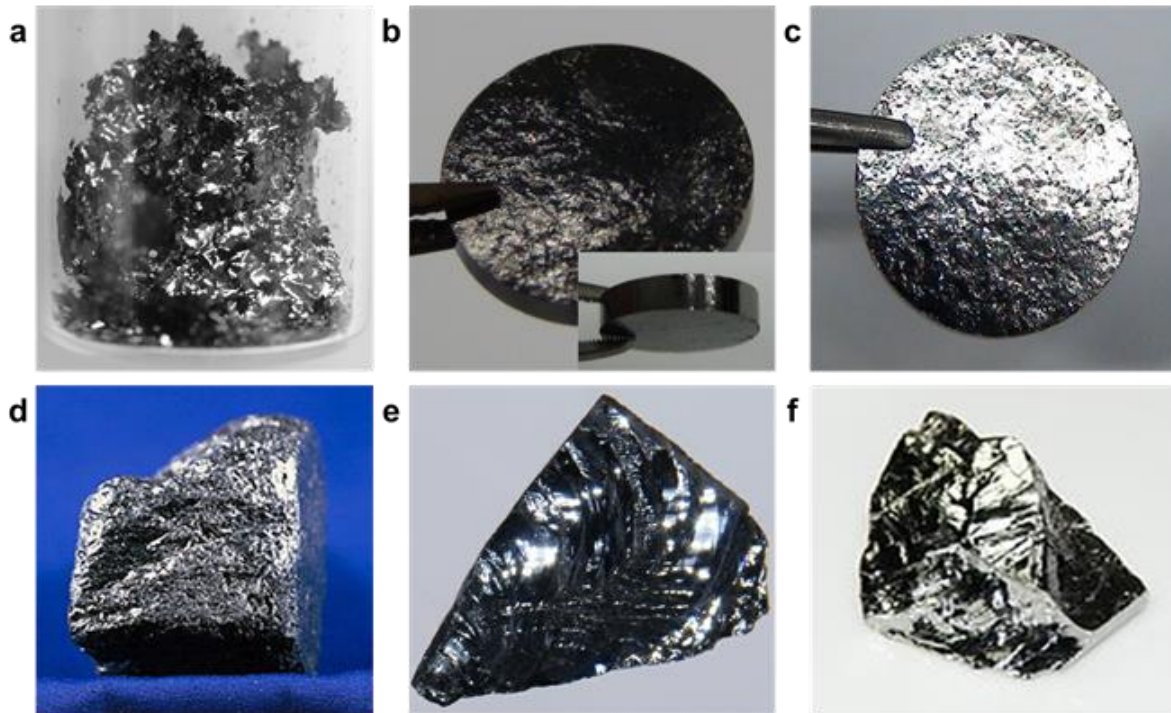


Figure 2.19. Photographs: (a) Heat-treated C_2N-h_2D crystal at 700 °C. (b) As-compressed C_2N-h_2D crystal pellet by approximately 9000 bars. Inset is side-view of the pallet. (c) After annealing at 700 °C. (d) Graphite ore (http://en.wikipedia.org/wiki/Graphite#cite_note-3). (e) Silicon ore (<http://images-of-elements.com/silicon.php>). (f) Germanium ore (<http://images-of-elements.com/germanium.php>). All cases are showing the surface in the shiny reflected light.



Figure 2.20. Schematic presentation of Knoevenagel condensation reaction of terephthalaldehyde and malononitrile in the presence of the C_2N-h_2D crystal as a reaction catalyst.

2.10 Conclusions

In summary, I have established that the third generation of graphitic structure, holey nitrogenated 2D crystal (designated as C_2N - h 2D crystal), can be easily synthesized by a bottom-up wet-chemical reaction. The crystal has uniformly distributed holes and nitrogen atoms in stacked structure with good crystallinity, and its structure was substantiated by atomic resolution STM imaging. It exhibits sp^2 hybridization characteristics with a semiconducting band-gap of ~ 2.0 eV (*ca.* 1.7 eV) with rare flat bands. In view of the established fabrication difficulties of the graphene and h -BN, the preparation of the C_2N - h 2D crystal is a easy and highly powerful method for the construction of 2D fused aromatic framework structure. This unique material would open up unusual opportunities for materials science and technology and thus widen the horizon of applications in electronics, sensors, catalysis and many more research opportunities, which can lead to complementary uses for graphene and h -BN. Furthermore, my success with the straightforward and efficient conceptual wet-chemistry based bottom-up approach coupled with multi-functionality of organic synthesis can open a new chapter to generate other 2D materials with possibly tuned properties through cost-effective ways, which will be a growing new area of research.

2.11 References

- (1) Novoselov, K. S.; Geim, A. K.; Morozov, S. V.; Jiang, D.; Zhang, Y.; Dubonos, S. V.; Grigorieva, I. V.; Firsov, A. A. Electric Field Effect in Atomically Thin Carbon Films. *Science* **2004**, *306*, 666.
- (2) Son, Y.-W.; Cohen, M. L.; Louie, S. G. Half-metallic graphene nanoribbons. *Nature* **2006**, *444*, 347.
- (3) Novoselov, K. S.; Jiang, D.; Schedin, F.; Booth, T. J.; Khotkevich, V. V.; Morozov, S. V.; Geim, A. K. Two-dimensional atomic crystals. *Proc. Natl. Acad. Sci. USA* **2005**, *102*, 10451.
- (4) Takamura, T.; Endo, K.; Fu, L.; Wu, Y.; Lee, K. J.; Matsumoto, T. Identification of nano-sized holes by TEM in the graphene layer of graphite and the high rate discharge capability of Li-ion battery anodes. *Electrochim. Acta* **2007**, *53*, 1055.
- (5) Schedin, F.; Geim, A. K.; Morozov, S. V.; Hill, E. W.; Blake, P.; Katsnelson, M. I.; Novoselov, K. S. Detection of individual gas molecules adsorbed on graphene. *Nat. Mater.* **2007**, *6*, 652.
- (6) Mas-Balleste, R.; Gomez-Navarro, C.; Gomez-Herrero, J.; Zamora, F. 2D materials: to graphene and beyond. *Nanoscale* **2011**, *3*, 20.
- (7) Sakamoto, J.; van Heijst, J.; Lukin, O.; Schlüter, A. D. Two-Dimensional Polymers: Just a Dream of Synthetic Chemists? *Angew. Chem. Int. Ed.* **2009**, *48*, 1030.

- (8) Perepichka, D. F.; Rosei, F. Extending Polymer Conjugation into the Second Dimension. *Science* **2009**, *323*, 216.
- (9) Jariwala, D.; Srivastava, A.; Ajayan, P. M. Graphene Synthesis and Band Gap Opening. *J. Nanosci. Nanotechnol.* **2011**, *11*, 6621.
- (10) Denis, P. A. Band gap opening of monolayer and bilayer graphene doped with aluminium, silicon, phosphorus, and sulfur. *Chem. Phys. Lett.* **2010**, *492*, 251.
- (11) Martins, T. B.; Miwa, R. H.; da Silva, A.; ocirc; nio, J. R.; Fazzio, A. lectronic and Transport Properties of Boron-Doped Graphene Nanoribbons. *Phys. Rev. Lett.* **2007**, *98*, 196803.
- (12) Wehling, T. O.; Novoselov, K. S.; Morozov, S. V.; Vdovin, E. E.; Katsnelson, M. I.; Geim, A. K.; Lichtenstein, A. I. Molecular Doping of Graphene. *Nano Lett.* **2007**, *8*, 173.
- (13) Lee, S. U.; Belosludov, R. V.; Mizuseki, H.; Kawazoe, Y. Designing Nanogadgetry for Nanoelectronic Devices with Nitrogen-Doped Capped Carbon Nanotubes. *Small* **2009**, *5*, 1769.
- (14) Wang, X.; Li, X.; Zhang, L.; Yoon, Y.; Weber, P. K.; Wang, H.; Guo, J.; Dai, H. N-Doping of Graphene Through Electrothermal Reactions with Ammonia. *Science* **2009**, *324*, 768.
- (15) Qu, L.; Liu, Y.; Baek, J.-B.; Dai, L. Nitrogen-Doped Graphene as Efficient Metal-Free Electrocatalyst for Oxygen Reduction in Fuel Cells. *ACS Nano* **2010**, *4*, 1321.
- (16) Wang, H.; Zhang, C.; Liu, Z.; Wang, L.; Han, P.; Xu, H.; Zhang, K.; Dong, S.; Yao, J.; Cui, G. Nitrogen-doped graphene nanosheets with excellent lithium storage properties. *J. Mater. Chem.* **2011**, *21*, 5430.
- (17) Gutzler, R.; Perepichka, D. F. π -Electron Conjugation in Two Dimensions. *J. Am. Chem. Soc.* **2013**, *135*, 16585.
- (18) Mahmood, J.; Kim, D.; Jeon, I.-Y.; Lah, M. S.; Baek, J.-B. Scalable Synthesis of Pure and Stable Hexaaminobenzene Trihydrochloride. *Synlett* **2013**, *24*, 246.
- (19) Schleyer, P. v. R. Introduction: Aromaticity. *Chem. Rev.* **2001**, *101*, 1115.
- (20) Jeong, H.-K.; Lee, Y. P.; Lahaye, R. J. W. E.; Park, M.-H.; An, K. H.; Kim, I. J.; Yang, C.-W.; Park, C. Y.; Ruoff, R. S.; Lee, Y. H. Evidence of Graphitic AB Stacking Order of Graphite Oxides. *J. Am. Chem. Soc.* **2008**, *130*, 1362.
- (21) Huang, H. G.; Wang, Z. H.; Xu, G. Q. The Selective Formation of Di- σ N-Si Linkages in Pyrazine Binding on Si(111)- 7×7 . *J. Phys. Chem. B* **2004**, *108*, 12560.

- (22) Kou, Y.; Xu, Y.; Guo, Z.; Jiang, D. Supercapacitive Energy Storage and Electric Power Supply Using an Aza-Fused π -Conjugated Microporous Framework. *Angew. Chem. Int. Ed.* **2011**, *50*, 8753.
- (23) Yang, S.; Feng, X.; Wang, X.; Müllen, K. Graphene-Based Carbon Nitride Nanosheets as Efficient Metal-Free Electrocatalysts for Oxygen Reduction Reactions. *Angew. Chem. Int. Ed.* **2011**, *50*, 5339.
- (24) Gu, W.; Zhang, W.; Li, X.; Zhu, H.; Wei, J.; Li, Z.; Shu, Q.; Wang, C.; Wang, K.; Shen, W.; Kang, F.; Wu, D. Graphene sheets from worm-like exfoliated graphite. *J. Mater. Chem.* **2009**, *19*, 3367.
- (25) Bao, Q.; Loh, K. P. Graphene Photonics, Plasmonics, and Broadband Optoelectronic Devices. *ACS Nano* **2012**, *6*, 3677.
- (26) Liu, S.; Guo, X.; Li, M.; Zhang, W.-H.; Liu, X.; Li, C. Solution-Phase Synthesis and Characterization of Single-Crystalline SnSe Nanowires. *Angew. Chem. Int. Ed.* **2011**, *50*, 12050.
- (27) Perdew, J. P.; Levy, M. Physical Content of the Exact Kohn-Sham Orbital Energies: Band Gaps and Derivative Discontinuities. *Phys. Rev. Lett.* **1983**, *51*, 1884.
- (28) Blundell, S. J.; Pratt, F. L. Organic and molecular magnets. *J. Phys.: Condensed Matter* **2004**, *16*, R771.
- (29) Merchant, C. A.; Healy, K.; Wanunu, M.; Ray, V.; Peterman, N.; Bartel, J.; Fischbein, M. D.; Venta, K.; Luo, Z.; Johnson, A. T. C.; Drndić, M. DNA Translocation through Graphene Nanopores. *Nano Lett.* **2010**, *10*, 2915.
- (30) Lu, C.-H.; Yang, H.-H.; Zhu, C.-L.; Chen, X.; Chen, G.-N. A Graphene Platform for Sensing Biomolecules. *Angew. Chem. Int. Ed.* **2009**, *48*, 4785.
- (31) Wang, Y.; Li, Z.; Wang, J.; Li, J.; Lin, Y. Graphene and graphene oxide: biofunctionalization and applications in biotechnology. *Trends in Biotechnol.* **2011**, *29*, 205.
- (32) Hohenberg, P. & Kohn, W. Inhomogeneous Electron Gas. *Phy. Rev.* **136**, B864-B871 (1964).
- (33) Kohn, W. & Sham, L. J. Self-Consistent Equations Including Exchange and Correlation Effects. *Phy. Rev.* **140**, A1133-A1138 (1965).
- (34) Kresse, G. & Furthmüller, J. Efficient iterative schemes for ab initio total-energy calculations using a plane-wave basis set. *Phy. Rev. B* **54**, 11169-11186 (1996).

- (35) Kresse, G. & Furthmüller, J. Efficiency of ab-initio total energy calculations for metals and semiconductors using a plane-wave basis set. *Comput. Mater. Sci.* **6**, 15-50 (1996).
- (36) Perdew, J. P., Burke, K. & Ernzerhof, M. Generalized Gradient Approximation Made Simple. *Phys. Rev. Lett.* **77**, 3865-3868 (1996).

III. C₃N 2D structure from carbonized single crystal

3.1 Abstract

Two dimensional (2D) heteroatom containing carbon nanomaterials represent a longstanding challenge and attracted huge interest beyond graphene due to their exceptional electronic and optoelectronic properties. Despite recent advances in materials science, scalable and easy methods to produce uniformly doped 2D materials are limited. Here, I introduce a new C₃N 2D material with uniformly placed nitrogen in the carbon framework by carbonization of hexaaminobenzene single crystals at 500 °C. The electronic and topological structure of the C₃N 2D crystal was studied by scanning tunneling microscopy (STM). The C₃N 2D crystal could be a new class of 2D materials with novel properties that can be emerged from their unique structure.

3.2 Introduction

New materials play an essential role in shaping new technology, and carbon and carbon-based materials have generated a lot of interest in different fields of science. The discovery of interesting new class of carbon-based structures with interesting structural, electrical and electrochemical properties, *e.g.*, fullerenes, carbon nanotubes and graphene provoked a new wave of interest in the scientific community^{1,2}. Real two-dimensional (2D) structures, termed as crystals with high aspect ratios and thickness corresponding to an atomic layer, have evolved huge curiosity recently. Graphene, the 2D form of carbon, also gathered substantial attention since 2004, when it was isolated into single atomic layers^{3,4}. Some of the promising properties⁵⁻⁹ of graphene make it possible replacement of indium tin oxide (ITO) in organic electronics, solar cells and electrochemistry. Although some significant steps have been made toward the application of this magical 2D material, absence of intrinsic band-gap in graphene^{10,11} diminishes its advantages in many applications. Recently, some of the 2D crystals of other materials similar to graphene¹²⁻¹⁴, which have attracted attention, comprised of transition metal dichalcogenides¹⁵, hexagonal boron nitride¹⁶, metal oxides and metal hydroxides¹⁷. A lot of researches has been performed on these reported 2D materials and scientific community is anxiously looking for 2D materials based carbon and heteroatoms¹⁸. Almost all the reported 2D materials suffer some weakness in the real applications. Hence, finding a new class of 2D materials is indispensable toward the advancement of science and technology¹⁴. Until now, a number of synthetic routes for other carbon-based 2D materials have been accomplished, but the quality and yield of the products are still very far away from the requirements for the practical utilization.¹⁹

3.3 Materials & Instrumentations

Hexaaminobenzene hydrochloride (HAB) was synthesized and its structure was confirmed by single crystal X-ray crystallography.²⁰ Room temperature Raman spectra were performed by Micro-Raman Alpha 300 R WITec with magnification 50x and helium-neon laser 532nm. Thermogravimetric analysis (TGA) was measured in air and nitrogen atmosphere at a heating rate of 10 °C/min using a Thermogravimetric Analyzer Q200 TA Instrument, USA. Scanning electron microscope (SEM) images were carried out on Field Emission Scanning Electron Microscope Nanonova 230 FEI, USA. X-ray photoelectron spectroscopy (XPS) was conducted on X-ray Photoelectron Spectroscopy Thermo Fisher K-alpha (UK). X-ray diffraction (XRD) studies were measured on High Power X-ray Diffractometer D/MAZX 2500V/PC (Cu-K α radiation, 35 kV, 20 mA, $\lambda = 1.5418 \text{ \AA}$) Rigaku, Japan.

3.4 Synthesis of carbonized single crystal rods (C₃N framework)

2 gram of the HAB crystals were taken in aluminum oxide crucible and put in the furnace and degassed the chamber three times by argon and high vacuum pump. Then the furnace temperature was raised, under reduced pressure and argon (10 cc/min) flow, to 500 °C in two hours. The temperature was maintained at 500 °C for three hours with continuous flow of argon and reduced pressure (initial pressure 4.5×10^{-4} , and under argon 1.9×10^{-3} torr). Then cooled down to room temperature and collected the sample, yield = 770 mg, which is almost quantitative.

3.5 Measurement of HOMO and LUMO gap

To investigate the HOMO and LUMO energy level of C₃N, the cyclic voltammogram of C₃N was measured by using a standard three-electrode system, which consists of a glassy carbon as the working electrode, a platinum mesh as the counter electrode, and a silver wire as the reference electrode. Acetonitrile containing 0.1 M tetrabutylammonium hexafluorophosphate (TBAPF₆) was used as the supporting electrolyte. The HOMO and LUMO energy level of C₃N was calculated according to the following equations.

$$\text{Fc/Fc}^+: 0.40 \text{ V vs. Ag/Ag}^+$$

- HOMO (eV) = $-4.8 - (E_{\text{ox}} - \text{Fc/Fc}^+) = -4.8 - (1.35 - 0.40) = -5.75 \text{ eV}$
- LUMO (eV) = $-4.8 - (E_{\text{red}} - \text{Fc/Fc}^+) = -4.8 - (-1.32 - 0.40) = -3.08 \text{ eV}$
- Band gap (E_{gap}) = $-3.08 \text{ eV} - (-5.75 \text{ eV}) = 2.67 \text{ eV}$

All electrochemical measurements were carried out under an atmospheric pressure of N₂.

- Working electrode: Glassy carbon
- Counter electrode: Pt mesh
- Reference: Ag wire
- Electrolyte: 0.1 M TBAPF₆ in Acetonitrile
- Scan rate: 100 mV/s
- Preparation of HAB on glassy carbon electrode: dropping and drying
- Fe/Fe⁺: 0.40 vs. Ag/Ag⁺
- E_{ox} as 1.35 V
- E_{red} as -1.32 V

The electrochemical band gap (HOMO-LUMO gap) was found to be 2.67 eV. The HOMO and LUMO value can also be experimentally estimated by the onset of the redox potentials taking the known reference level for ferrocene, 4.8 eV below the vacuum level, according to the following equation: In my experiments, ferrocene exhibits a ½ peak potential with a 0.40 V vs. Ag wire. The electrochemical measurements of C₃N show an onset oxidation potential of +1.35 V and onset reduction potential of -1.32 V vs. Ag wire. Based on these data, The HOMO/LUMO can be calculated as -5.75 and -3.08 eV, respectively.

3.6 Results and Discussion

An organic single crystal is a solid in which the molecules are periodically stacked by chemical bonds across its whole volume. The unique repeating pattern offers good opportunities to construct well-defined structures and to search new important applications. I, for the first time, synthesized hexaaminobenzene hydrochloride (HAB) in pure and crystalline form²⁰. While checking the melting point, I observed that HAB carbonizes before its melting; maintaining the needle like well-defined crystal shape. Here, I focus on the carbonization of hexaaminobenzene hydrochloride single crystal at 500 °C into a hexagonal rod like structures, which resembles covalently bonded hexagonal shaped 3D layered structure. The HAB single crystals were directly carbonized into rigid hexagonal rods without melting. At first place, the HAB converts into polyaniline like structure and then forms 2D layered structure with removal of ammonium chloride (**Figures 3.1a and 3.2**). This process is reproducible and the resultant materials are stable. The measurements reported here were made on samples from three different batches, each sample prepared at the same condition. Annealing of the HAB was carried out

in argon atmosphere under reduced pressure (10^{-4} torr). During annealing the HAB single crystal first forms 3D polyaniline (3D-PANI) type structure, and then 3D-PANI on further annealing with release of ammonium chloride results into a graphitic network structure²¹. 3D-PANI cannot maintain the initial structure at 500 °C, even at above 200 °C PANI starts forming cross-linked structure^{22,23}. I, for the first time, report serendipitous discovery of a new type of 2D layered material. The proposed novel structure was confirmed by scanning tunneling microscopy (STM) and many other characterization techniques to support the proposed structure. This novel material manifests the possibility of next generation layered 2D structure with interesting properties.

The elemental composition calculated from the different technique is very close to the calculated value (**Table 3.1**). The empirical formula of the material is C_3N for the core network and C_3NH for the whole molecule, considering the edge amine functional groups in the bulk structure (**Figure 3.1b**). Initial confirmation of this novel structure was performed by using solid-state carbon nuclear magnetic resonance (^{13}C -NMR) measurement, revealing only two peaks at 126.02 and 150.80 ppm (**Figure 3.3b**). Peak at 150.80 ppm is for the carbon inside the framework attached with tertiary nitrogen and the peak at 126.02 ppm is assignable to the carbon at the edges covalently bonded with the primary or secondary amine (**Figure 3.3b**).

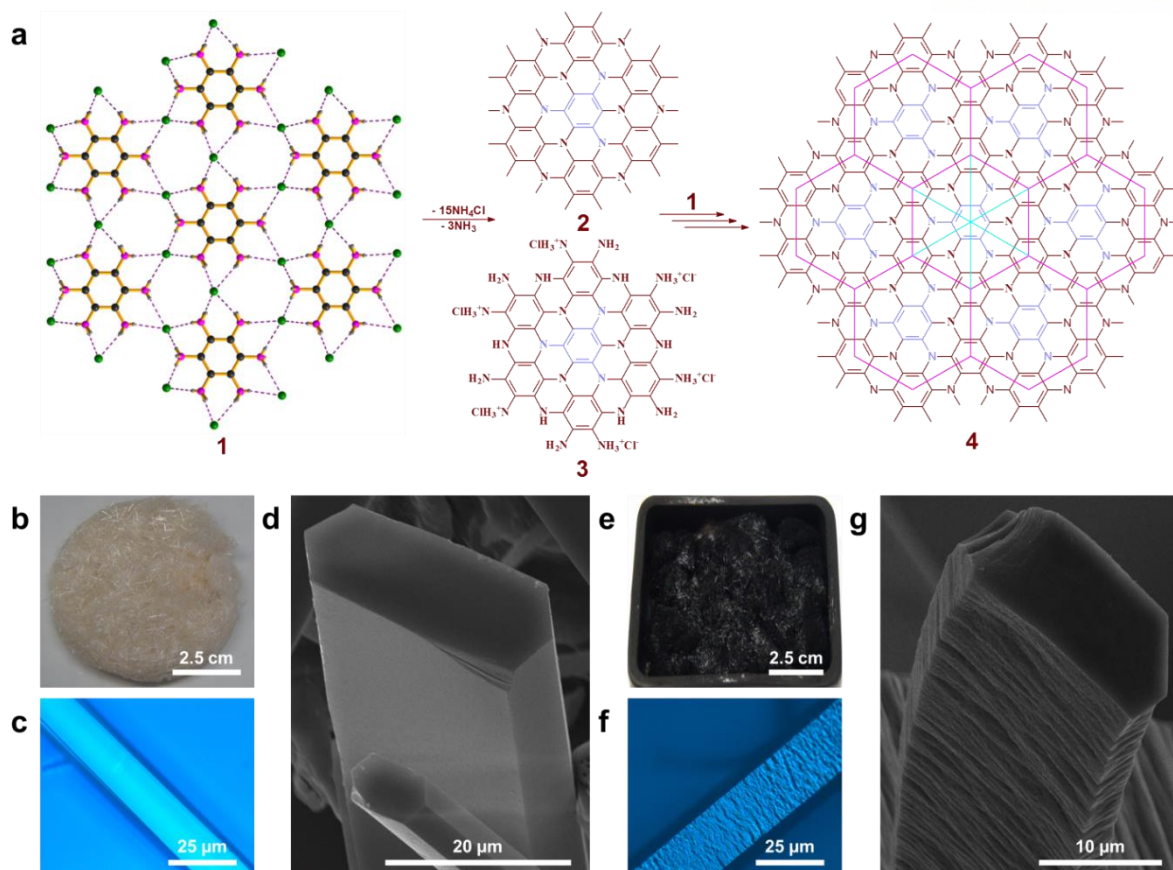


Figure 3.1. Schematic representation of C₃N formation. (a), Single-crystal x-ray packing structure of HAB (1) and schematic representation of the spontaneous transformation of HAB into the 2D C₃N crystal (2, 3, 4); (b), digital photograph of HAB crystals on butter paper; c, optical microscopy image of a needle-like HAB crystal before annealing; (d), SEM image of an HAB single crystal; e, digital image of HAB after annealing at 500 °C; (f), optical microscopy image of HAB crystals after annealing at 500 °C; (g), SEM image of a 2D C₃N single crystal.

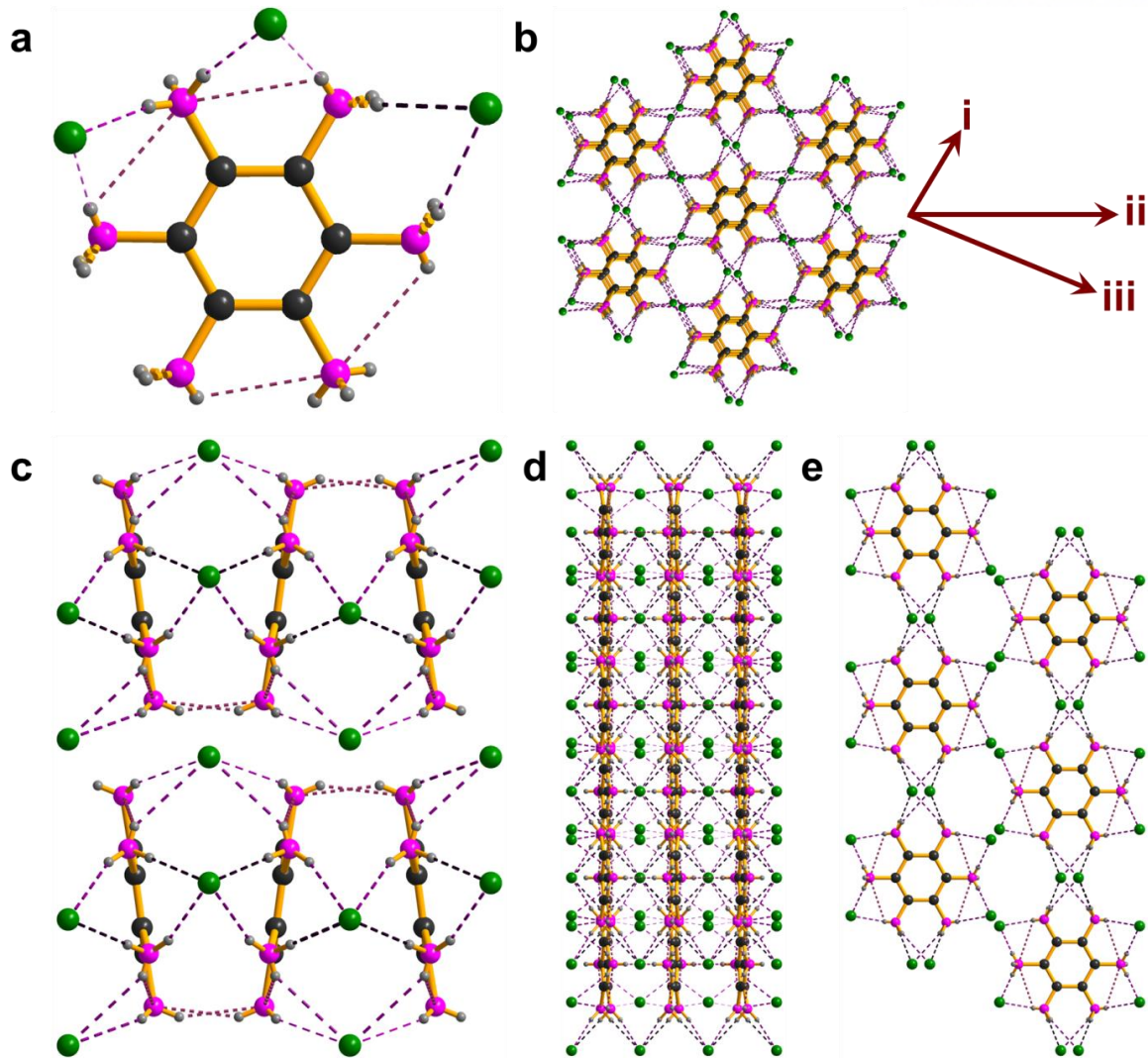


Figure 3.2. Single crystal structure of HAB: (a), formula unit; (b), hydrogen-bonded three layers of HAB crystal; (c), hydrogen-bonded packing a-direction view in (b); (d), hydrogen-bonded packing b-direction view in (b); (e), hydrogen-bonded packing c-direction view in (b).

The chemical composition and nature of possible bonds were probed with XPS measurement (**Figure 3.3d**). The survey scan spectrum from the XPS reveals only C 1s, N 1s and O 1s without any other impurities (**Figure 3.3d**). The characteristic band for the K-edge of nitrogen appeared at 398.6 and 400.2 eV, showing the edge-amines (C-N) and tertiary nitrogen attached with three aromatic carbon atoms in the new structure. From high resolution spectrum, C 1s can be deconvoluted into three peaks at 284.6 and 285.6 288.5 eV. The peaks at 284.6 and 285.6 eV are assigned to sp^2C-C and sp^2C-N , respectively, in the framework, while the minor peak at 288.5 is ascribed to C-NH₂ at the edges. The N 1s spectrum shows two peaks at 398.6 and 400.6 eV for sp^2C_2-NH and sp^2C_3-N in the network. The small oxygen content (O 1s) in the structure can be attributed to the adsorbed molecular oxygen and bound moisture (**Figure 3.4**),^{24,25} because I started from the single crystal of HAB, whose structure was confirmed by single crystal X-ray. All the results point towards the novel conceived structure. TGA showed that the synthesized sample showed good thermal stability both in air and nitrogen atmosphere (**Figure 3.3b**). BET specific surface area of the material determined by nitrogen adsorption/desorption method is about 54.4 m²g⁻¹, which is an indication of highly ordered and mesoporous structure. The powder XRD pattern of the C₃N shows major peak at 25.8 °, whose value tallies with interlayer distance (*d*-spacing) of 0.35 nm, which supports the formation of the proposed 2D sheet-like structure. There are other small and broad peaks at 43.99 and 12.29 °. The micro-Raman spectrum of the C₃N framework shows prominent peaks at 1510 and 1370 cm⁻¹ that correspond to the D and G bands respectively. The presence of G band is an indication of the ordered 2D nature of the material and high ratio of the D band is associated with edge contribution and sp^3 nitrogen in the structure.

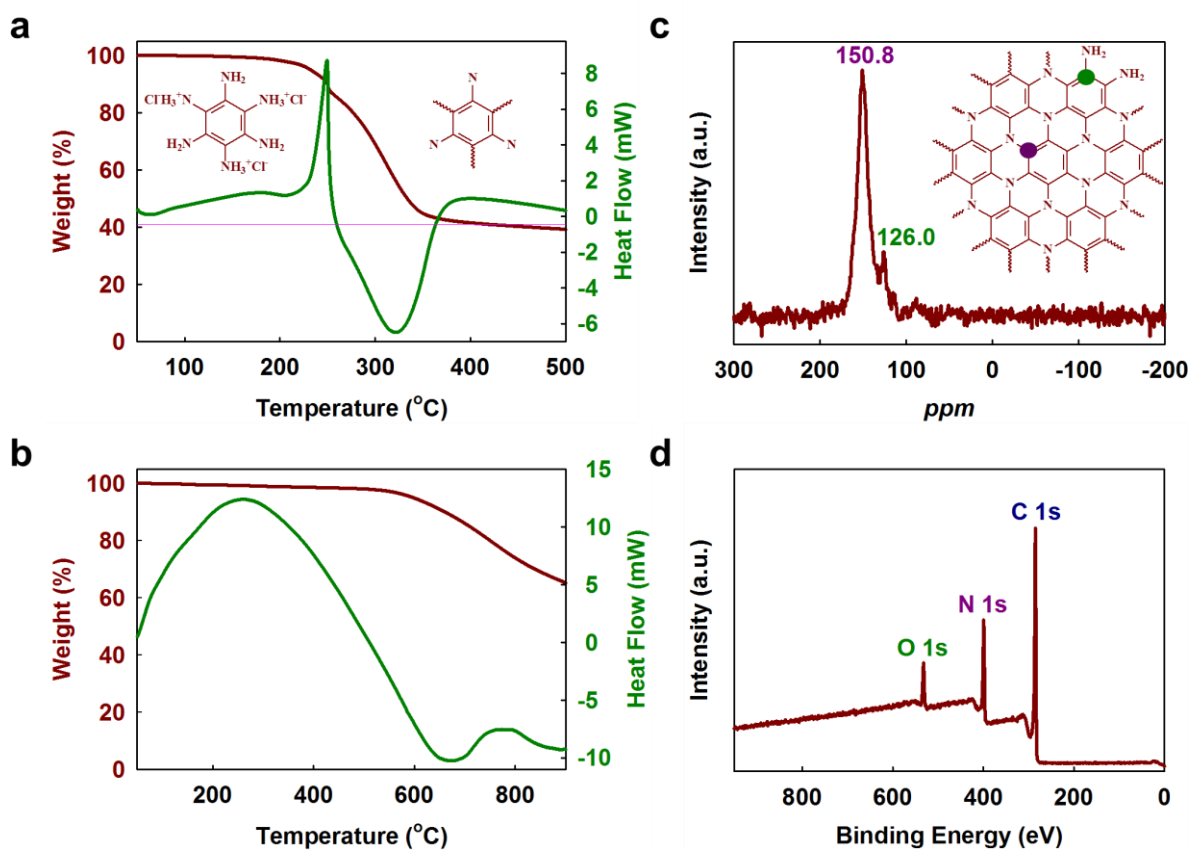


Figure 3.3. Characterisation of the C₃N structure. (a), TGA thermogram of an HAB single crystal with a ramping rate of 10 °C/min; (b), TGA thermogram of a 2D C₃N crystal after annealing at 500 °C; (c), solid-state ¹³C magic-angle spinning (MAS) NMR spectrum of C₃N crystals; (d), XPS survey spectrum of C₃N crystals. High-resolution XPS spectra are presented in **Figure 3.4**.

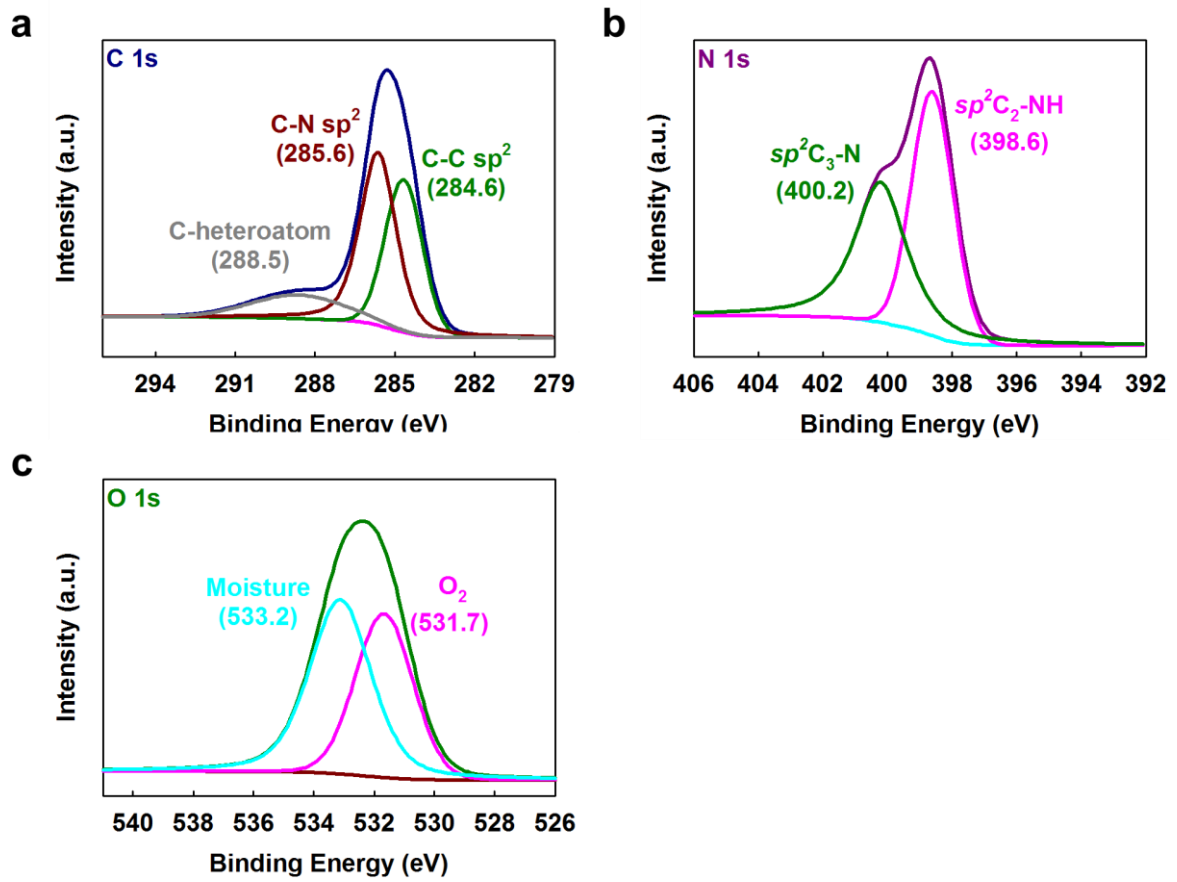


Figure 3.4. High-resolution XPS spectra of C₃N framework: (a), C 1s; (b), N 1s; (c), O 1s.

Table 3.1. Elemental composition of the C₃N framework from different characterization techniques

Technique	C	H	N	O	Total
Theoretical (wt%)	61.54	2.58	35.88	0	100
EA (wt%)^a	59.74	1.92	26.16	11.31	99.13
SEM EDS (wt%)	60.38	NA ^b	34.71 ^c	4.91 ^d	100

^a EA is most reliable element counts for bulk sample. The more oxygen content could be because of the adsorbed moisture and oxygen. As the starting material is pure single crystal, so only possibility for oxygen content is adsorbed oxygen on the C₃N framework.

^b NA = Not available.

^{c,d} The increased nitrogen content and decreased oxygen content in EDS is due to removal of adsorbed oxygen in high vacuum condition.

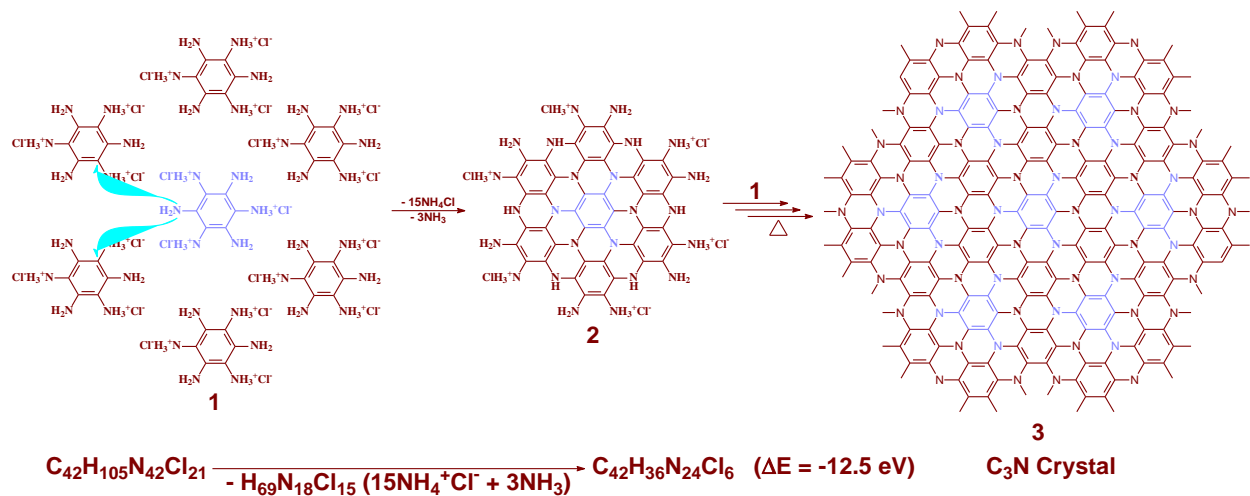


Figure 3.5. Mechanistic presentation of the C₃N framework with edge groups.

To confirm the unusual chemistry I carried out TGA on pure HAB crystals under nitrogen atmosphere to check the behavior of the HAB crystals on gradual increase of temperature. The monomer show endothermic weight loss associated with 15% mass loss at around 250 °C. This weigh loss is partial removal of the ammonium chloride (NH₄Cl) to form 2D PANI type structure. At around 325 °C, the reaction is highly exothermic, which is associated with 42% mass loss, indicating the formation of new bonds and stable structure with release of remaining ammonium chloride (**Figure 3.3a**). To check the nature of the gases coming out during annealing of the HAB monomer, I performed Py-GC-MS (Pyrolysis coupled GC-MS). Py-GC-MS clearly shows the major peak for the removal of HCl. Py-GC-MS was unable to detect the ammonia because of small size, which is out of detection limit. Alternatively, I confirmed the formation of ammonium chloride by chemical method. During the annealing of the HAB monomer in quartz tube furnace ammonium chloride is released and deposited in the tube outside the furnace as ammonium chloride crystals, whose melting point is 340 °C (sublimation). The deposited material was collected from the furnace tube and washed with chloroform to give white compound. Then basic chemical tests were carried out to check ammonium and chloride ion in the solution. Chloride was detected by using silver nitrate solution, which precipitates chloride ion forming silver chloride, giving white precipitate (**Figure 3.6b**). To identify ammonia, sodium hydroxide was added to the collected white crystals and heated by heat gun. On heating ammonia is released and detected by damp pH paper which turns dark green at the mouth of the test tube (**Figure 3.6d**). These experiments were repeated and reproduced with commercial chemicals as well.

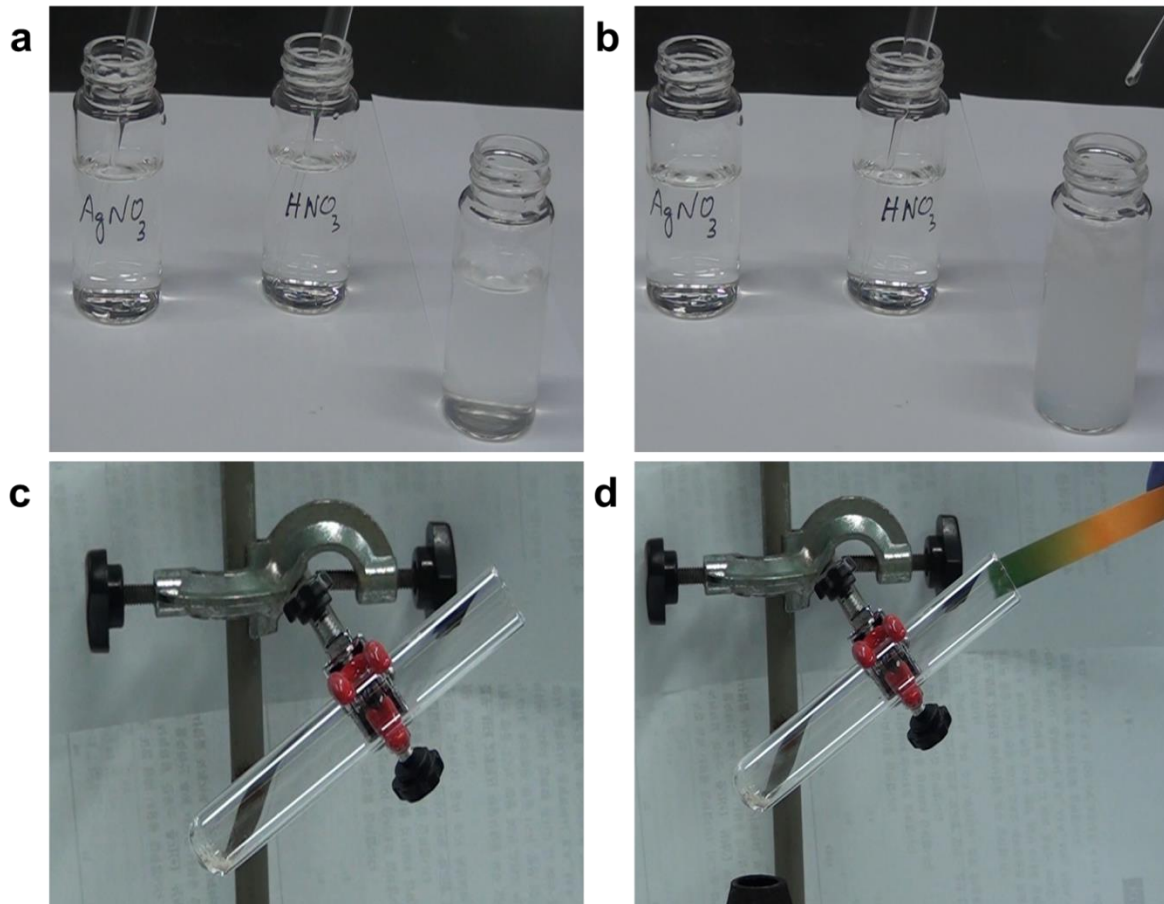


Figure 3.6. (a), Before addition of AgNO_3 to the sample; (b), after addition of AgNO_3 , white precipitation appeared, indicating the presence of chloride ion $\text{HAB} + \text{HNO}_3 + \text{AgNO}_3 \rightarrow \text{AgCl}$ (white precipitation in water); (c), Mixture of HAB and NaOH, before heating; (d), after heating the mixture, pH paper at the mouth of the test tube turn deep green, showing the release of ammonia as follow: $\text{NH}_4^+\text{Cl}^- + \text{Na}^+\text{OH}^- \rightarrow \text{NaCl} + \text{H}_2\text{O} + \text{NH}_3$.

The surface morphology of the HAB crystals and prepared C_3N framework was studied with FE-SEM, (**Figures 3.7 and 3.9**), disclosing hexagonal rod like structure reaching up to few millimeter long. High resolution SEM shows more like graphitic structure with stacked layered and highly wrinkled morphology, which is ascribed to the 2D nature of the C_3N framework and sheet-like appearance. SEM morphologies of the C_3N are well supporting each other and very unique and specific to this material. The hexagonal shape of the HAB crystals is well maintained in the structure after carbonization. Energy dispersive spectroscopy (EDS) from the SEM reveals the elemental composition of the materials, indicating the complete removal of chlorides from the material (**Figures 3.8 and 3.10**).

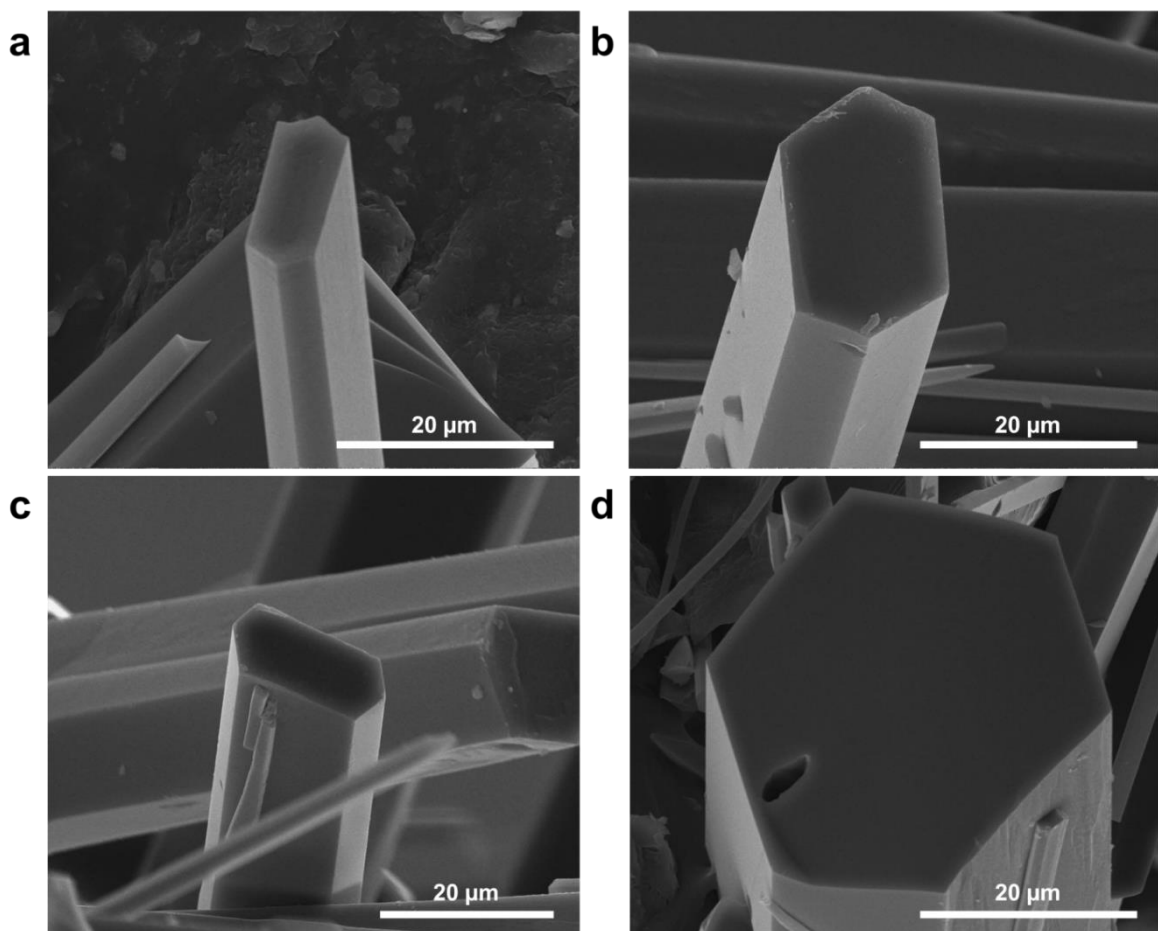


Figure 3.7. SEM images of the pure HAB crystals show well define hexagonal rod like framework from different crystals.

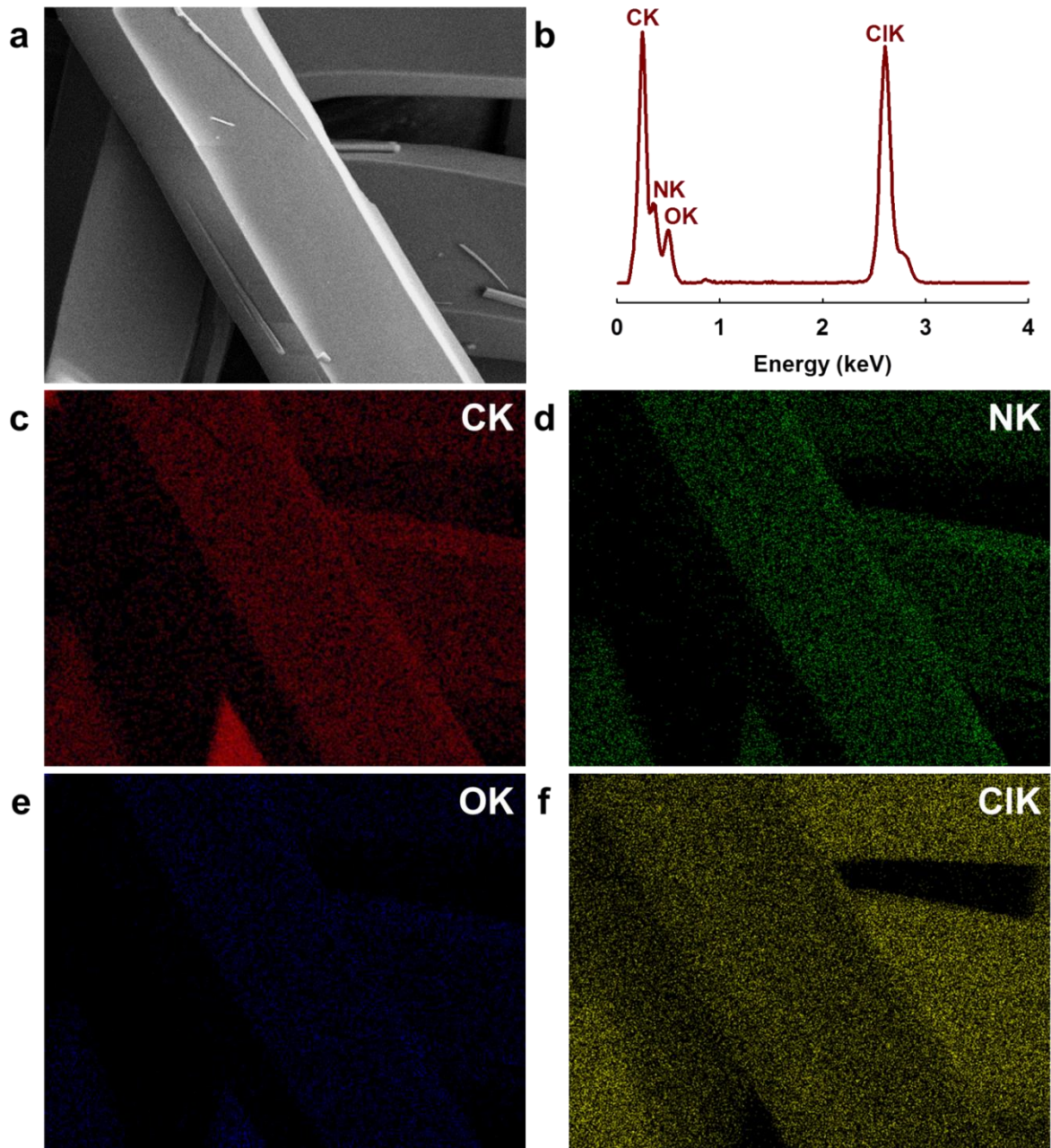


Figure 3.8. SEM energy dispersive X-ray spectroscopy (EDS) showing the elemental composition of the hexaaminobenzene hydrochloride (HAB) (C, Cl, N and O) from the corresponding SEM image.

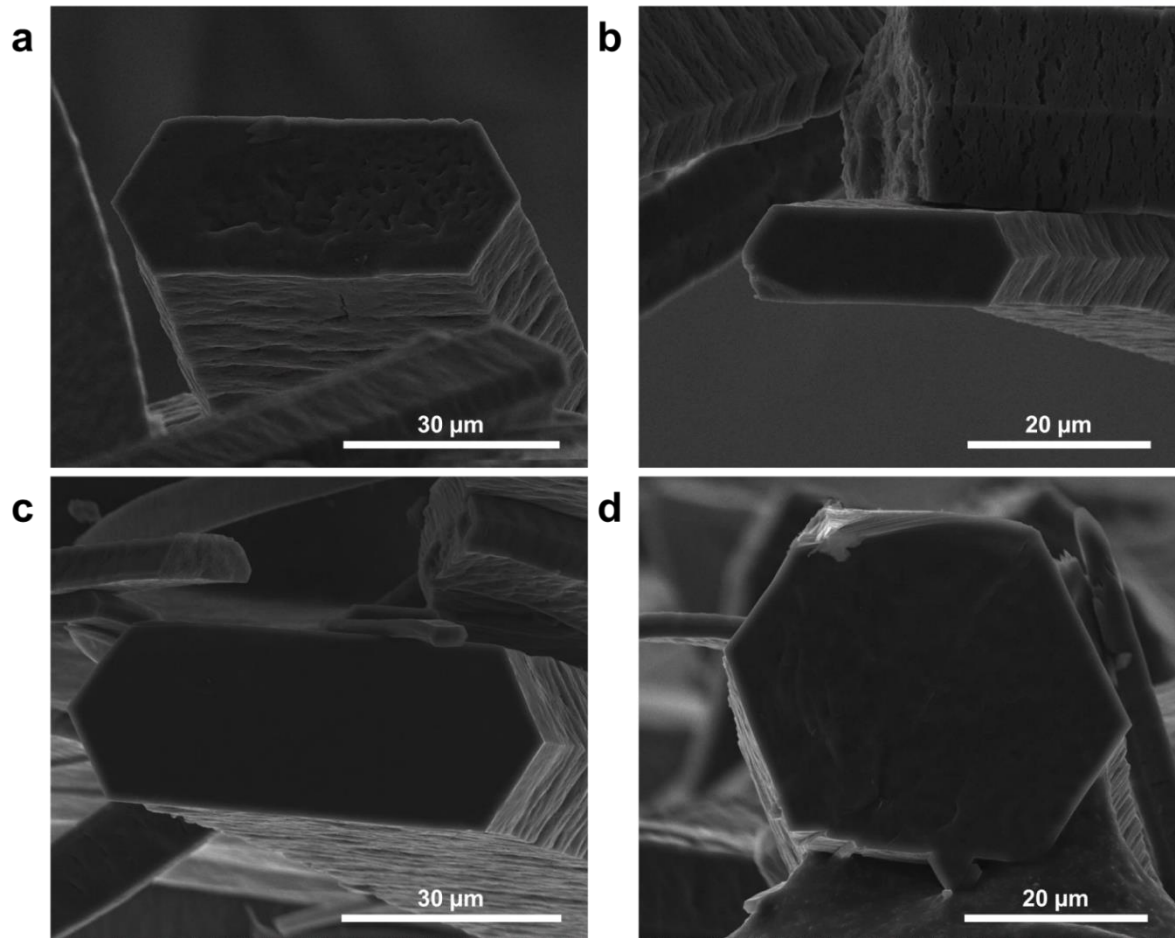


Figure 3.9. SEM images of the C₃N framework at different magnification showing the stacked layers and the prominent hexagonal rod like morphology is well maintained after annealing at 500 °C.

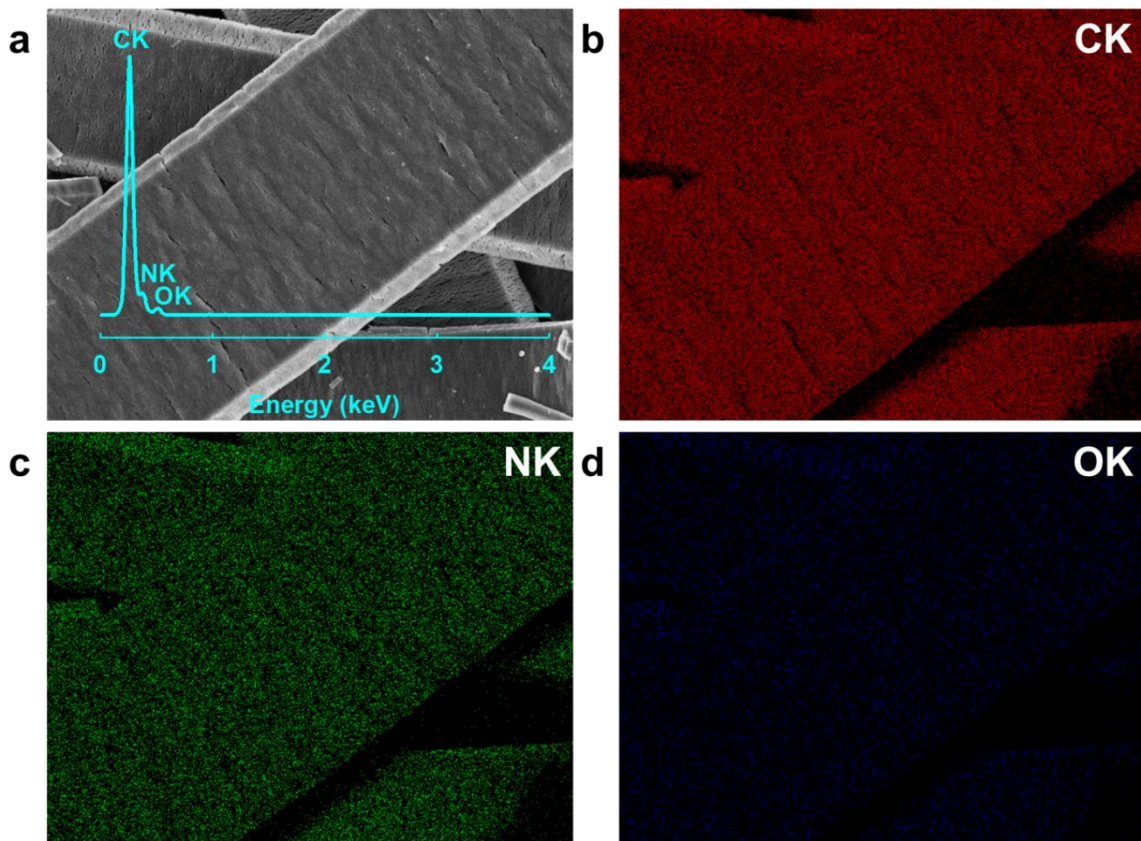


Figure 3.10. SEM energy dispersive X-ray spectroscopy (EDS) showing the elemental composition of the C₃N frame work (C, N and O) from the corresponding SEM image, showing no chloride peak in the EDS spectrum.

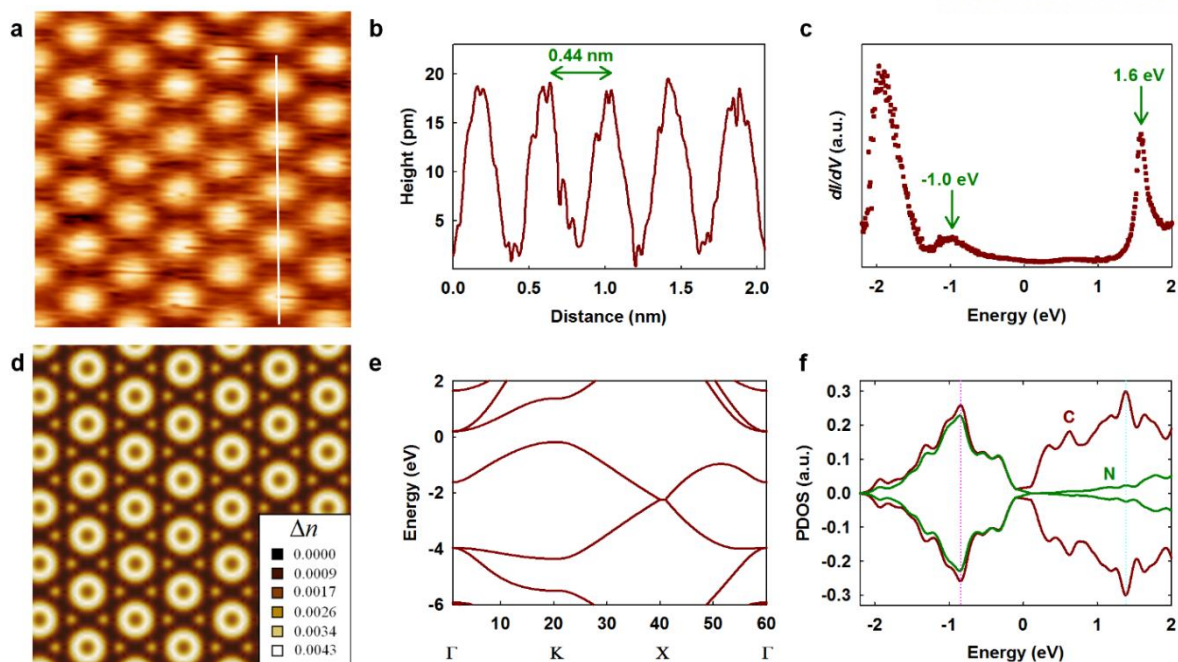


Figure 3.11. STM and theoretical studies of the C_3N structure. (a), STM image of a C_3N crystal ($2.5 \times 2.5 \text{ nm}^2$, $V_s = -1.1 \text{ V}$, $I_t = 1.0 \text{ nA}$); (b), topographic height profile along the white line marked in (a); (c), differential conductance (dI/dV) spectrum of a C_3N crystal; (d), simulated STM image; (e), electronic band structure; (f), PDOS of the carbon (dark-red) and nitrogen (dark-green) atoms.

STM is a probe based equipment that can resolve the electronic and topographic structure of the 2D materials and can exploit individual atoms at specific points in order to construct and characterize well define nanostructures on the clean and smooth substrates. Because of the challenges of the aligning of the specific zone of the substrate with the remote and sensitive STM tip, the most commonly studies samples are *in situ* prepared samples on the particular substrate. The molecular structure of the C_3N was investigated by UHV low-temperature scanning tunneling microscope (Specs. JT-STM) at 77 k. After cleaning the Cu (111) single crystal, HAB molecules were deposited on the substrate *in situ* by thermal evaporation. C_3N reveals the well-ordered triangular structure (**Figure 3.11a**). The dot-to-dot distance is $442 \pm 16 \text{ pm}$ (**Figure 3.11b**), which is very different from the lattice constant of graphene. To examine the electronic structure of C_3N , I performed scanning tunneling spectroscopy (STS) on the material, by employing lock-in detection technique. The HOMO and LUMO are positioned at -0.96 and 1.5 eV , respectively (**Figure 3.11c**) which is in good agreement with the electrochemically determined gap of 2.67 eV (**Figure 3.12**). Electrochemical band gap from the pure HAB molecules was not possible because of the unitability of the HAB in the measuring condition (**Figure 3.12c**) indicating that my C_3N structures are distinctly different from those of self-assembled HAB molecules without carbonization.

First-principles DFT calculations were performed to determine the electronic structure and to analyse the STM image. To produce the calculated STM image, the Kohn-Sham charge density was integrated from the Fermi level to 1.1 eV below the Fermi level. The band structure along the symmetry lines in the Brillouin zone and the projected density of electronic states (PDOS) are shown in **Figures 3.11e and 3.11f**, respectively. The gradient-corrected DFT calculations show that C₃N has a non-zero finite density of states near the Fermi level, in agreement with the STS measurement (**Figure 3.11c**). The valence band maximum and conduction band minimum are both derived from the carbon and nitrogen p_z orbitals. The conduction band minimum states closely resemble the π electronic structures of benzene rings bridged by nitrogen atoms.

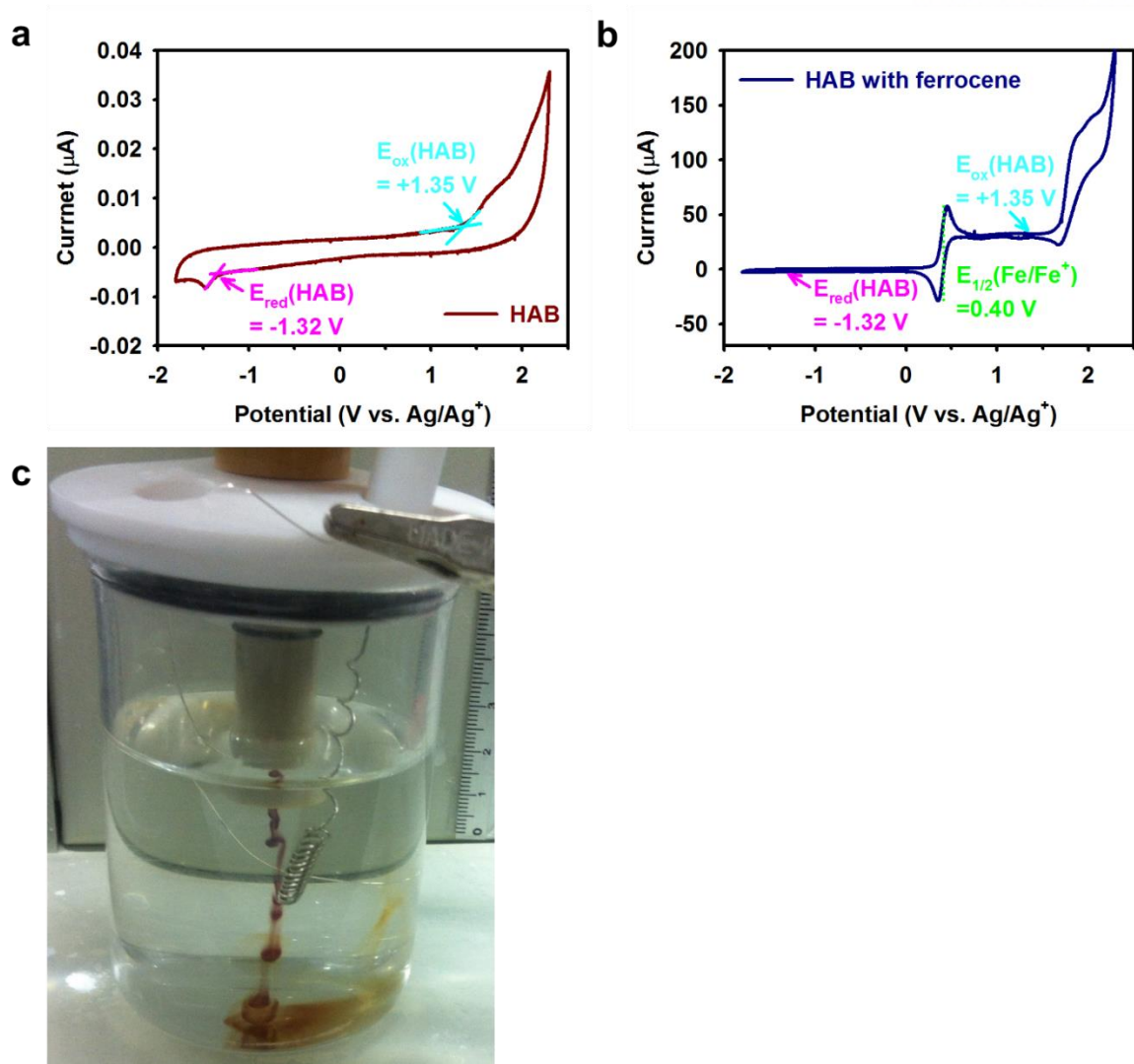


Figure 3.12. Cyclic voltammograms in acetonitrile containing 0.1 M TBAPF₆: (a), C₃N crystal; (b), C₃N crystal with ferrocene; (c), Pure HAB crystals were also tried to measure the band gap by electrochemically, but HAB molecules are unstable in the electrochemical test condition. It decomposes during the process, so it was not possible to determine HOMO-LUMO by electrochemical method.

3.7 Conclusions

In summary, I have shown, a new class of carbon 2D material composed of alternating carbon and nitrogen atoms, has been produced by simple procedure from the organic single crystal, supposed to be the most promising organic 2D material so far after graphene. Molecular level study was also done by STM on the sample fabricated on the substrate. New materials have always been decisive factor in the development of new technologies. It is now technologically feasible to produce new carbon-based 2D material by a simple procedure, 2D C₃N is structural analogue of graphene; hence, I expect unprecedented potential for the applications in next generation electronics, energy storage, nanomedicine, engineering and biology as a novel biocompatible material.

3.8 References

- (1) Hirsch, A. The era of carbon allotropes. *Nat. Mater.* **2010**, *9*, 868.
- (2) Jariwala, D.; Sangwan, V. K.; Lauhon, L. J.; Marks, T. J.; Hersam, M. C. Carbon nanomaterials for electronics, optoelectronics, photovoltaics, and sensing. *Chem. Soc. Rev.* **2013**, *42*, 2824.
- (3) Novoselov, K. S.; Geim, A. K.; Morozov, S. V.; Jiang, D.; Zhang, Y.; Dubonos, S. V.; Grigorieva, I. V.; Firsov, A. A. Electric Field Effect in Atomically Thin Carbon Films. *Science* **2004**, *306*, 666.
- (4) Geim, A. K.; Novoselov, K. S. The rise of graphene. *Nat. Mater.* **2007**, *6*, 183.
- (5) Mayorov, A. S.; Gorbachev, R. V.; Morozov, S. V.; Britnell, L.; Jalil, R.; Ponomarenko, L. A.; Blake, P.; Novoselov, K. S.; Watanabe, K.; Taniguchi, T.; Geim, A. K. Micrometer-Scale Ballistic Transport in Encapsulated Graphene at Room Temperature. *Nano Lett.* **2011**, *11*, 2396.
- (6) Lee, C.; Wei, X.; Kysar, J. W.; Hone, J. Measurement of the Elastic Properties and Intrinsic Strength of Monolayer Graphene. *Science* **2008**, *321*, 385.
- (7) Balandin, A. A. Thermal properties of graphene and nanostructured carbon materials. *Nat. Mater.* **2011**, *10*, 569.
- (8) Bae, S.; Kim, H.; Lee, Y.; Xu, X.; Park, J.-S.; Zheng, Y.; Balakrishnan, J.; Lei, T.; Ri Kim, H.; Song, Y. I.; Kim, Y.-J.; Kim, K. S.; Ozyilmaz, B.; Ahn, J.-H.; Hong, B. H.; Iijima, S. Roll-to-roll production of 30-inch graphene films for transparent electrodes. *Nat. Nanotechnol.* **2010**, *5*, 574.
- (9) Wee Shing, K.; Choon How, G.; Wee Kee, P.; Akimov, Y. A.; Ping, B. The Potential of Graphene as an ITO Replacement in Organic Solar Cells: An Optical Perspective. *Selected Topics in Quantum Electronics, IEEE Journal of* **2014**, *20*, 4000107.
- (10) Dvorak, M.; Oswald, W.; Wu, Z. Bandgap Opening by Patterning Graphene. *Sci. Rep.* **2013**, *3*.

- (11) Lu, G.; Yu, K.; Wen, Z.; Chen, J. Semiconducting graphene: converting graphene from semimetal to semiconductor. *Nanoscale* **2013**, *5*, 1353.
- (12) Xu, M.; Liang, T.; Shi, M.; Chen, H. Graphene-Like Two-Dimensional Materials. *Chem. Rev.* **2013**, *113*, 3766.
- (13) Kissel, P.; Erni, R.; Schweizer, W. B.; Rossell, M. D.; King, B. T.; Bauer, T.; Götzinger, S.; Schlüter, A. D.; Sakamoto, J. A two-dimensional polymer prepared by organic synthesis. *Nat. Chem.* **2012**, *4*, 287.
- (14) Colson, J. W.; Dichtel, W. R. Rationally synthesized two-dimensional polymers. *Nat. Chem.* **2013**, *5*, 453.
- (15) Radisavljevic B.; Radenovic A.; Brivio J.; Giacometti V.; Kis A. Single-layer MoS₂ transistors. *Nat. Nanotechnol.* **2011**, *6*, 147.
- (16) Auwärter, W.; Kreuz, T. J.; Greber, T.; Osterwalder, J. XPD and STM investigation of hexagonal boron nitride on Ni(111). *Surf. Sci.* **1999**, *429*, 229.
- (17) Ma, R.; Sasaki, T. Nanosheets of Oxides and Hydroxides: Ultimate 2D Charge-Bearing Functional Crystallites. *Adv. Mater.* **2010**, *22*, 5082.
- (18) Sakamoto, J.; van Heijst, J.; Lukin, O.; Schlüter, A. D. Two-Dimensional Polymers: Just a Dream of Synthetic Chemists? *Angew. Chem. Int. Ed.* **2009**, *48*, 1030.
- (19) Butler, S. Z.; Hollen, S. M.; Cao, L.; Cui, Y.; Gupta, J. A.; Gutiérrez, H. R.; Heinz, T. F.; Hong, S. S.; Huang, J.; Ismach, A. F.; Johnston-Halperin, E.; Kuno, M.; Plashnitsa, V. V.; Robinson, R. D.; Ruoff, R. S.; Salahuddin, S.; Shan, J.; Shi, L.; Spencer, M. G.; Terrones, M.; Windl, W.; Goldberger, J. E. Progress, Challenges, and Opportunities in Two-Dimensional Materials Beyond Graphene. *ACS Nano* **2013**, *7*, 2898.
- (20) Mahmood, J.; Kim, D.; Jeon, I.-Y.; Lah, M. S.; Baek, J.-B. Scalable Synthesis of Pure and Stable Hexaaminobenzene Trihydrochloride. *Synlett* **2013**, *24*, 246.
- (21) Langer, J. J.; Golczak, S. Highly carbonized polyaniline micro- and nanotubes. *Polym. Degrad. Stab.* **2007**, *92*, 330.
- (22) Trchová M.; Konyushenko, E. N.; Stejskal, J.; Kovářová, J.; Čirić-Marjanović, G. The conversion of polyaniline nanotubes to nitrogen-containing carbon nanotubes and their comparison with multi-walled carbon nanotubes. *Polym. Degrad. Stab.* **2009**, *94*, 929.

- (23) Trchová M.; Matějka, P.; Brodinová, J.; Kalendová, A.; Prokeš, J.; Stejskal, J. Structural and conductivity changes during the pyrolysis of polyaniline base. *Polym. Degrad. Stab.* **2006**, *91*, 114.
- (24) Yang, W. P.; Costa, D.; Marcus, P. Resistance to Pitting and Chemical Composition of Passive Films of a Fe-17%Cr Alloy in Chloride-Containing Acid Solution. *J. Electrochem. Soc.* **1994**, *141*, 2669.
- (25) Lim, A. S.; Atrens, A. ESCA studies of nitrogen-containing stainless steels. *Appl. Phys. A* **1990**, *51*, 411.

IV. Fe-Cocooned C₂N-*h*2D Structures as Efficient Oxygen Reduction Catalysts

4.1 Abstract

Heteroatom-doped carbon-based nanostructured materials have demonstrated a promising oxygen reduction activity in alkaline media but not in acidic media. Hitherto, there are no electrochemically active carbon-based materials in both media with appreciable stability. Here, I describe the design, synthesis and evaluation of the novel type of the non-precious iron (Fe)-based electrocatalyst derived from nitrogenated (C₂N empirical formula unit of basal area) holey two-dimensional structure (C₂N-*h*2D) for the oxygen reduction reaction (ORR). The C₂N-*h*2D is select as a nitrogen abundant carbon framework, which has six nitrogen atoms facing center of uniformly distributed holes, providing high density of coordination sites to cocoon the Fe particles. Fe coordinated C₂N-*h*2D framework (Fe@C₂N-*h*2D) exhibits a high oxygen reduction activity both in acid and alkaline media with very good cycle stability and tolerance against carbon monoxide/methanol poisoning.

4.2 Introduction

Electrochemical catalyst is essential for the clean and sustainable energy technologies such as fuel cells¹ and metal-air cells.² Platinum (Pt) -based materials have long been regarded as the most efficient catalysts for oxygen reduction reaction (ORR) in fuel cells.^{3,4} However, their sensitivity to fuel crossover and carbon monoxide (CO) poisoning, limited reserves and very high cost hampers their commercialization on large-scale in air-breathing electrodes.⁵ Comprehensive efforts have been explored on non-precious-metal catalysts to replace the precious Pt-based catalysts in the fuel cells.^{6,7} In this connection, non-precious metal coordinated heteroatom-doped carbon-based materials have garnered huge interest for ORR.⁸⁻¹¹ For example, cobalt phthalocyanine was initially described to show substantial catalytic activity toward ORR¹² and this initiative discovery inspired extensive studies on a variety of non-precious metal-based materials as a potential alternatives to Pt-based materials, including transition metal oxides,¹³ organometallic complexes,¹⁴ chalcogenides¹⁵ and bio-inspired compounds.¹⁶ However, these reported materials are too costly and/or lack stability in a fuel cell system. More importantly, their catalytic activity for ORR is mediocre compared to the Pt-based commercial catalysts. Recent developments in ORR indicated that nitrogen-doped carbon nanomaterials could work as an efficient catalysts for ORR in alkaline fuel cells.^{17,18} However, these heteroatom-doped carbon-based materials are rival to Pt-based catalysts only in alkaline medium, which hinders their utilization in proton exchange membrane fuel cells (PEMFC), which operate in acidic media and microbial fuel cells (MFC) running in neutral solutions.

An alternative route is to incorporate non-precious iron (Fe) into the carbon nanostructures. Such hybrid materials show good catalytic activity near to Pt-based catalysts.^{1,11,19} In a recent approach has described to produce bimetallic system for ORR catalysts as a potential replacement for Pt-based catalysts.²⁰ It is usually perceived that interactions between nitrogen-doped carbon nanostructure and transition metals play a pivotal role to produce useful active sites for ORR. Nevertheless, Fe-based catalysts are always suffering from instability. Therefore, the most important challenge is to improve electrochemical stability as potential alternatives to Pt-based catalysts.

4.3 Materials

All the solvents, chemicals and reagents were purchased from Aldrich Chemical Inc., unless otherwise stated. Solvents were degassed with nitrogen purging before use. All the reactions were performed under nitrogen atmosphere using oven dried glassware. 1,2,3,4,5,6-hexaaminobenzene was synthesized according to literature procedure.²¹

4.4 Instrumentation

Thermogravimetric analysis (TGA) was conducted in air and nitrogen atmosphere at a heating rate of 10 °C/min using a Thermogravimetric Analyzer Q200 TA Instrument, USA. The surface area was calculated by nitrogen adsorption-desorption isotherms using the Brunauer-Emmett-Teller (BET) method on Micromeritics ASAP 2504N. Scanning electron microscope (SEM) images were taken on Field Emission Scanning Electron Microscope Nanonova 230 FEI, USA. X-ray photoelectron spectroscopy (XPS) was performed on X-ray Photoelectron Spectroscopy Thermo Fisher K-alpha (UK). X-ray diffraction (XRD) studies were taken on High Power X-Ray Diffractometer D/MAZX 2500V/PC (Cu-K α radiation, 35 kV, 20 mA, $\lambda = 1.5418 \text{ \AA}$) Rigaku, Japan. High resolution transmission electron microscopy (TEM) was performed by using JEM-2100F (JEOL, Japan) under an operating voltage of 200 keV. The samples for TEM were prepared by drop casting NMP dispersion on Quantifoil holey carbon TEM grid and dried in oven at 80 °C. XPS were recorded on a Thermo Fisher K-alpha spectrometer. Elemental analysis was conducted with Thermo scientific Flash 2000.

4.5 Synthesis of the iron containing holey 2D crystal (Fe@C₂N-h2D)

FeCl₃ (1.168g) was first dissolved in NMP (35 mL) and placed on the ice bath in 3-necked round bottom flask and then added hexaketocyclohexane octahydrate (1.125 g, 3.603 mmol) followed by addition of Hexaaminobenzene trihydrochloride (1.00g, 3.603 mmol) under the nitrogen atmosphere and the reaction flask was slowly warm up to room temperature for 2 hours. The ice bath was replaced with oil bath and heated to 175 °C and refluxed for 8 hours. After completion of the reaction the reaction

mixture was cooled to 80 °C and added NaBH₄ (5g) and refluxed again for 3 hours. Then, the flask was cooled slowly to room temperature and poured some water into it. The precipitated black solid product was collected by suction filtration using PTFE (0.5 μm) membrane. The resultant dark black solid was further Soxhlet extracted with methanol and water, respectively, and oven dried at 75 °C under reduced pressure. After drying the product was annealed at 500 °C for 2 hours under argon atmosphere.

4.6 Cyclic voltammogram

Cyclic voltammetry (CV) measurements were conducted using a computer controlled potentiostat (CHI 760 C, CH Instrument) in a standard three-electrode cell. Samples/glassy carbon (GC) electrodes were utilized as the working electrode, a platinum wire as the counter electrode, and an Ag/AgCl (3 M KCl filled) electrode as the reference electrode. Rotating disk electrode (RDE) experiments were measured on a MSR-X electrode rotator (Pine Instrument) and the CHI 760 C potentiostat. For all CV measurements, an aqueous solution of KOH (1.0 M) was used as the electrolyte. N₂ or O₂ was used to purge the solution to achieve oxygen-free or oxygen-saturated electrolyte solution. Procedures for the pretreatment and modification of glassy carbon (GC) electrode are described as follows: the working electrode was polished with alumina slurry to achieve a mirror-like surface and then washed with DI water and dried in air. Samples (1 mg) were dissolved in 1 mL solvent mixture of NMP by slight sonication. The sample suspensions (5 μl) were pipetted on the glassy carbon (GC) electrode surface, followed by drying at room temperature under vacuum.

4.7 Results and Discussion

Herein, I would like to report a new class of catalyst system, which consists of Fe-cocooned nitrogenated holey two-dimensional crystals (Fe@C₂N-*h*2D). The Fe@C₂N-*h*2D was synthesized by the polycondensation between hexaketocyclohexane (HKH) and hexaaminobenzene (HAB) trichloride in the presence of iron chloride (FeCl₃).²² The HKH and HAB are used for the formation of C₂N-*h*2D (empirical formula, C₂N; holey two-dimensional, *h*2D) structure and FeCl₃ is used as a Fe precursor. The C₂N-*h*2D structures have uniform holes and each hole contains six nitrogen atoms for Fe encapsulation. The resultant Fe@C₂N-*h*2D displays unusual catalytic activity with excellent stability in both acidic and alkaline media. The results indicated that the electrocatalytic performance of Fe@C₂N-*h*2D is superb to the commercial Pt/C.

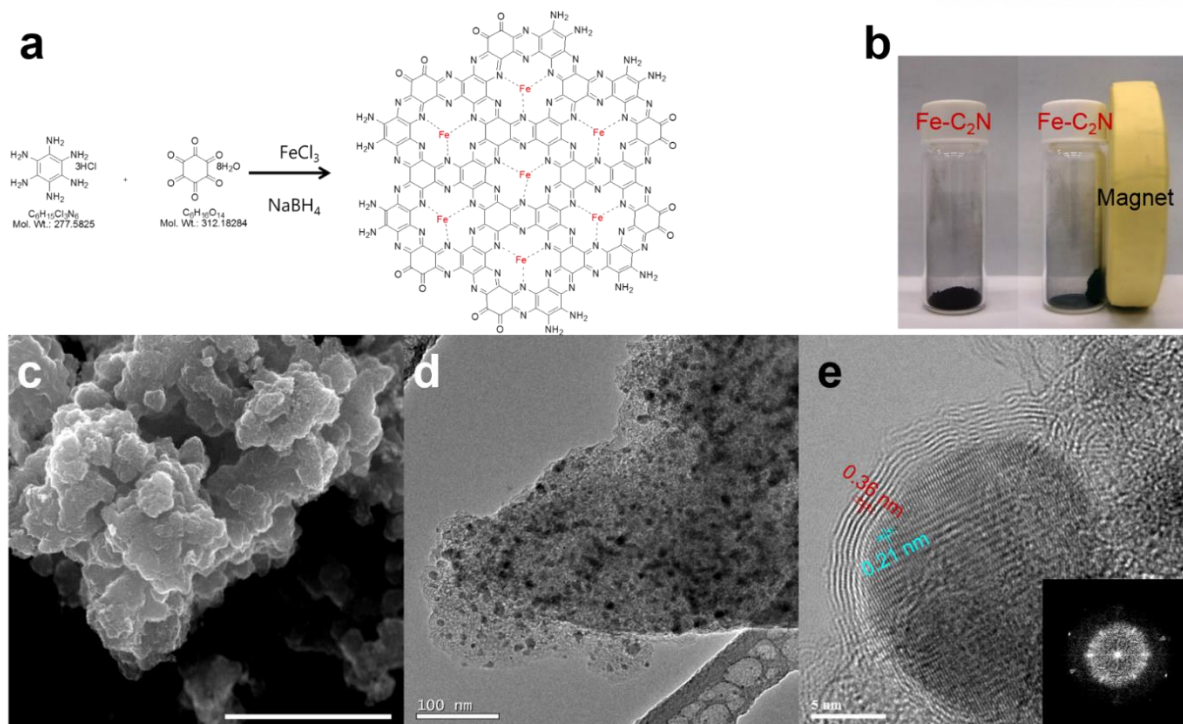


Figure 4.1. (a) Schematic presentation of the Fe@C₂N-*h*2D synthesis; (b) behavior of the Fe@C₂N-*h*2D in the magnetic field. Fe@C₂N-*h*2D in vial without magnetic field (left); Fe@C₂N-*h*2D in vial with magnetic field (right), showing attraction of black Fe@C₂N-*h*2D particles toward magnet and the particles are accumulated on the side of the glass wall (The image taken from the video clip in Supporting Information); (c) SEM image of Fe@C₂N-*h*2D; (d) low-magnification of HR-TEM image; (e) high-magnification of HR-TEM image, showing the encapsulated Fe nanoparticles. Inset is selected-area electron diffraction (SAED) pattern.

As schematically presented in Figure 4.1a, Fe@C₂N-*h*2D was *in-situ* synthesized by the reaction between HKH and HAB in the presence of iron(III) chloride. The resultant Fe@C₂N-*h*2D is black colored and displays strong magnetic response (**Figure 4.1b**), indicating the presence of Fe nanoparticles. Field-emission scanning electron microscopy (FE-SEM) was used to examine the surface morphology of the Fe@C₂N-*h*2D, showing unique granular morphology (**Figures 4.1c and 4.2**). Energy-dispersive spectroscopy (EDS) combined with SEM (SEM-EDS) was used to confirm the elemental composition in the Fe@C₂N-*h*2D (**Figure 4.2**). Uniform distribution of Fe nanoparticles in the C₂N-*h*2D framework were detected by element mappings in the SEM-EDS analysis. EDS (**Figure 4.2**) and XPS (**Figure 4.3**) survey spectra of the Fe@C₂N-*h*2D revealed the presence of C, N, O and Fe and the detailed data are summarized in Table 4.1. The important peaks identified in the XPS survey spectrum correspond to different chemical states of carbon, nitrogen, oxygen and iron atoms,

respectively. High resolution XPS spectra for C1s, N1s, O1s and Fe are shown in the figure. C1s can be resolved into three major peaks at 284.4 eV (C-C sp²), 285.4 eV (C-N sp²) and 288.09 eV for carbon bonded to heteroatom. There are two peaks of element N1s in figure. The peak at 398.2 eV corresponds to the binding energy of the Fe₃-N bond and the peak at 399.6 corresponds to the pyrazine like nitrogen in the C₂N framework. O1s is resolved into three peaks 530.05 eV, 531.4 eV and 532.7 eV respectively for physically adsorbed oxygen and C=O bonds at the edges. To further investigate the structure of the Fe@C₂N-h2D, the high-resolution transmission electron microscopy (HR-TEM) was conducted. As illustrated in Figure 4.1d, HR-TEM the sample is consist of Fe nanoparticles, which have an average diameter of approximately 10-30 nm. At high magnification, the Fe nanoparticle is a distinctive encapsulated with a C₂N-h2D framework. The number of coated C₂N-h2D layers varies from 2 to 6. The selected-area electron diffraction (SAED) pattern of the Fe@C₂N-h2D can be assignable to diffraction planes of the crystalline structure of the nanoparticles coated C₂N-h2D layers.

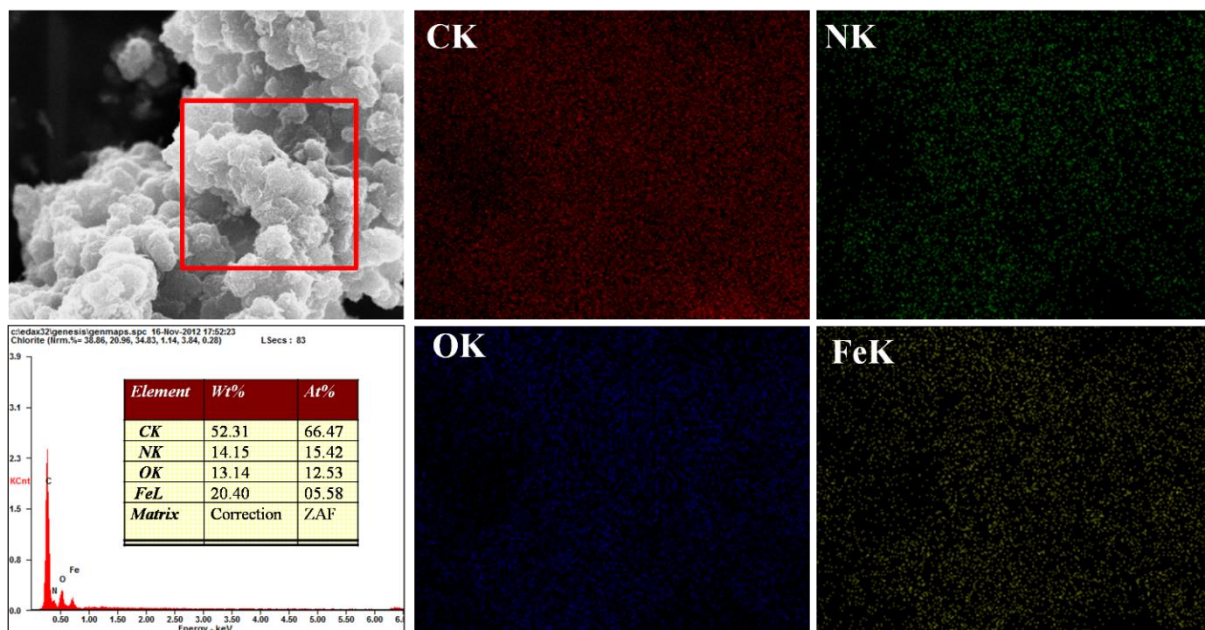


Figure 4.2. Fe@C₂N-h2D energy dispersive X-ray spectroscopy (EDS) spectrum showing the elemental mapping and composing (C, N, O and Fe) from the SEM image.

Detailed structural information of the Fe nanoparticles was further investigated, indicating that C₂N-*h*2D layers can clearly determine around the Fe nanoparticles with interlayer spacing of 0.35 nm (**Figure 4.5b**), which is matching with the XRD results (**Figure 4.2b**). The nanoparticles have well-defined crystalline lattice spacing of 0.21 nm can be observed in the core of the nanoparticles, which is the related to the diffraction peak of the Fe₃C (**Figure 4.5d**). These results ascertain the complete encapsulation of metallic Fe nanoparticles inside the C₂N-*h*2D layers, which are expect to protect Fe nanoparticles from oxidization even after prolonged exposure to air. Figure 4.6 reveals the nitrogen adsorption-desorption isotherms of the Fe@C₂N-*h*2D. The Brunauer-Emmett-Teller (BET) specific surface area is approximately 84.02 m² g⁻¹. The nitrogen adsorption-desorption isotherms exhibit a hysteresis loop of type H4 (IUPAC), indicating the presence of slit like pores between the layers (**Figure 4.6**). The catalyst shows total pore volume of about 0.1554 cm³ g⁻¹ and having mesopores of average pore diameter 7.39 nm.

Table 4.1. Elemental composition from different techniques

Technique	C%	Fe%	N%	O%	Total
XPS at.%	66.25	2.93	13.35	17.47	100
EDS (SEM) wt.%	52.31	20.4	14.15	13.14	100
EDS (SEM) at.%	66.47	5.58	15.42	12.53	100

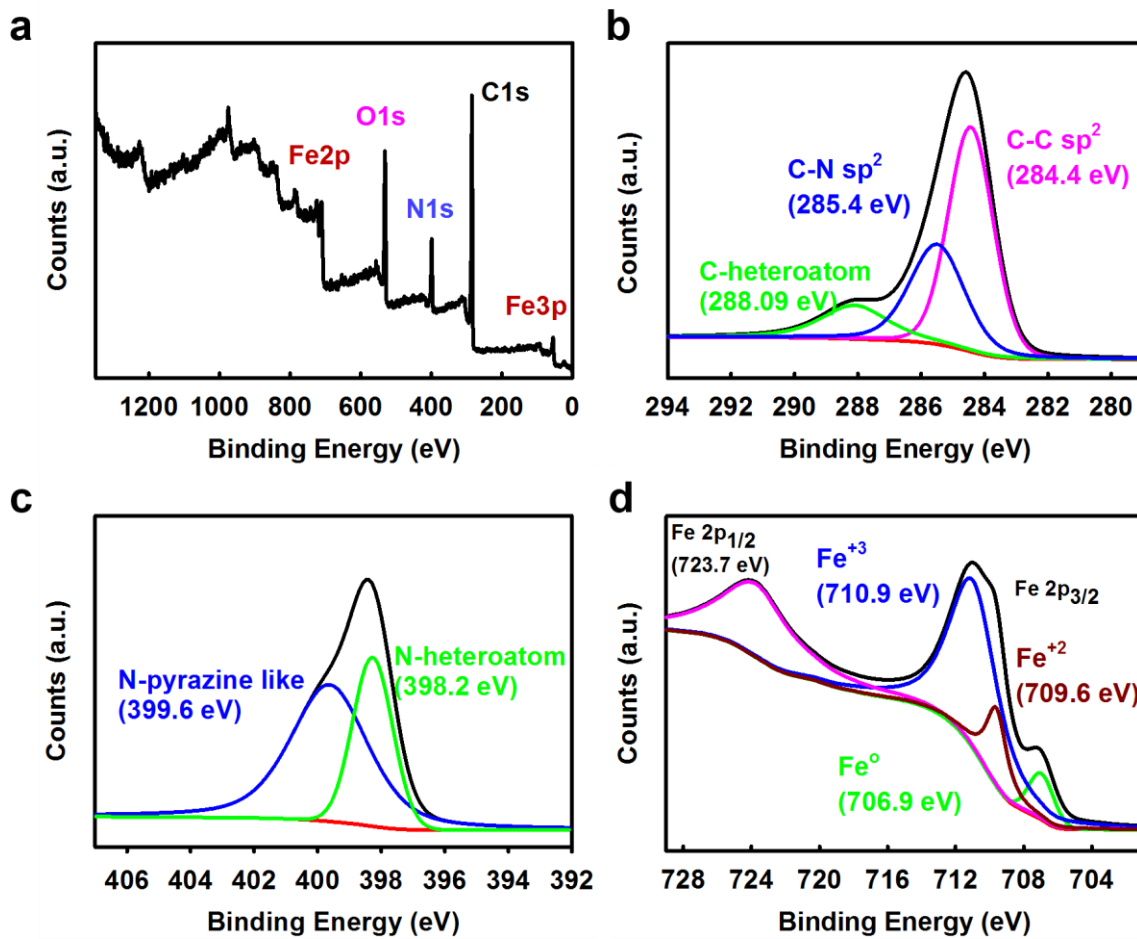


Figure 4.3. (a) XPS survey spectrum showing C1s, Fe 2p, N1s and O1s. Deconvoluted XPS spectra of Fe@C₂N-*h*2D (b) C 1s; (c) N 1s; (d) Fe 2p.

Figure 4.4b presents the X-ray diffraction (XRD) patterns of the prepared Fe@C₂N-*h*2D. The diffraction peak at 25.5° (2θ) relates to the (002) planes of C₂N-*h*2D structure, while the peak at 43.7° and 45.01° are characteristic of Fe-nitride.²³ The peak appearing at 44.7° and 65.9° are related to Fe-carbide bond formation.²⁴ The rest of the peaks are characteristic of the crystalline planes of the Fe carbide and Fe₃N species (JCPDS, No.87-0722, 89-2867, 86-0232, 73-2102). Therefore, the crystalline XRD results validate that the hybrid material comprised of C₂N-*h*2D structure formed Fe-carbide and Fe-nitride species. The result is clear indication of strong interaction between the Fe and C₂N-*h*2D, as indicated by TEM analysis (**Figures 4.1d and 4.1e**).

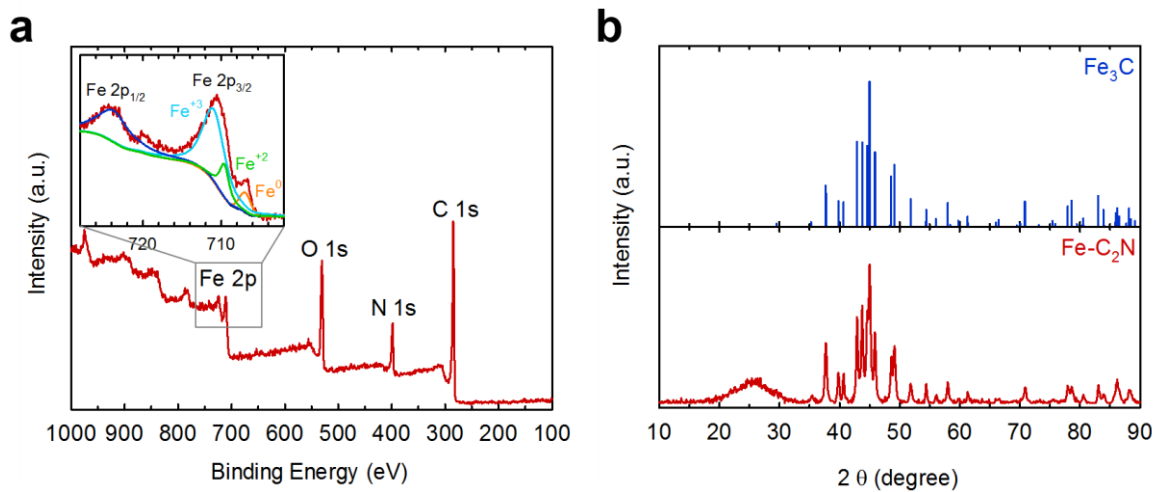


Figure 4.4. XPS and XRD of the Fe@C₂N-*h*2D samples: (a) Survey XPS spectrum with the inset Fe deconvoluted spectrum; (b) Powder XRD from the Fe@C₂N-*h*2D in comparison with the simulated Fe₃C XRD.

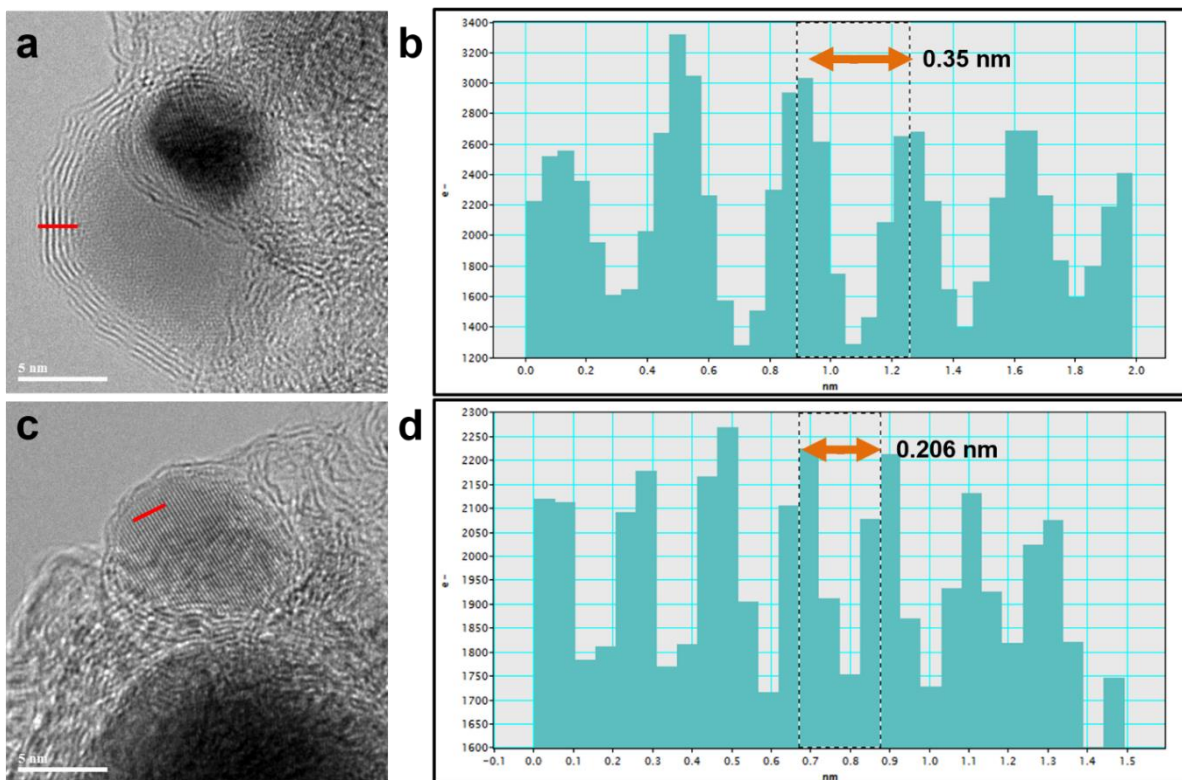


Figure 4.5. (a,c) HR-TEM images of as-prepared Fe@C₂N-*h*2D; (b) inter layer distance from the red marked line; (d) lattice distance from the Fe nanoparticles from the marked distance.

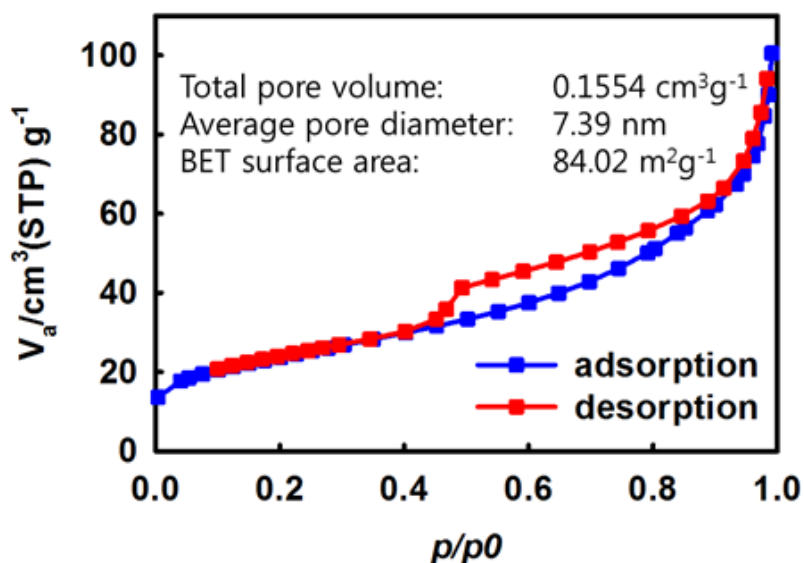


Figure 4.6. Nitrogen adsorption and desorption isotherm for the Fe@C₂N-h₂D. The Brunauer-Emmett-Teller (BET) specific surface area is approximately 84.02 m²g⁻¹ which is apparently low. The nitrogen adsorption-desorption isotherms exhibit a hysteresis loop of type H4 indicating the presence of slit like pores between the layers.

Given the well-defined structural identification of Fe@C₂N-h₂D, its ORR activity was evaluated using cyclic voltammetry (CV) in both 1 M aq. KOH and 1 M aq. H₂SO₄ solutions. The ORR effectiveness of commercial 20 wt.% Pt/C (Vulcan XC-72R, E-TEK) was carried out under the same environment for comparison. The same mass of each material was loaded onto a glassy electrode (20 μg cm⁻²). **Figures 4.7a and 4.7b** show CVs of the Fe@C₂N-h₂D electrode in the N₂ and O₂ saturated 1 M aq. KOH solution. Fe@C₂N-h₂D electrode showed well-defined reduction peak in O₂-saturated 1 M aq. KOH solution, which can be attributed to electrocatalytic reduction of oxygen on the electrodes. The electrocatalytic activity can be disclosed by the capacitance from the voltammogram. Surprisingly, the capacitance of Fe@C₂N-h₂D was more than twice of the commercial Pt/C catalyst in both acidic and basic conditions (**Figures 4.8 and 4.9**).

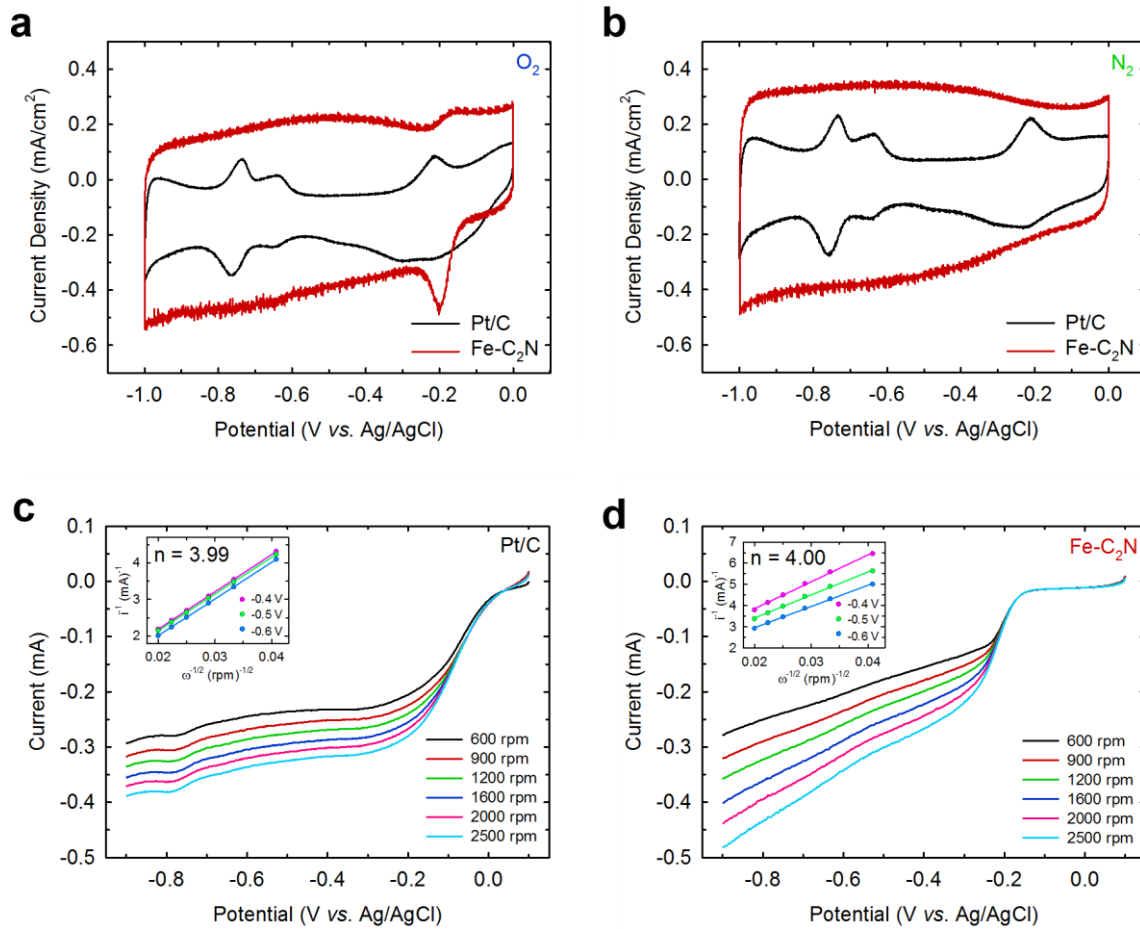


Figure 4.7. Cyclic voltammograms of Pt/C and Fe@C₂N-h₂D in 1 M aq. KOH solution: (a) in oxygen-saturated and (b) in nitrogen-saturated conditions. Polarization curves on a glassy carbon RDE voltammograms for Pt/C and Fe@C₂N-h₂D in O₂-saturated 0.1 M aq KOH solution with a scan rate of 0.01 V s⁻¹ at different rotating rates of 600, 900, 1200, 1600, 2000, and 2500 rpm: (c) the Pt/C; (d) Fe@C₂N-h₂D. Koutecky-Levich plots for the Fe@C₂N-h₂D (inset in c) and Pt/C (inset in d) electrodes at -0.6 V.

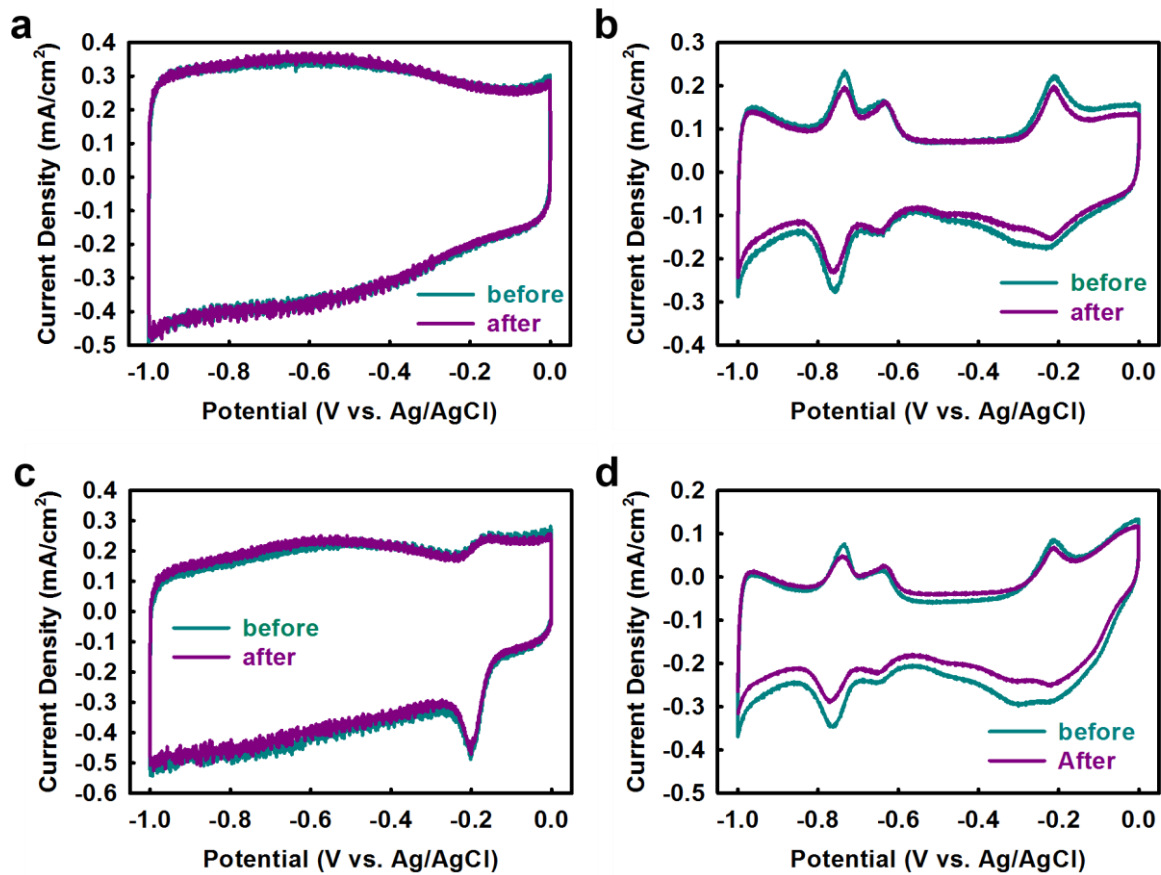


Figure 4.8. Cyclic stability of the samples before and after 200 cycles in 1 M aq. KOH solution. (a) Fe@C₂N-h₂D in nitrogen condition (b) Pt/C in nitrogen saturated atmosphere (c) Fe@C₂N-h₂D in oxygen saturated condition (d) Pt/C in oxygen saturated environment.

To understand the principle element in Fe@C₂N-h₂D for unusual ORR behavior, a series of comparative CV experiments were conducted. CVs of the samples were performed on glassy carbon electrode with a scan rate of 100 mV s⁻¹, both in N₂ and O₂ saturated 1 M aq. KOH solution. In oxygen-saturated 1 M aq. KOH solution, the capacitance of the Fe@C₂N-h₂D and Pt/C are 200 and 85 F g⁻¹, respectively. In nitrogen-saturated 1 M aq. KOH solution, the capacitance (220 F/g) of Fe@C₂N-h₂D is also much higher than that (93 F/g) of Pt/C. In oxygen-saturated 1 M aq. H₂SO₄ solution, the capacitance of the Fe@ C₂N-h₂D is 198 F/g and that of Pt/C is 80 F/g. In nitrogen-saturated 1 M aq. H₂SO₄ solution, the capacitances are 165 and 77 F g⁻¹, respectively, for Fe@C₂N-h₂D and Pt/C (**Figures 4.8 and 4.9**).

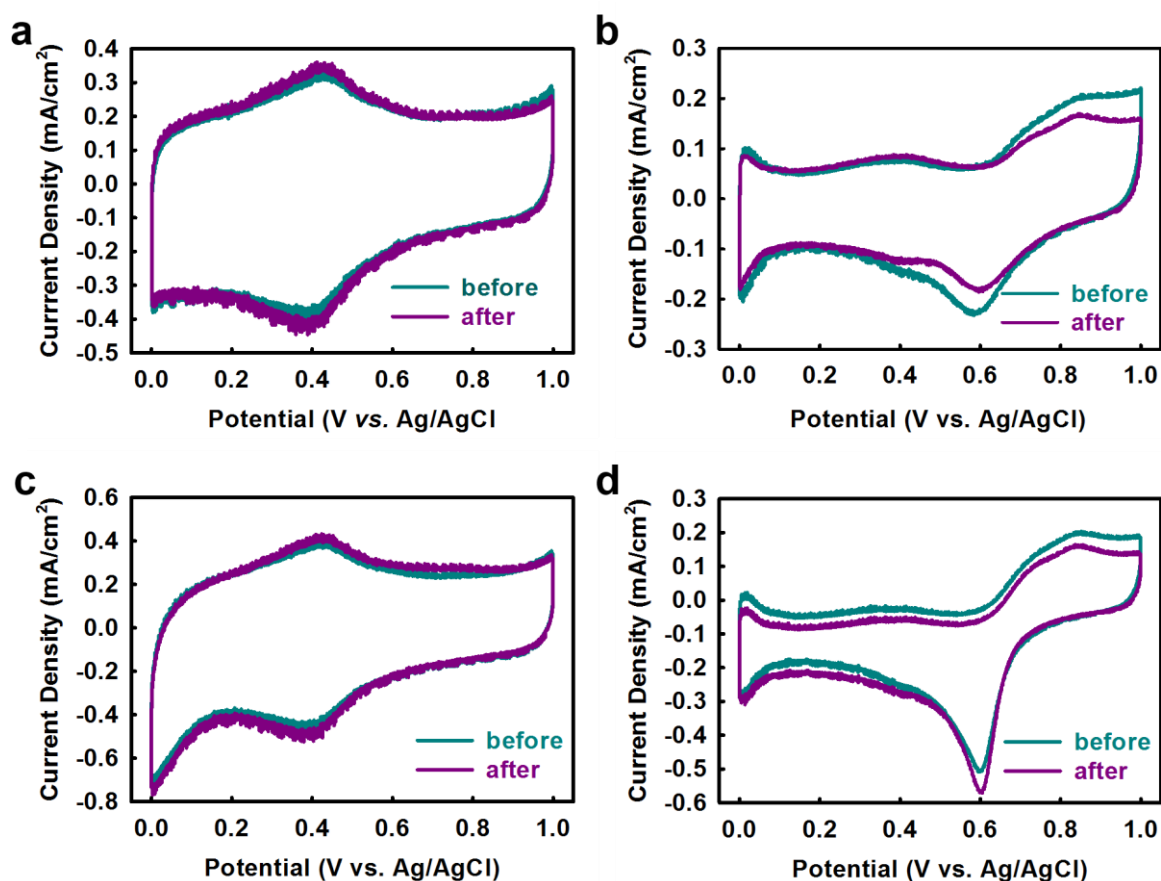


Figure 4.9. Cyclic stability of the samples before and after 200 cycles in 1 M aq. H₂SO₄ solution: (a) Fe@C₂N-h₂D in nitrogen condition (b) Pt/C in nitrogen saturated atmosphere (c) Fe@C₂N-h₂D in oxygen saturated condition (d) Pt/C in oxygen saturated environment.

Cycle stability of the samples before and after 10,000 cycles in 1 M aq. KOH and 1 M aq. H₂SO₄ solutions were also performed (**Figures 4.8 and 4.9**). In case of nitrogen saturated 1 M aq. KOH solution, the capacitance retention of Fe@C₂N-h₂D is almost 100%, while Pt/C decreases to 60% after 10,000 cycles. In case of oxygen saturated atmosphere, the capacitance retentions are 98% and 66%, respectively, for Fe@C₂N-h₂D and Pt/C. The capacitance retentions for Fe@C₂N-h₂D in 1 M aq. H₂SO₄ are 103% and 105%, respectively, in nitrogen and oxygen saturated conditions, while those of Pt/C retains the 50% in nitrogen-saturated condition and 62% capacitance in oxygen-saturated condition after 10,000 cycles (**Figure 4.10**). Even after 10,000 cycles, the deterioration of Pt occurred on Pt/C catalyst (**Figure 4.11**). The reason of decreased activity could be associated to the migration/aggregation of the Pt nanoparticles caused by continuous potential cycling and causing the subsequent loss of specific catalytic activity.⁵

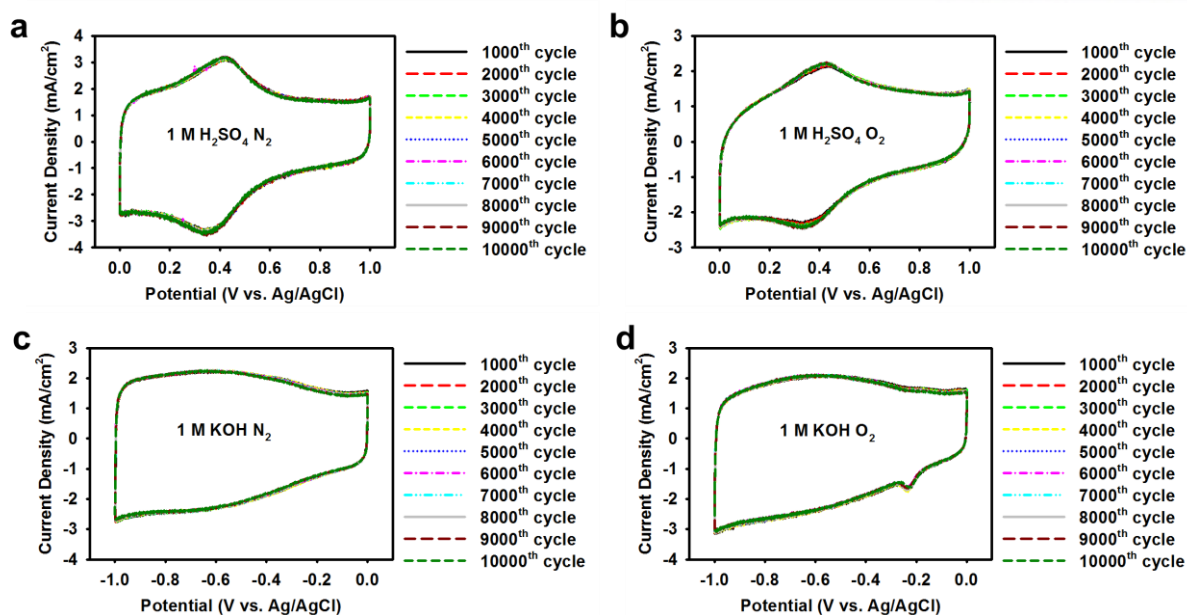


Figure 4.10. Stability test of the Fe@C₂N-h₂D in H₂SO₄ and KOH both in oxygen and nitrogen atmosphere after 10,000 cycles.

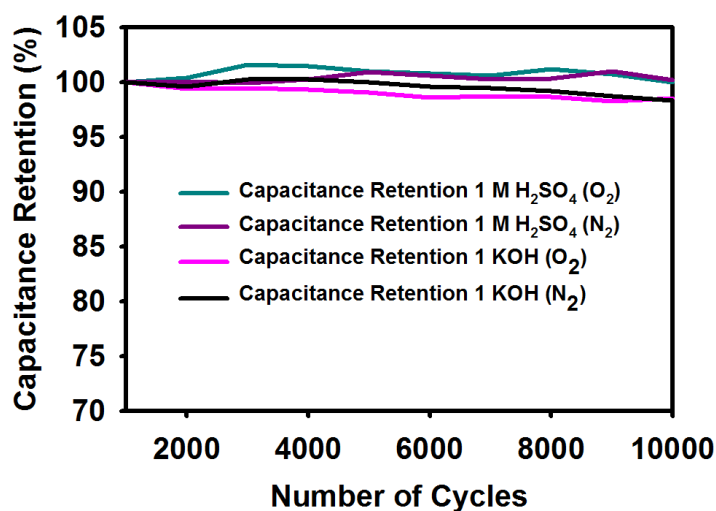


Figure 4.11. Stability of the Fe@C₂N-h₂D material, capacitance retention after 10,000 cycles.

To examine the kinetics of electrochemical catalytic ORR at Fe@C₂N-h₂D and Pt/C electrodes, rotating disk electrode (RDE) voltammograms were further performed. The polarization curves were recorded by scanning the potential from 0.0 to -1.0 V at a scan rate of 10 mV s⁻¹ with different rotation frequency (**Figures 4.7c and 4.7d**). The current exhibits a typical increase with rotation rate owing to the shortened diffusion layer.¹⁷ Analysis of the steady-state diffusion currents through Koutechy-Levich

(K-L) plots indicates a four electron process of the ORR on Fe@C₂N-*h*2D with water as a major product, as is the case for Pt/C catalyst. K-L curves (Insets, **Figures 4.7c and 4.7d**) demonstrate the inverse current density (j^{-1}) as a function of the inverse of the square root of the rotation speed ($\omega^{-1/2}$) at different potential plots. The onset potential is located at about -0.14 V for Fe@C₂N-*h*2D electrode, slightly higher than that of Pt/C electrode (-0.05 V). These K-L curves indicated good linearity with parallelism, suggesting a first order dependence of the O₂ reduction kinetics on the electrodes. From the K-L equation, the number of the electron transferred for ORR at Fe@C₂N-*h*2D and Pt/C electrodes was determined to be about 4.00 and 3.99 respectively, demonstrating the ORR in Fe@C₂N-*h*2D and Pt/C electrodes (Insets, **Figures 4.7c and 4.7d**) predominantly proceeds with an ideal four electron reaction pathway. In addition, the kinetic current of Fe@C₂N-*h*2D was -0.43 mA, which is higher than that of Pt/C catalyst (-0.38 mA). This enhanced kinetic current at the Fe@C₂N-*h*2D electrode symbolizes the improved dynamics for the ORR relative to the Pt/C catalyst.

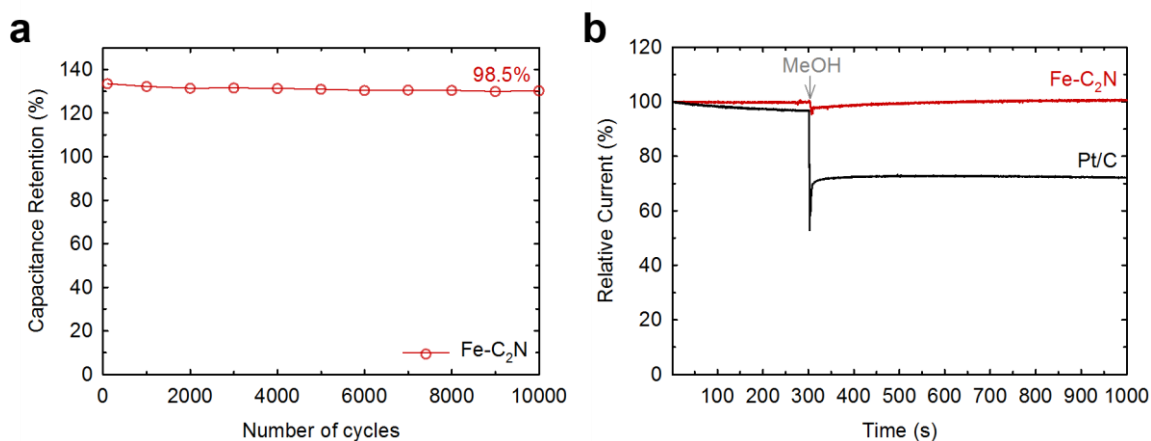


Figure 4.12. Stability and methanol crossover effect of Pt/C and Fe@C₂N-*h*2D in oxygen saturated 0.1 M aq. KOH solution: (a) capacity retention as a function of cycle number of 10,000 cycles; (b) methanol tolerance.

Furthermore, the fuel crossover effect on the ORR activity of Fe@C₂N-*h*2D was evaluated in the presence and absence of methanol. It has a serious influence on the ORR activity of Pt/C, while there is almost no effect for Fe@C₂N-*h*2D (**Figure 4.12b**). These results are indicative for the promising activities of the Fe@C₂N-*h*2D as a stable ORR catalyst in the DMFC.

On the basis of the results, Fe@C₂N-*h*2D surpasses the Pt/C as the cathode catalyst for ORR in fuel cells. The high degree of catalytic properties could be associated to the synergic effects from the core Fe nanoparticles encapsulated by C₂N-*h*2D, which contains uniformly distributed nitrogen atoms and

holes, providing very good interaction between them. In addition to the superb ORR activity and enhanced kinetics of Fe@C₂N-h2D to Pt/C, the synthetic protocol is simple and the process could be easily scale up for mass production. Furthermore, long-term stability is critical for practical use. Hence, the durability of the Fe@C₂N-h2D catalyst was explored by cycling for 10,000 times between 0 and 1 V at a scan rate of 100 mV s⁻¹ in both acidic and alkaline media (Figures 4.12a, 4.9-4.11). There is no obvious change in the current density and/or shift in ORR potential noticed during the experiment, demonstrating the high stability of Fe@C₂N-h2D in both acidic and alkaline media.

Furthermore, the magnetic properties of Fe-encapsulated nanoparticles were recorded by using Superconducting Quantum Interference Device - Vibrating Sample Magnetometer (SQUID-VSM). The Fe-encapsulated sample displays hysteresis loop at 5 K and 300 K (Figure 4.13a). The coercivity and remanence of the sample do not disappear even at 300K, suggesting ferromagnetic ground state. The blocking temperature (T_b) measured at $H = 1000$ Oe was 370 K, which is considerably higher than the typical magnetic nanoparticles (Figure 4.13b). Higher T_b may be associated with robust crystallinity of the sample and/or enhanced surface anisotropy due to the embedded environment. The transition to the superparamagnetism can be observed in zero field-cooled (ZFC) versus field-cooled (FC) magnetization.

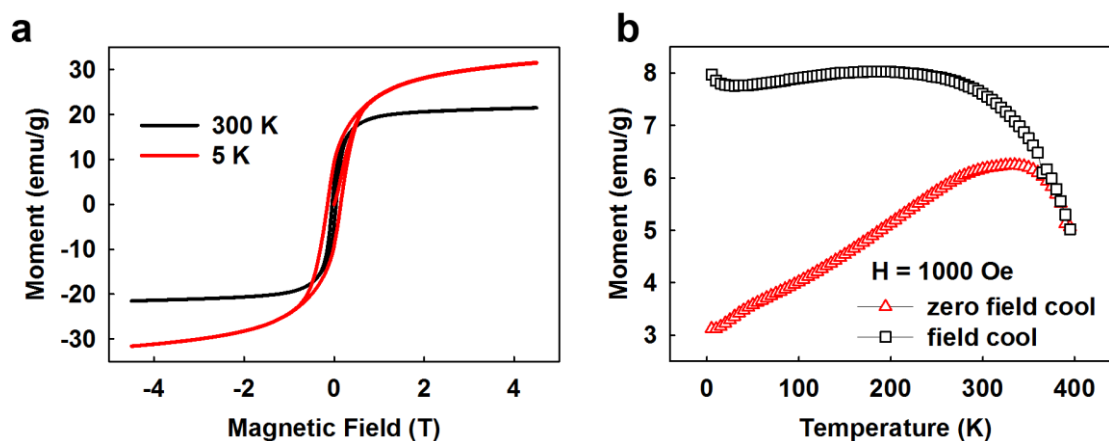


Figure 4.13. (a), Displays hysteresis loop of the sample measured at 5 K and 300K. (b), the blocking temperature (T_b) measured at $H = 1000$ Oe was~ 370 K.

4.8 Conclusions

In summary, I have, for the first time, synthesized Fe-cocooned C₂N-h2D (Fe@C₂N-h2D) structures by a simple but efficient synthetic protocol. The structure of Fe nanoparticle cores encapsulated by C₂N-

*h*2D shells was confirmed by HR-TEM. Compared with Pt/C, Fe@C₂N-*h*2D can considerably reduce the costs, while gaining significantly improved catalytic activity with enhanced stability in both acidic and alkaline media. Hence, Fe@C₂N-*h*2D can offer a potential alternatives to Pt-based cathode materials for fuel cells. The approach described in this work could lead to the development of various non-precious metal-based electrocatalysts on C₂N-*h*2D platform.

4.9 References

- (1) Wen, Z.; Ci, S.; Zhang, F.; Feng, X.; Cui, S.; Mao, S.; Luo, S.; He, Z.; Chen, J. Nitrogen-Enriched Core-Shell Structured Fe/Fe₃C-C Nanorods as Advanced Electrocatalysts for Oxygen Reduction Reaction. *Adv. Mater.* **2012**, *24*, 1399.
- (2) Zhang, G.-Q.; Zhang, X.-G.; Wang, Y.-G. A new air electrode based on carbon nanotubes and Ag-MnO₂ for metal air electrochemical cells. *Carbon* **2004**, *42*, 3097.
- (3) Steele, B. C. H.; Heinzel, A. Materials for fuel-cell technologies. *Nature* **2001**, *414*, 345.
- (4) Lim, B.; Jiang, M.; Camargo, P. H. C.; Cho, E. C.; Tao, J.; Lu, X.; Zhu, Y.; Xia, Y. Pd-Pt Bimetallic Nanodendrites with High Activity for Oxygen Reduction. *Science* **2009**, *324*, 1302.
- (5) Gong, K.; Du, F.; Xia, Z.; Durstock, M.; Dai, L. Nitrogen-Doped Carbon Nanotube Arrays with High Electrocatalytic Activity for Oxygen Reduction. *Science* **2009**, *323*, 760.
- (6) Jaouen, F.; Proietti, E.; Lefevre, M.; Chenitz, R.; Dodelet, J.-P.; Wu, G.; Chung, H. T.; Johnston, C. M.; Zelenay, P. Recent advances in non-precious metal catalysis for oxygen-reduction reaction in polymer electrolyte fuel cells. *Energy Environ. Sci.* **2011**, *4*, 114.
- (7) Bezerra, C. W. B.; Zhang, L.; Lee, K.; Liu, H.; Marques, A. L. B.; Marques, E. P.; Wang, H.; Zhang, J. A review of Fe-N/C and Co-N/C catalysts for the oxygen reduction reaction. *Electrochim. Acta* **2008**, *53*, 4937.
- (8) Liang, Y.; Wang, H.; Zhou, J.; Li, Y.; Wang, J.; Regier, T.; Dai, H. Covalent Hybrid of Spinel Manganese-Cobalt Oxide and Graphene as Advanced Oxygen Reduction Electrocatalysts. *J. Am. Chem. Soc.* **2012**, *134*, 3517.
- (9) Jahan, M.; Bao, Q.; Loh, K. P. Electrocatalytically Active Graphene-Porphyrin MOF Composite for Oxygen Reduction Reaction. *J. Am. Chem. Soc.* **2012**, *134*, 6707.
- (10) Liang, Y.; Li, Y.; Wang, H.; Zhou, J.; Wang, J.; Regier, T.; Dai, H. Co₃O₄ nanocrystals on graphene as a synergistic catalyst for oxygen reduction reaction. *Nat. Mater.* **2011**, *10*, 780.

- (11) Zhang, C.; Hao, R.; Yin, H.; Liu, F.; Hou, Y. Iron phthalocyanine and nitrogen-doped graphene composite as a novel non-precious catalyst for the oxygen reduction reaction. *Nanoscale* **2012**, *4*, 7326.
- (12) Jasinski, R. A New Fuel Cell Cathode Catalyst. *Nature* **1964**, *201*, 1212.
- (13) Cheng, F.; Su, Y.; Liang, J.; Tao, Z.; Chen, J. MnO₂-Based Nanostructures as Catalysts for Electrochemical Oxygen Reduction in Alkaline Media. *Chem. Mater.* **2009**, *22*, 898.
- (14) Thorum, M. S.; Yadav, J.; Gewirth, A. A. Oxygen Reduction Activity of a Copper Complex of 3,5-Diamino-1,2,4-triazole Supported on Carbon Black. *Angew. Chem. Int. Ed.* **2009**, *48*, 165.
- (15) Nekooi, P.; Akbari, M.; Amini, M. K. CoSe nanoparticles prepared by the microwave-assisted polyol method as an alcohol and formic acid tolerant oxygen reduction catalyst. *Int. J. Hydrogen Energy* **2010**, *35*, 6392.
- (16) Cracknell, J. A.; Vincent, K. A.; Armstrong, F. A. Enzymes as Working or Inspirational Electrocatalysts for Fuel Cells and Electrolysis. *Chem. Rev.* **2008**, *108*, 2439.
- (17) Yang, W.; Fellingner, T.-P.; Antonietti, M. Efficient Metal-Free Oxygen Reduction in Alkaline Medium on High-Surface-Area Mesoporous Nitrogen-Doped Carbons Made from Ionic Liquids and Nucleobases. *J. Am. Chem. Soc.* **2010**, *133*, 206.
- (18) Liu, R.; Wu, D.; Feng, X.; Müllen, K. Nitrogen-Doped Ordered Mesoporous Graphitic Arrays with High Electrocatalytic Activity for Oxygen Reduction. *Angew. Chem. Int. Ed.* **2010**, *49*, 2565.
- (19) Zhao, Y.; Watanabe, K.; Hashimoto, K. Self-Supporting Oxygen Reduction Electrocatalysts Made from a Nitrogen-Rich Network Polymer. *J. Am. Chem. Soc.* **2012**, *134*, 19528.
- (20) Wu, G.; More, K. L.; Johnston, C. M.; Zelenay, P. High-Performance Electrocatalysts for Oxygen Reduction Derived from Polyaniline, Iron, and Cobalt. *Science* **2011**, *332*, 443.
- (21) Mahmood, J.; Kim, D.; Jeon, I.-Y.; Lah, M. S.; Baek, J.-B. Scalable Synthesis of Pure and Stable Hexaaminobenzene Trihydrochloride. *Synlett* **2013**, *24*, 246.
- (22) Mahmood, J.; Lee, E. K.; Jung, M.; Shin, D.; Jeon, I.-Y.; Jung, S.-M.; Choi, H.-J.; Seo, J.-M.; Bae, S.-Y.; Sohn, S.-D.; Park, N.; Oh, J. H.; Shin, H.-J.; Baek, J.-B. Nitrogenated holey two-dimensional structures. *Nat. Commun.* **2015**, *6*, 6486.
- (23) Kim, S.; Nahm, K.; Kim, P. High Electrocatalytic Performance of NH₃-Activated Iron-Adsorbed Polyaniline for Oxygen Reduction Reactions. *Catal. Lett.* **2012**, *142*, 1244.

(24) Wu, A.; Liu, D.; Tong, L.; Yu, L.; Yang, H. Magnetic properties of nanocrystalline Fe/Fe₃C composites. *CrystEngComm* **2011**, *13*, 876.

V. C₂N-*h*2D polymer encapsulated cobalt oxide catalyst for hydrogen evolution

5.1 Abstract

Cobalt oxides being a promising catalyst for hydrogen generation, 2D polymer supported cobalt oxides catalyst with good crystallinity is highly expected to enhance the catalytic performance. Here, I report for the first time the fabrication of 2D nitrogenated porous polymer encapsulated cobalt catalyst (Co@C₂N) via solvothermal synthesis and catalytic performance of Co@C₂N on the catalytic hydrolysis of neutral and alkaline sodium borohydride (NaBH₄) solutions. Co@C₂N exhibits very high activities for the hydrogen (H₂) generation from the hydrolysis of neutral and alkaline NaBH₄ solutions. The maximum hydrogen generation rate is comparable to most of the reported values of other metal contained catalyst performed in alkaline solutions. The Co@C₂N catalyst was also evaluated as reducing agent for the nitro group in 4-nitrophenol. The results obtained in this study showed that Co@C₂N is a promising candidate to replace noble metal catalyst in the H₂ evolution from the hydrolysis of NaBH₄.

5.2 Introduction

Today, hydrogen is considered as a neat and effective fuel and excellent alternative to fossil fuels. In fuel cells, hydrogen is regarded as environmentally friendly anodic fuel to generate electricity. However, many problems are associated with the safe and convenient utilization of hydrogen fuel. One of the foremost is to search for ideal hydrogen storage materials and efficient process to control the storage and release of hydrogen. At present, sodium borohydride (NaBH₄) is regarded as convenient hydrogen storage source with high densities of hydrogen available, and it is crucial to develop suitable catalyst for controlled hydrogen release.¹ Catalytic decomposition of the sodium borohydride is an easy method to obtain clean hydrogen, where the catalysts play a vital role to control the speed and extent of hydrogen release. The hydrogen evolution reaction of NaBH₄ at the surface of suitable catalyst at ambient condition is as follows.²



The most popular catalysts for obtaining hydrogen from hydrides are mainly based on the noble metals such as Ru and Pt.^{3,4} However, due to very high cost and limited supply of noble metals, extensive focus has been given to look for alternative catalysts composed of inexpensive materials.⁵ Transition metal oxides are broadly used as a catalyst due to their diversity of oxidation states for efficient redox charge transfer.⁶ Cobalt oxides have been recognized for their nontoxicity, high stability,

and low cost,⁷⁻¹⁵ and investigated as a catalyst for oxygen reduction and evolution reactions in fuel cells and water splitting.^{16,17} In addition, cobalt oxide can work as an efficient catalyst precursor for NaBH₄ hydrolysis as it can be reduced in situ to form active Co_xB catalyst.^{7,18,19} Crystalline cobalt oxides and high surface area are conducive for NaBH₄ hydrolysis on the surface of the catalyst.^{20,21} Hence, cobalt oxide materials with good crystallinity and large surface area are promising for catalytic application. By implanting the crystalline metal oxide on carbon support, the crystallinity and surface area can be enhanced. A number of techniques, such as electrochemical deposition,²² hydrothermal process,²³ thermal decomposition,⁶ thermal oxidation²⁴ and spray pyrolysis²⁵ have been implied to produce cobalt oxide nanostructures.^{7,26-28} Recently, porous single crystal and ordered mesoporous CoO structures were developed by using template method.^{7,29,30} However, cobalt oxide with 2D polymer framework has never been reported up to now for hydrogen evolution and heterogeneous reduction catalyst.

In this study, the crystalline cobalt oxides encapsulated in the 2D porous polymer framework³¹ as a support is reported. The encapsulated cobalt oxide 2D porous polymer framework shows outstanding catalytic activity for NaBH₄ hydrolysis in neutral and alkaline solution being better to those of the respective reported pure metal based catalysts. The material was also evaluated as reduction catalyst for the reduction of 4-nitrophenol to 4-aminophenol.

5.3 Materials

All the solvents, chemicals and reagents were purchased from Aldrich Chemical Inc., unless otherwise stated. Solvents were degassed with nitrogen purging before use. All the reactions were performed under nitrogen atmosphere using oven dried glassware. 1,2,3,4,5,6-hexaaminobenzene was synthesized according to literature procedure.³²

5.4 Instrumentation

Thermogravimetric analysis (TGA) was conducted in air and nitrogen atmosphere at a heating rate of 10 °C/min using a Thermogravimetric Analyzer Q200 TA Instrument, USA. The surface area was calculated by nitrogen adsorption-desorption isotherms using the Brunauer-Emmett-Teller (BET) method on Micromeritics ASAP 2504N. Scanning electron microscope (SEM) images were taken on Field Emission Scanning Electron Microscope Nanonova 230 FEI, USA. X-ray photoelectron spectroscopy (XPS) was performed on X-ray Photoelectron Spectroscopy Thermo Fisher K-alpha (UK). X-ray diffraction (XRD) studies were taken on High Power X-Ray Diffractometer D/MAZX 2500V/PC (Cu-K α radiation, 35 kV, 20 mA, $\lambda = 1.5418 \text{ \AA}$) Rigaku, Japan. High resolution transmission electron microscopy (TEM) was performed by using JEM-2100F (JEOL, Japan) under an operating voltage of 200 keV. The samples for TEM were prepared by drop casting NMP dispersion on Quantifoil holey

carbon TEM grid and dried in oven at 80 °C. XPS were recorded on a Thermo Fisher K-alpha spectrometer. Elemental analysis was conducted with Thermo scientific Flash 2000.

5.5 Synthesis of Co@C₂N

CoCl₂ (1.15g) was first dissolved in dry NMP (80 ml) on the ice bath in round bottom flask and then added 1.5 g (5.403 mmol) of Hexaketocyclohexane followed by 1.68 g (5.403 mmol) of HAB under the nitrogen atmosphere and refluxed for 8 hours. After 8 hours NaBH₄ solution (10 wt% 40 mL in NMP) was slowly added to the room temperature cooled reaction mixture and refluxed again for 5 hours. Then the mixture was filtered through 0.5 μm PTFE membrane. The reaction mixture was filtered and thoroughly Soxhlet extracted with methanol and water. The sample was dried in oven and annealed at 450°C for 2 hours under argon atmosphere.

5.6 Catalyst test

In typical experiment, an oven dried flask containing 10 mg of the Co@C₂N catalyst was evacuated and flushed with nitrogen efficiently. Then 3 mL of 10 wt% NaBH₄ solution and 3 mL 5 wt% NaOH was injected into the rubber plug sealed flask through a syringe. The volume of the H₂ generated was calculated using water displacement method. The reaction temperature was managed by immersing the flask in a temperature controlled oil bath.

5.7 Catalytic reduction reaction

10 mg of Co@C₂N catalyst was taken in two neck flask with 40 mL deionized water. Then added 2g of 4-nitrophenol and 20 mL 10 % solution of NaBH₄. The mixture was stirred at room temperature till the yellowish solution color completely disappear after 30-60 minutes. After completion of reaction the reaction mixture was filtered to remove the catalyst. The filtrate was evaporated to dryness to give quantitative yield of 4-aminophenol. The product was characterized by NMR and Mass spectrometry.

5.8 Results and discussion

The material was synthesized simply by taking cobalt chloride (CoCl₂) with hexaketocyclohexane (HKH) and hexaaminobenzene (HAB)³² in NMP and reacted under reflux for 8 hours in nitrogen atmosphere. After completion of the framework formation, NaBH₄ dissolved in N-methyl-2-pyrrolidone (NMP) was added to the solution and refluxed again for 5 hours (**Figure 5.1a**). Then the reaction mixture was precipitated in water and filtered through 0.5 μm PTFE membrane. The resultant black solid was Soxhlet extracted with water and methanol for 2 days each and freeze dried at -120 °C

for 3 days. After freeze drying the black powder was annealed at 450 °C for 2 hours under argon atmosphere. After annealing the material shows strong attraction toward external magnet (**Figure 5.1b**).

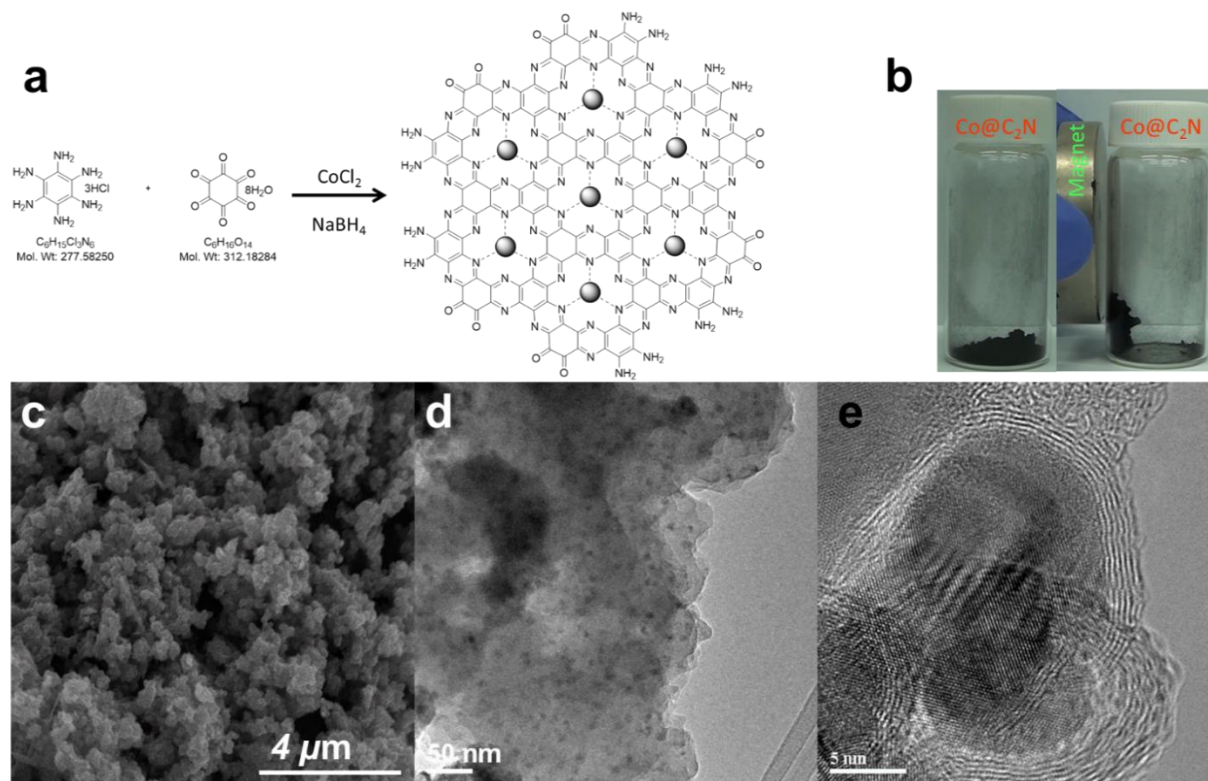


Figure 5.1. (a) Schematic presentation of the Co@C₂N synthesis; (b) the behavior of Co@C₂N in the magnetic field. Co@C₂N in a vial without magnetic field (left); Co@C₂N in the vial with magnetic field (right), revealing magnetic attraction of the black Co@C₂N particles toward magnet and the material is accumulated on the side of the glass wall; (c) SEM image of the Co@C₂N; (d) low-magnification HR-TEM image; (e) high magnification HR-TEM image, disclosing the C₂N polymer encapsulated Co nanoparticles.

The polymer is represented by C₂N for the repeating unit in the basal plane (**Figure 5.1a**) and the cobalt oxide embedded structure is denoted by Co@C₂N. Scanning electron microscope (SEM) and high-resolution transmission electron microscope (HR-TEM) were used to study the morphology and to look deep in the Co@C₂N material (**Figures 5.1c,d,e**) structure. HR-TEM study of the Co@C₂N material revealed the presence of well distributed particles in the C₂N polymer framework (**Figure 5.1d**) with average diameter of approximately 10-40 nm. High magnification image shows that Co nanoparticles are very nicely encapsulated with C₂N framework. The number of coated C₂N layers varies from 2-10 in the Co@C₂N. Selected-area electron diffraction (SAED) pattern of the Co@C₂N

can be assigned to diffraction planes of the crystalline structure of the nanoparticles coated with C₂N layers (**Figure 5.1e**). The C₂N layers can be easily distinguished around the outer surface of the Co nanoparticles with interlayer spacing of 0.35 nm. These results exhibit that the encapsulation of the Co nanoparticles inside the C₂N framework; which protects the Co nanoparticles and enhances the stability and activity.

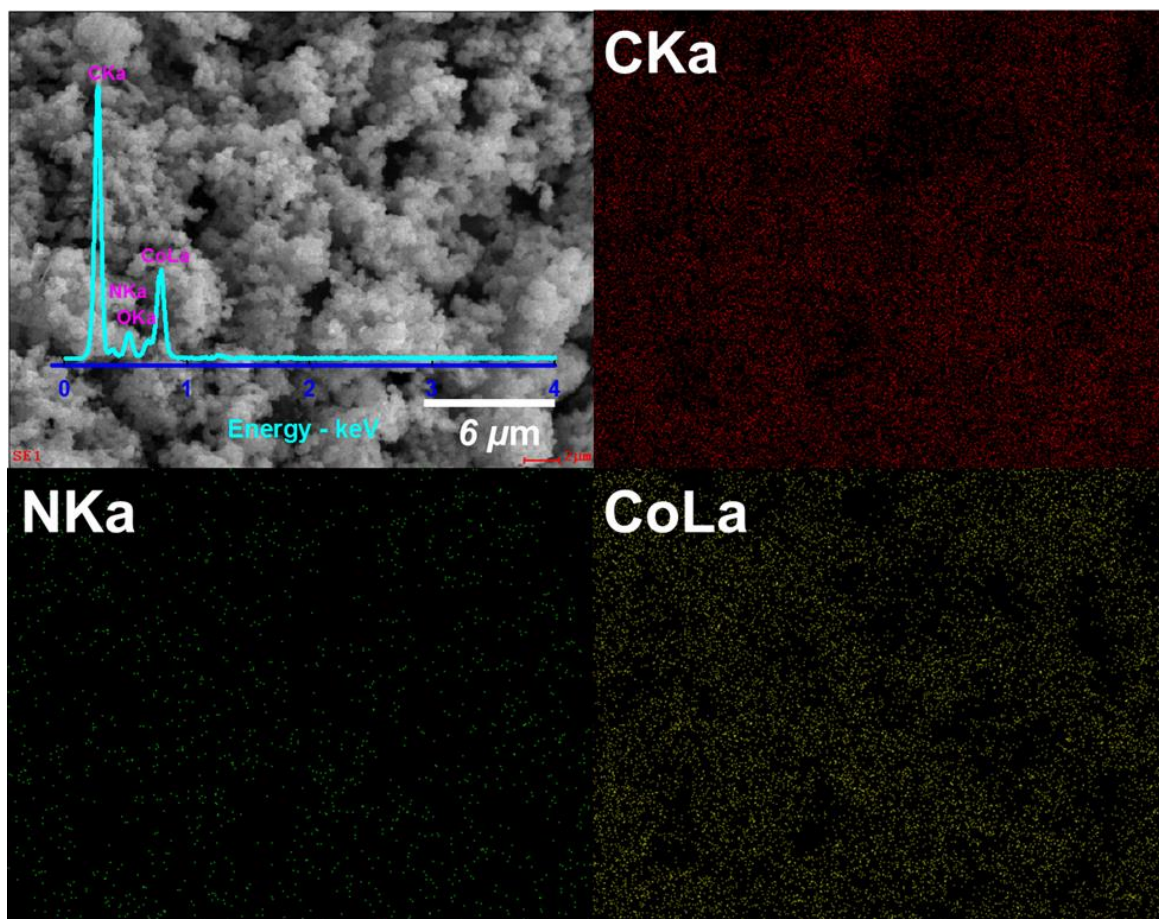


Figure 5.2. Co@C₂N energy dispersive X-ray spectroscopy (EDS) showing the elemental mapping and composition (C, N, O and Co) from the SEM image.

The elemental analysis (EA) revealed that the Co@C₂N catalyst contains 30 wt % cobalt oxide with 70 wt % polymer (**Table 5.1**) and thermogravimetric analysis (TGA) results (**Figure 5.3**) also support the EA results. SEM coupled energy dispersive spectroscopy (SEM-EDS) was also used to confirm the elemental composition in the Co@C₂N (**Figure 5.2**). Uniform distribution of Co nanoparticles in the Co@C₂N framework were detected by elemental mappings in the SEM-EDS analysis. EDS and XPS (**Figure 5.5a**) survey spectra of the Co@C₂N material shows the presence of C, N, O and Co and the

detail data are summarized in the **Table 5.1**. Deconvoluted XPS spectrum (**Figure 5.4**) of Cobalt reveals that Co in the Co@C₂N material mainly in form of Co⁺² state (inset in **Figure 5.5a**)³³.

Table 5.1. Elemental composition from different techniques

Technique	C	Co	H	N	O	Total
EA Wt%	33.88	2.35	15.02	19.80	71.05
XPS AT%	58.73	5.53	14.72	21.02	100
EDS (SEM) Wt%	33.62	34.37	15.25	16.76	100
EDS (SEM) At%	50.73	10.57	19.73	18.98	100

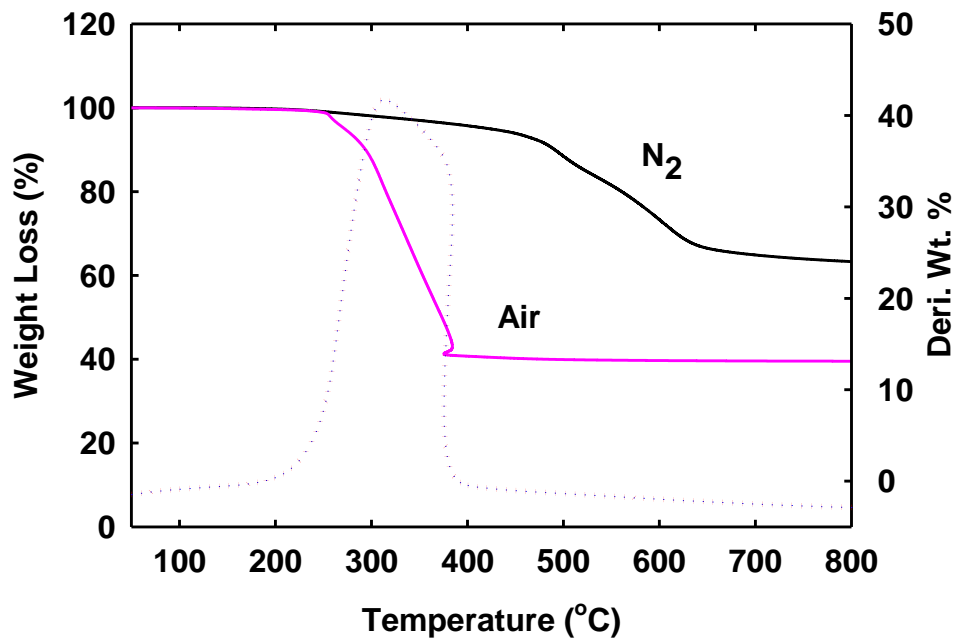


Figure 5.3. TGA from the Co@C₂N in air and nitrogen atmosphere.

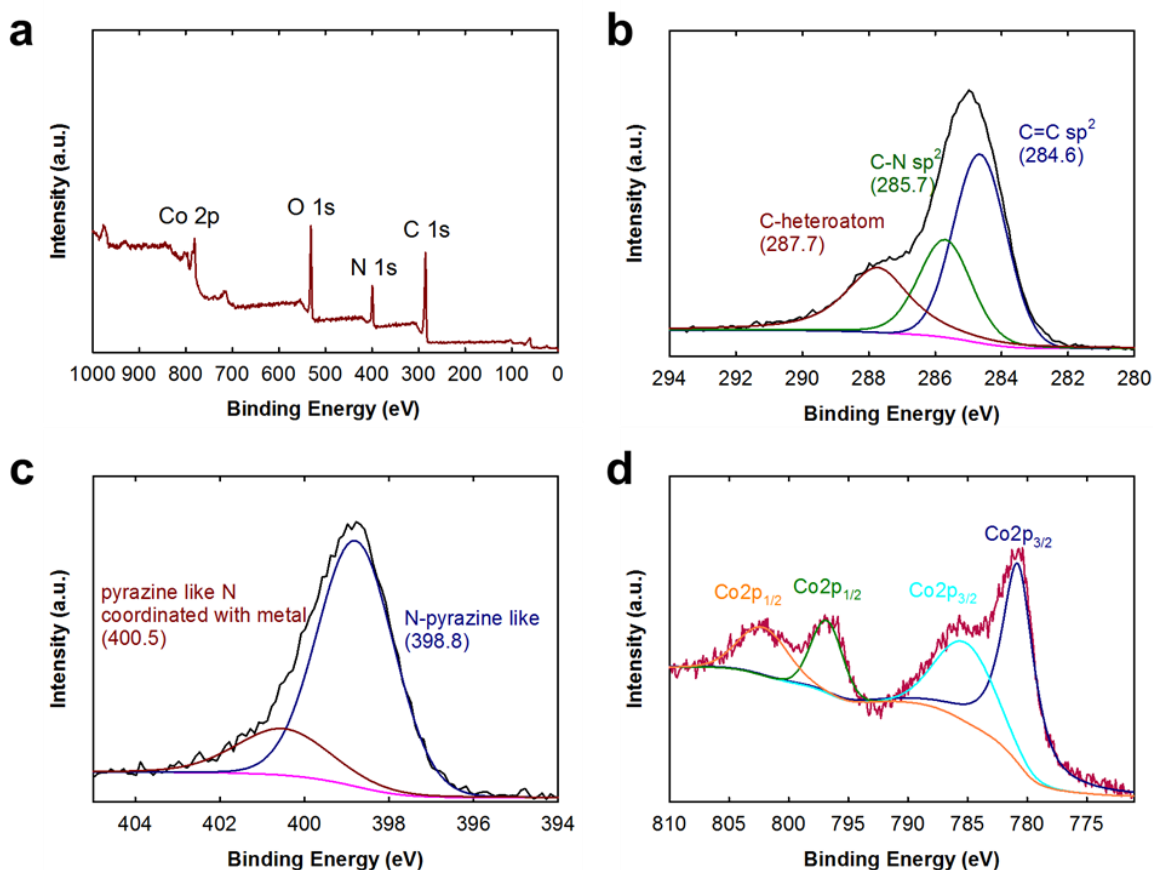


Figure 5.4. (a) XPS survey spectrum of Co@C₂N showing C1s, Co 2p, N1s and O1s. Deconvoluted spectra of Co@C₂N (b) C1s; (c) N1s; (d) Co 2p.

The powder X-ray diffraction (XRD) pattern of the Co@C₂N after annealing at 450 °C reveals that its structure is highly crystalline (**Figure 5.5b**). The XRD pattern of Co@C₂N is shown in figure 5.5b. The diffraction peaks marked with dark red spots at 2θ values of 19.02 °, 31.23 °, 36.72 °, 38.05 °, 44.52 °, 55.50 °, 59.40 ° and 65.06 ° for the crystal can be assigned to the (111), (220), (311), (222), (400), (422), (511) and (440) planes of cobalt oxide (Co₃O₄) crystal, respectively. While the peaks spotted with blue at 2θ values of 42.40 ° and 61.52 ° for the cobaltous oxide (CoO) crystal can be assigned to the (200) and (220) planes of the CoO crystals, respectively. XRD profile indicates mainly the presence of Co₃O₄ and CoO in the material as an active catalyst for hydrogen evolution (JCPDS 78-0431). From the XRD spectrum it is clear that the concentration of Co₃O₄ is more than CoO.

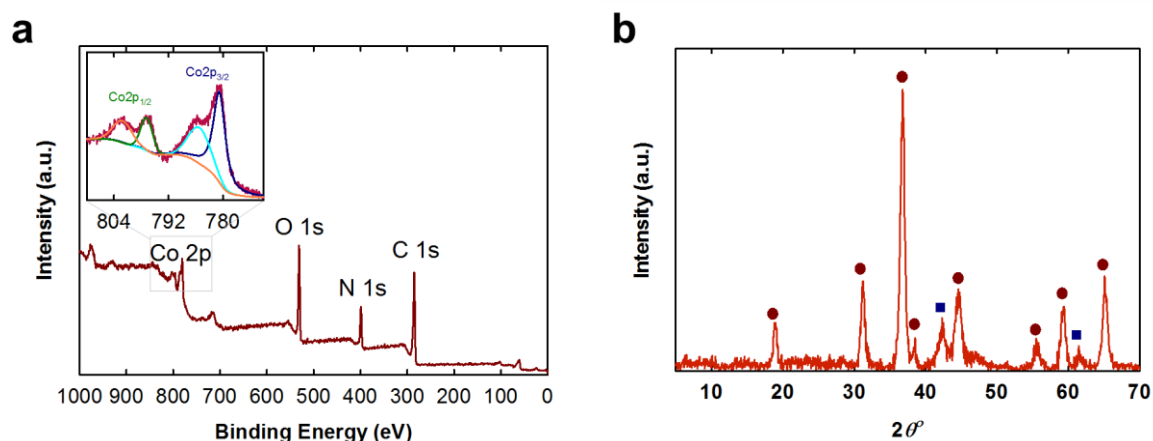


Figure 5.5. XPS and HP-XRD of the Co@C₂N material. (a) Survey XPS spectrum with the inset Co deconvoluted spectrum; (b) Powder XRD pattern from the Co@C₂N material.

After annealing at 450 °C the material was used as a catalyst for the hydrogen production by NaBH₄ hydrolysis in alkaline media. The plots of H₂ generation volume as a function of time at different temperature are shown in **Figure 5.6a**. Quite obviously, the H₂ generation rate increases with the increase in temperature due to accelerated movement of the NaBH₄ molecules.¹⁹ It can be seen that the volume of total H₂ volume generated always approaches 1500 mL, which is the maximum theoretical value for the added NaBH₄ dosage can provide.²⁰ Furthermore, the Co@C₂N achieves the maximum H₂ generation rate of 8903 mL min⁻¹ g⁻¹ at 303 K. As Co@C₂N catalyst contains 30 % cobalt catalyst the actual rate may be much higher than the reported value. These results indicate that Co@C₂N has a very high catalytic activity and can be excellent substitute for the noble metal catalyst in the catalytic generation of the H₂ via hydrolysis of NaBH₄. The Arrhenius activation energy (E_a) for the catalytic reaction can be calculated using the following equation:

$$r = k_0 \exp\left(-\frac{E_a}{RT}\right) \quad (2)$$

Where r denotes the reaction rate, R the universal gas constant, k_0 the reaction constant, and T the reaction temperature. The values of rate constant k at different temperature are calculated from the slope of the initial linear part of each plot. From the slope of Arrhenius plot shown in **Figure 5.6b**, the Arrhenius activation energy of Co@C₂N is calculated to be about 66.174 kJ mol⁻¹. The low Arrhenius activation energy may be due to synergic effect of 2D C₂N polymer on the Co catalyst.

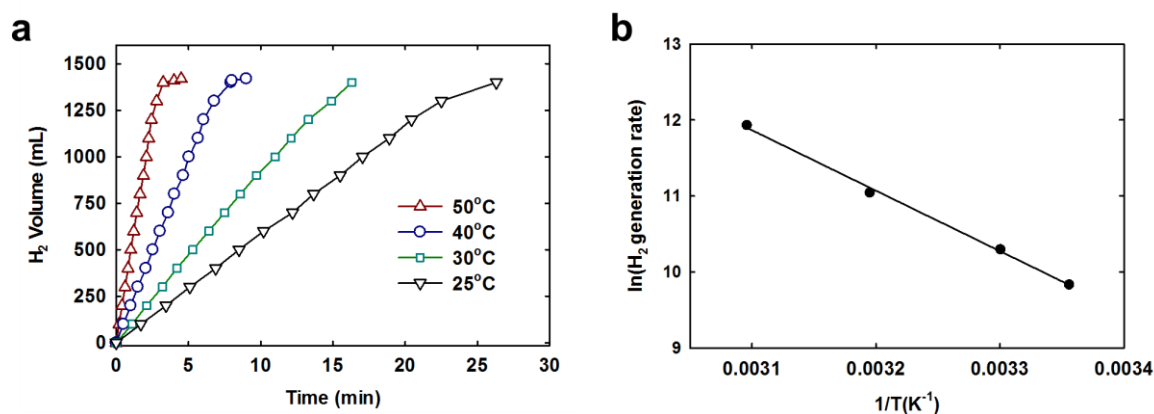


Figure 5.6. Catalytic hydrogen generation of Co@C₂N. (a) Hydrogen generation rate for Co@C₂N at different temperature; (b) Corresponding Arrhenius plot obtained from the data in a.

The stability of the Co@C₂N was explored during the hydrolysis of NaBH₄. Co@C₂N revealed good stability, nearly maintaining the activity up to five run (**Figure 5.7a**). The efficient catalytic properties may arise from the possible two reasons. One could be high surface area, which provides more active sites for catalytic reaction and the second is 2D C₂N polymer protected nanoparticles; the porous 2D polymer coating imparts synergic effect by providing large surface and well dispersed protected particle in the matrix. Brunauer, Emmett and Teller (BET) surface area was measured by nitrogen adsorption/desorption analysis on Co@C₂N catalyst (**Figure 5.7b**). The specific surface area was measured to be 231 m²/g with average pore diameter 4.54 nm.

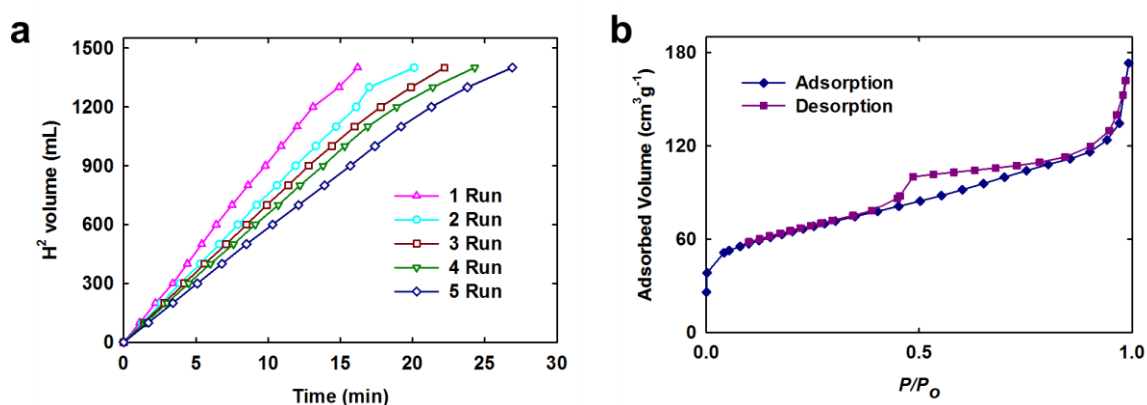


Figure 5.7. (a) Stability test of Co@C₂N during catalysis at 303 K. (b) Nitrogen adsorption and desorption isotherm for Co@C₂N.

4-Nitrophenol widely present in wastewater is originated from the agricultural and industrial sources, and it has been regarded to be one of the most widespread organic pollutant.³⁴ Additionally, the transformation from nitro to amino has great potential industrial values such as for aniline and paracetamol production.³⁵ The catalytic reduction of 4-nitrophenol to 4-aminophenol by NaBH_4 was first reported by Pal in 2002 using silver nanoparticles as the catalyst³⁶ and it has been the commonly used reaction to test the catalytic activity in aqueous solution under mild conditions.³⁷ $\text{Co@C}_2\text{N}$ was also used as a heterogeneous catalyst to catalyze the hydrogenation of 4-nitrophenol. The product, 4-aminophenol, is an important synthon for the chemical and pharmaceutical industry. It is mainly produced by the hydrogenation of nitrobenzene over precious metals³⁸ under hydrogen at relatively high pressure. Interestingly, $\text{Co@C}_2\text{N}$ itself can catalyze very efficiently the reduction of 4-nitrophenol to 4-aminophenol at room temperature in the presence of NaBH_4 with almost quantitative yield. The product was characterized by NMR, and Mass spectrometry.

5.9 Conclusions

In summary, a facile and scalable method is reported for the synthesis of 2D polymer encapsulated cobalt catalyst ($\text{Co@C}_2\text{N}$). The synthesized $\text{Co@C}_2\text{N}$ possesses highly active sites and exhibit outstanding catalytic activities towards NaBH_4 hydrolysis comparable to other metal catalysts. The maximum H_2 evolution rate of the $\text{Co@C}_2\text{N}$ catalyst exceeds most reported values of transition metal or noble metal containing catalyst carried out at similar condition. Thus the hydrolysis of NaBH_4 can be achieved at ambient condition and hydrogen gas can be evolved at an appreciable rate. $\text{Co@C}_2\text{N}$ has great potential to be used as a new catalyst for reduction of nitro groups with high activity. The results obtained in this study paves the way for the application of $\text{Co@C}_2\text{N}$ as an excellent lead for the catalytic production of pure hydrogen.

5.10 References

- (1) Clark, T. J.; Whittell, G. R.; Manners, I. Highly Efficient Colloidal Cobalt- and Rhodium-Catalyzed Hydrolysis of $\text{H}_3\text{N BH}_3$ in Air. *Inorg. Chem.* **2007**, *46*, 7522.
- (2) Schlesinger, H. I.; Brown, H. C.; Finholt, A. E.; Gilbreath, J. R.; Hoekstra, H. R.; Hyde, E. K. Sodium Borohydride, Its Hydrolysis and its Use as a Reducing Agent and in the Generation of Hydrogen. *J. Am. Chem. Soc.* **1953**, *75*, 215.
- (3) Wu, C.; Zhang, H.; Yi, B. Hydrogen generation from catalytic hydrolysis of sodium borohydride for proton exchange membrane fuel cells. *Catal. Today* **2004**, *93–95*, 477.

- (4) Özkar, S.; Zahmakıran, M. Hydrogen generation from hydrolysis of sodium borohydride using Ru(0) nanoclusters as catalyst. *J. Alloys Compd.* **2005**, *404–406*, 728.
- (5) Tong, D.-G.; Han, X.; Chu, W.; Chen, H.; Ji, X.-Y. Preparation and characterization of Co-B flowers with mesoporous structure. *Mater. Res. Bull.* **2008**, *43*, 1327.
- (6) Ryu, J.; Kim, S.-W.; Kang, K.; Park, C. B. Synthesis of Diphenylalanine/Cobalt Oxide Hybrid Nanowires and Their Application to Energy Storage. *ACS Nano* **2009**, *4*, 159.
- (7) Zhang, H.; Ling, T.; Du, X.-W. Gas-Phase Cation Exchange toward Porous Single-Crystal CoO Nanorods for Catalytic Hydrogen Production. *Chem. Mater.* **2014**.
- (8) Rakhi, R. B.; Chen, W.; Cha, D.; Alshareef, H. N. Substrate Dependent Self-Organization of Mesoporous Cobalt Oxide Nanowires with Remarkable Pseudocapacitance. *Nano Lett.* **2012**, *12*, 2559.
- (9) Xie, X.; Li, Y.; Liu, Z.-Q.; Haruta, M.; Shen, W. Low-temperature oxidation of CO catalysed by Co₃O₄ nanorods. *Nature* **2009**, *458*, 746.
- (10) Zhu, Z.; Li, X.; Zeng, Y.; Sun, W.; Zhu, W.; Huang, X. T. Application of Cobalt Oxide Nanoflower for Direct Electrochemistry and Electrocatalysis of Hemoglobin with Ionic Liquid as Enhancer. *J. Phys. Chem. C* **2011**, *115*, 12547.
- (11) Melaet, G.; Ralston, W. T.; Li, C.-S.; Alayoglu, S.; An, K.; Musselwhite, N.; Kalkan, B.; Somorjai, G. A. Evidence of Highly Active Cobalt Oxide Catalyst for the Fischer–Tropsch Synthesis and CO₂ Hydrogenation. *J. Am. Chem. Soc.* **2014**, *136*, 2260.
- (12) Polshettiwar, V.; Baruwati, B.; Varma, R. S. Self-Assembly of Metal Oxides into Three-Dimensional Nanostructures: Synthesis and Application in Catalysis. *ACS Nano* **2009**, *3*, 728.
- (13) Huang, X.-l.; Wang, R.-z.; Xu, D.; Wang, Z.-l.; Wang, H.-g.; Xu, J.-j.; Wu, Z.; Liu, Q.-c.; Zhang, Y.; Zhang, X.-b. Homogeneous CoO on Graphene for Binder-Free and Ultralong-Life Lithium Ion Batteries. *Adv. Funct. Mater.* **2013**, *23*, 4345.
- (14) Varghese, B.; Zhang, Y.; Dai, L.; Tan, V. B. C.; Lim, C. T.; Sow, C.-H. Structure-Mechanical Property of Individual Cobalt Oxide Nanowires. *Nano Lett.* **2008**, *8*, 3226.
- (15) Seo, W. S.; Shim, J. H.; Oh, S. J.; Lee, E. K.; Hur, N. H.; Park, J. T. Phase- and Size-Controlled Synthesis of Hexagonal and Cubic CoO Nanocrystals. *J. Am. Chem. Soc.* **2005**, *127*, 6188.

- (16) Liu, J.; Jiang, L.; Zhang, B.; Jin, J.; Su, D. S.; Wang, S.; Sun, G. Controllable Synthesis of Cobalt Monoxide Nanoparticles and the Size-Dependent Activity for Oxygen Reduction Reaction. *ACS Catal.* **2014**, *4*, 2998.
- (17) Liao, L.; Zhang, Q.; Su, Z.; Zhao, Z.; Wang, Y.; Li, Y.; Lu, X.; Wei, D.; Feng, G.; Yu, Q.; Cai, X.; Zhao, J.; Ren, Z.; Fang, H.; Robles-Hernandez, F.; Baldelli, S.; Bao, J. Efficient solar water-splitting using a nanocrystalline CoO photocatalyst. *Nat. Nanotechnol.* **2014**, *9*, 69.
- (18) Krishnan, P.; Advani, S. G.; Prasad, A. K. Cobalt oxides as Co₂B catalyst precursors for the hydrolysis of sodium borohydride solutions to generate hydrogen for PEM fuel cells. *Int. J. Hydrogen Energy* **2008**, *33*, 7095.
- (19) Simagina, V. I.; Komova, O. V.; Ozerova, A. M.; Netskina, O. V.; Odegova, G. V.; Kellerman, D. G.; Bulavchenko, O. A.; Ishchenko, A. V. Cobalt oxide catalyst for hydrolysis of sodium borohydride and ammonia borane. *Appl. Catal. A* **2011**, *394*, 86.
- (20) Lu, A.; Chen, Y.; Jin, J.; Yue, G.-H.; Peng, D.-L. CoO nanocrystals as a highly active catalyst for the generation of hydrogen from hydrolysis of sodium borohydride. *J. Power Sources* **2012**, *220*, 391.
- (21) Pfeil, T. L.; Pourpoint, T. L.; Groven, L. J. Effects of crystallinity and morphology of solution combustion synthesized Co₃O₄ as a catalyst precursor in hydrolysis of sodium borohydride. *Int. J. Hydrogen Energy* **2014**, *39*, 2149.
- (22) Meng, Z.; Liu, B.; Zheng, J.; Sheng, Q.; Zhang, H. Electrodeposition of cobalt oxide nanoparticles on carbon nanotubes, and their electrocatalytic properties for nitrite electrooxidation. *Microchim. Acta* **2011**, *175*, 251.
- (23) Jiang, J.; Liu, J.; Ding, R.; Ji, X.; Hu, Y.; Li, X.; Hu, A.; Wu, F.; Zhu, Z.; Huang, X. Direct Synthesis of CoO Porous Nanowire Arrays on Ti Substrate and Their Application as Lithium-Ion Battery Electrodes. *J. Phys. Chem. C* **2009**, *114*, 929.
- (24) Varghese, B.; Teo, C. H.; Zhu, Y.; Reddy, M. V.; Chowdari, B. V. R.; Wee, A. T. S.; Tan, V. B. C.; Lim, C. T.; Sow, C. H. Co₃O₄ Nanostructures with Different Morphologies and their Field-Emission Properties. *Adv. Funct. Mater.* **2007**, *17*, 1932.
- (25) Lupu, F.; Kamalakaran, R.; Gulino, A. Viable Route for Cobalt Oxide–Carbon Nanocomposites. *J. Phys. Chem. C* **2009**, *113*, 15533.
- (26) Risbud, A. S.; Snedeker, L. P.; Elcombe, M. M.; Cheetham, A. K.; Seshadri, R. Wurtzite CoO. *Chem. Mater.* **2005**, *17*, 834.

- (27) An, K.; Lee, N.; Park, J.; Kim, S. C.; Hwang, Y.; Park, J.-G.; Kim, J.-Y.; Park, J.-H.; Han, M. J.; Yu, J.; Hyeon, T. Synthesis, Characterization, and Self-Assembly of Pencil-Shaped CoO Nanorods. *J. Am. Chem. Soc.* **2006**, *128*, 9753.
- (28) Li, D.; Ding, L.-X.; Wang, S.; Cai, D.; Wang, H. Ultrathin and highly-ordered CoO nanosheet arrays for lithium-ion batteries with high cycle stability and rate capability. *J. Mater. Chem. A* **2014**, *2*, 5625.
- (29) Ren, Y.; Bruce, P. G.; Ma, Z. Solid-solid conversion of ordered crystalline mesoporous metal oxides under reducing atmosphere. *J. Mater. Chem.* **2011**, *21*, 9312.
- (30) Tüysüz, H.; Weidenthaler, C.; Schüth, F. A Strategy for the Synthesis of Mesostructured Metal Oxides with Lower Oxidation States. *Chem. Eur. J.* **2012**, *18*, 5080.
- (31) Mahmood, J.; Lee, E. K.; Jung, M.; Shin, D.; Jeon, I.-Y.; Jung, S.-M.; Choi, H.-J.; Seo, J.-M.; Bae, S.-Y.; Sohn, S.-D.; Park, N.; Oh, J. H.; Shin, H.-J.; Baek, J.-B. Nitrogenated holey two-dimensional structures. *Nat. Commun.* **2015**, *6*, 6486.
- (32) Mahmood, J.; Kim, D.; Jeon, I.-Y.; Lah, M. S.; Baek, J.-B. Scalable Synthesis of Pure and Stable Hexaaminobenzene Trihydrochloride. *Synlett* **2013**, *24*, 246.
- (33) Dominguez, M.; Taboada, E.; Idriss, H.; Molins, E.; Llorca, J. Fast and efficient hydrogen generation catalyzed by cobalt talc nanolayers dispersed in silica aerogel. *J. Mater. Chem.* **2010**, *20*, 4875.
- (34) Nemanashi, M.; Meijboom, R. Synthesis and characterization of Cu, Ag and Au dendrimer-encapsulated nanoparticles and their application in the reduction of 4-nitrophenol to 4-aminophenol. *J. Colloid Interface Sci.* **2013**, *389*, 260.
- (35) Fenger, R.; Fertitta, E.; Kirmse, H.; Thunemann, A. F.; Rademann, K. Size dependent catalysis with CTAB-stabilized gold nanoparticles. *PCCP* **2012**, *14*, 9343.
- (36) Pradhan, N.; Pal, A.; Pal, T. Silver nanoparticle catalyzed reduction of aromatic nitro compounds. *Colloids Surf. A* **2002**, *196*, 247.
- (37) Herves, P.; Perez-Lorenzo, M.; Liz-Marzan, L. M.; Dzubiel, J.; Lu, Y.; Ballauff, M. Catalysis by metallic nanoparticles in aqueous solution: model reactions. *Chem. Soc. Rev.* **2012**, *41*, 5577.
- (38) Gelder, E.; Jackson, S. D.; Lok, C. M. A Study of Nitrobenzene Hydrogenation Over Palladium/Carbon Catalysts. *Catal. Lett.* **2002**, *84*, 205.

VI. Organic Ferromagnetism from Self-Polymerized TCNQ

6.1 Abstract:

I report on the design, synthesis, and magnetic properties of an organic π -conjugated triazine polymer demonstrating room-temperature ferromagnetism derived from purely organic compounds. The organic polymer was developed through the self-polymerization of tetracyanoquinodimethane (TCNQ) with the intent of producing highly stable free radicals as a result of the energy gain from the aromatization of the central ring in primary TCNQ. The free radicals encapsulated in this polymerized structure can be strongly coupled through the π -conjugated network. Magnetic characterization revealed the presence of spin $\frac{1}{2}$ moments, which partially lead to ferromagnetic ordering with a critical temperature that is significantly higher than room temperature.

6.2 Introduction

Intensive efforts have been made to develop magnets based on free radicals in purely organic compounds, driven both by scientific curiosity and by the potential applications of such materials^{1,2}. The flexible and low-temperature syntheses of these materials are perhaps their greatest advantage over traditional metal-based magnets. In addition, their low density, biocompatibility, and plasticity make them attractive candidates for replacing conventional magnets in certain applications³⁻⁵. Whereas the magnetic moments in traditional magnets emerge from unpaired electrons in *d* or *f* orbitals, the magnetism in organic and/or molecular magnets originates from unpaired electrons in *s* and *p* molecular orbitals. The study of organic magnets is generally focused on crystalline solids of small-molecule radicals or charge-transfer salts, which typically display ferromagnetic transitions at very low temperatures⁶⁻⁹. An alternative route for the synthesis of organic magnets is the polymerization of radicals along with a π -conjugated backbone¹⁰. The achievement of polymeric magnets that exhibit a T_C greater than 300 K has even been claimed in several reports¹¹. However, it is unclear whether it is possible to prepare well-defined materials of this type with reproducible magnetic characteristics¹¹. Recently, numerous studies have indicated that localized moments from various sp^3 defects in carbon allotropies could induce magnetic ordering, thus reviving the quest for room-temperature magnets based on π electrons¹²⁻¹⁴.

6.3 Materials & Instrumentations

7,7,8,8-Tetracyanoquinodimethan (TCNQ) was purchased from Alfa Aesar and recrystallized from distilled acetonitrile. Trifluoromethanesulfonic acid (TFMSA) was also purchased from the Alfa Aesar and freshly distilled under reduced pressure before use. Thermogravimetric analysis (TGA) was

conducted in air and nitrogen atmosphere at a heating rate of 10 °C/min using a Thermogravimetric Analyzer Q600 TA Instrument, USA. Scanning electron microscope (SEM) images were taken on Field Emission Scanning Electron Microscope Nanonova 230 FEI, USA. X-ray photoelectron spectroscopy (XPS) was performed on X-ray Photoelectron Spectroscopy Thermo Fisher K-alpha (UK). The surface area was measured by nitrogen adsorption-desorption isotherms using the Brunauer-Emmett-Teller (BET) method on Micromeritics ASAP 2504N. X-ray diffraction (XRD) studies were taken on High Power X-ray Diffractometer D/MAZX 2500V/PC (Cu-K α radiation, 35 kV, 20 mA, $\lambda = 1.5418 \text{ \AA}$) Rigaku, Japan.

6.4 Self-Polymerization of 7,7,8,8-tetracyanoquinodimethane (TCNQ)

TCNQ crystals (5.0 g) were taken in a three neck round bottom flask under the nitrogen flow and added 30 mL freshly distilled trifluoromethanesulfonic acid (TFMSA) and stirred at room temperature for 30 minutes. Then the temperature was gradually raised to 50, 100 and 140 °C and maintained at each temperature for 1 h. Then, the temperature was raised to 155 °C overnight. After completion of the reaction, the mixture converted into black thick gel-like material and thus efficient stirring was impossible. The reaction mixture was slowly cooled to room temperature and distilled water was added. The black cake product was collected and Soxhlet extracted with methanol and water successively for three days each to remove any possible impurity. Then the sample was filtered and freeze-dried at -120 °C under reduced pressure for three days to yield (quantitative) black powder. After freeze drying, the sample was further annealed at 370 °C to remove trapped impurities.

6.5 Electron spin resonance (ESR) measurements

ESR spectra were recorded with JES-FA100 (JEOL) Spectrometer (9.5 GHz) with a field modulation frequency of 100 KHz, using microwave power of 10 mW and modulation amplitude of 0.4 G. ESR is a form of magnetic resonance spectroscopy used to study the electronic structure of materials with unpaired electrons.

6.6 Results and discussion

Here, I report that the simple polymerization of tetracyanoquinodimethane (TCNQ), which is one of the commonly used organic charge-transfer materials for the formation of organic-based magnets, can induce highly stable free radicals as a result of the delocalization of the electrons. Magnetic characterizations of the resulting material revealed spontaneous magnetization and hysteresis with an ordering temperature exceeding 300 K. Although TCNQ is well known as a highly conducting molecule in its composite form^{15,16}, it has also been extensively studied as a building block for organic-based

magnets, similar to tetracyanoethylene (TCNE) ^{17,18}. Coordination between transition-metal ions and radical anions of TCNX (X = E, Q) leads to long-range magnetic order with a wide variation in critical temperatures. Among metal-TCNX (X = E, Q) compounds, V(TCNE)_x (x ~ 2) features magnetic ordering above room temperature with highly spin-polarized valence and conduction bands, which has been extensively characterized ^{8,19,20}. In this material, the anti-ferromagnetic exchange interaction between the spins in the π^* orbitals in the TCNE⁻ anions and the spins in the *d* orbitals of the V²⁺ cations leads to a net magnetic moment of 1 μ_B (per molecular formula unit) with a high ordering temperature. It would be intriguing to investigate the magnetic properties of a π -conjugated organic network without metal cations *via* self-polymerization of TCNQ. In addition, aromatization in the central ring of TCNQ could induce highly stable radicals if they are trapped in a polymerized network structure.

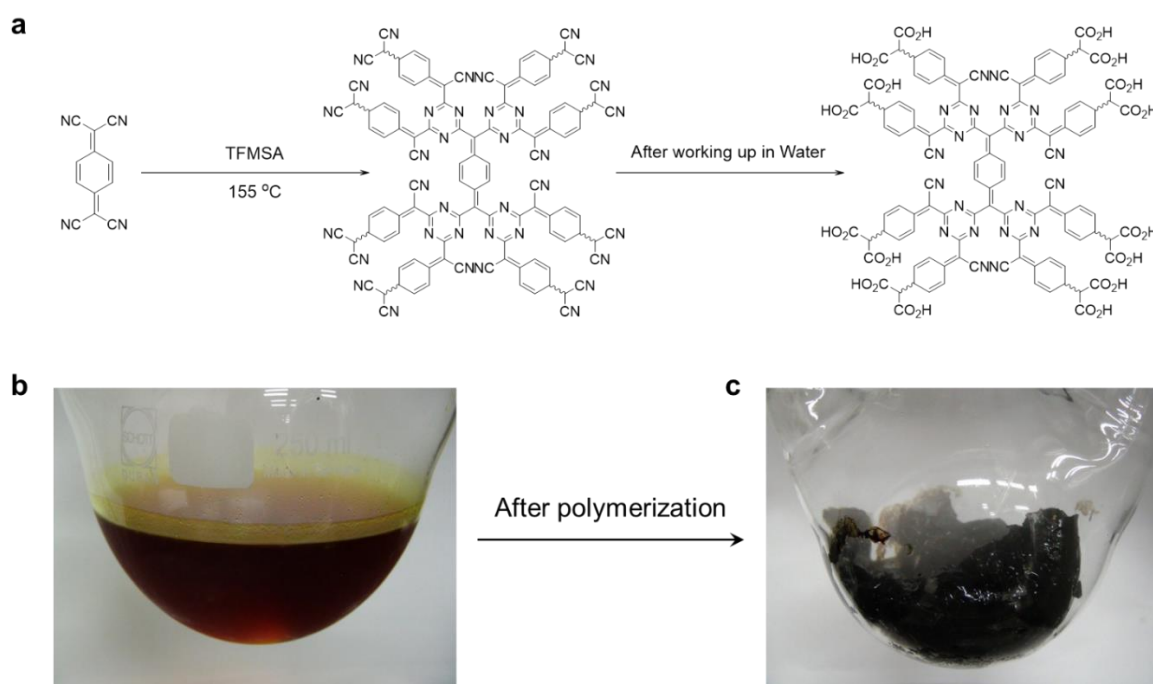


Figure 6.1. (a) Schematic presentation of the TCNQ framework with edge groups after aqueous quenching; (b) TCNQ dissolved in TFMSA after stirring at room temperature before self-polymerization; (c) complete gelation of the reaction mixture after polymerization at 155 °C overnight.

TCNQ, after self-polymerization at 155 °C in trifluoromethanesulfonic acid (TFMSA) overnight, was converted into a highly viscous black solid gel-like material (**Figure 6.1c**); the experimental details are provided in the Supplementary Materials. Trimerization of the cyano (-CN) groups in TCNQ leads to the formation of a triazine framework in the presence of TFMSA ²¹. The structure consists of a

quinone moiety surrounded by bulky aromatic triazine rings (**Figures 6.3a and 6.1a**). The resultant blackish appearance of the product served as evidence of an extended conjugated 3D structure. The product was Soxhlet extracted with methanol and water, respectively, to wash off any small-mass organic and inorganic impurities, if any. It was finally freeze dried at $-120\text{ }^{\circ}\text{C}$ under reduced pressure (0.05 mmHg). The product was heat treated at $370\text{ }^{\circ}\text{C}$ to completely remove any trapped solvent impurities. Its elemental composition was analyzed using X-ray photoelectron spectroscopy (XPS) and elemental analysis (EA), and the results were found to agree well with the theoretical values (**Figure 6.2 and Table 6.1**).

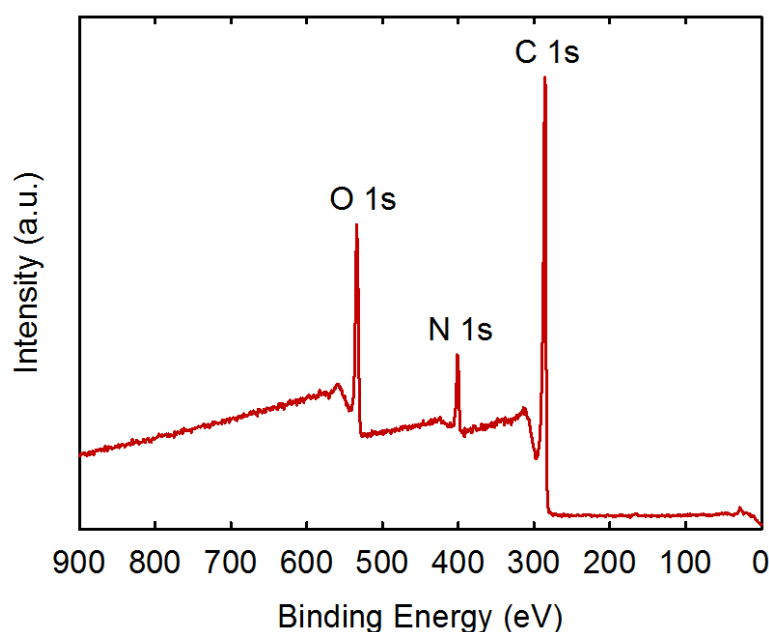


Figure 6.2. XPS survey spectrum from the *p*-TCNQ.

Thermogravimetric analysis (TGA) was performed to investigate the thermal deposition behavior of the sample. The data acquired in nitrogen (N_2) and air environments indicated good stability of the material (**Figure 6.4a**). The powder XRD spectrum exhibited a broad 2θ peak centered at 24.9° with a relatively high signal-to-noise ratio, implying the amorphous 3D nature of the self-polymerized TCNQ (*p*-TCNQ) (**Figure 6.4b**). The Brunauer-Emmett-Teller (BET) specific surface area of the *p*-TCNQ sample was approximately $36.0\text{ m}^2\text{ g}^{-1}$, reflecting the compact nature of the material. The bulk morphology of the *p*-TCNQ was examined *via* field-emission scanning electron microscopy (FE-SEM). The SEM images revealed that the sample consisted of grains of irregular shapes and sizes, typically several tens of microns in size, with an irregular texture (**Figure 6.5**).

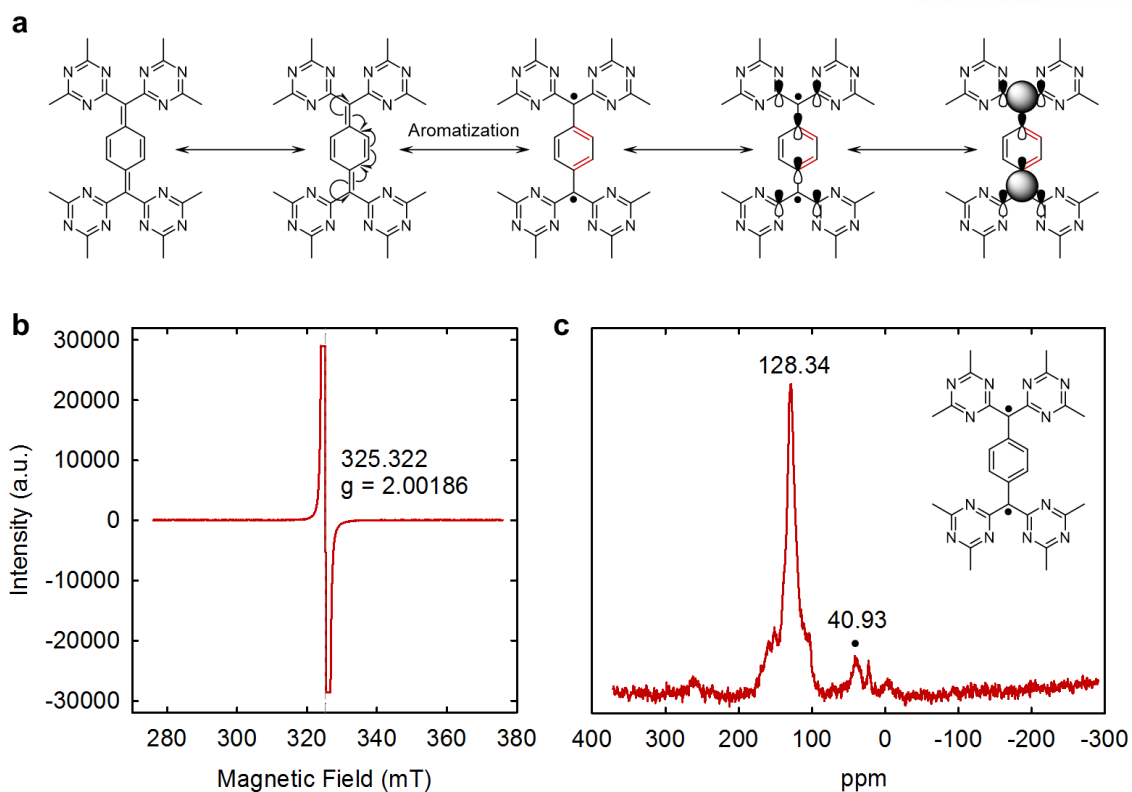


Figure 6.3. (a) Schematic representation of the radical formation and its stability in the structure.; (b) solid-state ESR spectrum of the sample under ambient conditions, showing an isotropic singlet; and (c) solid-state NMR revealing the presence of an unusual peak at 40.93 ppm, which is associated with the tertiary radical in the structure (indicated in the inset by a black dot).

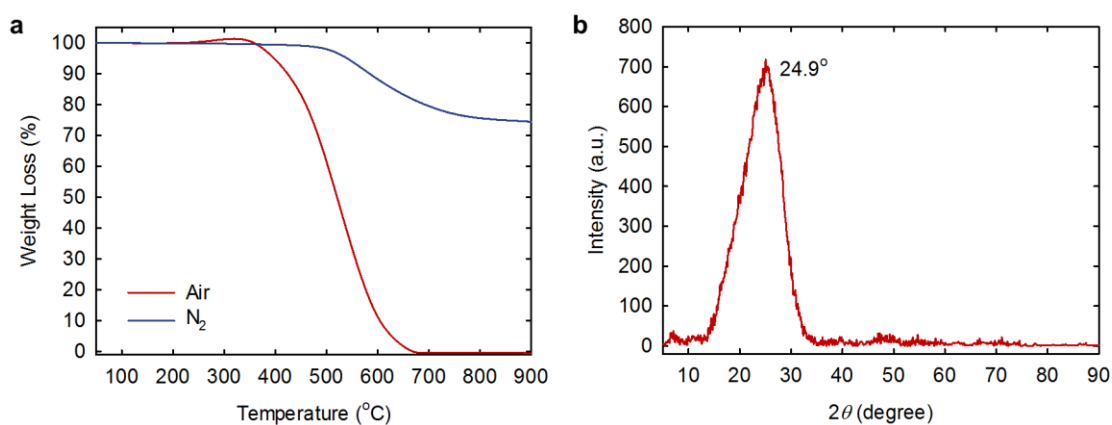


Figure 6.4. (a) TGA graph in inert (N₂) and air atmosphere; (b) powder XRD spectrum exhibiting a broad peak centered at $2\theta = 24.9^\circ$, implying the amorphous 3D nature of the material.

Table 6.1. Elemental composition of the *p*-TCNQ framework from different characterization techniques

Technique	C	H	N	O	Total
Theoretical (wt.%)	60.57	2.45	13.08	23.91	100
EA (wt.%)^a	61.42	3.00	9.57	25.49	99.48
XPS (at.%)^b	76.97	----	7.46	15.57	100

^a EA is most reliable element counts for bulk sample.

^b XPS is more sensitive to surface chemical composition.

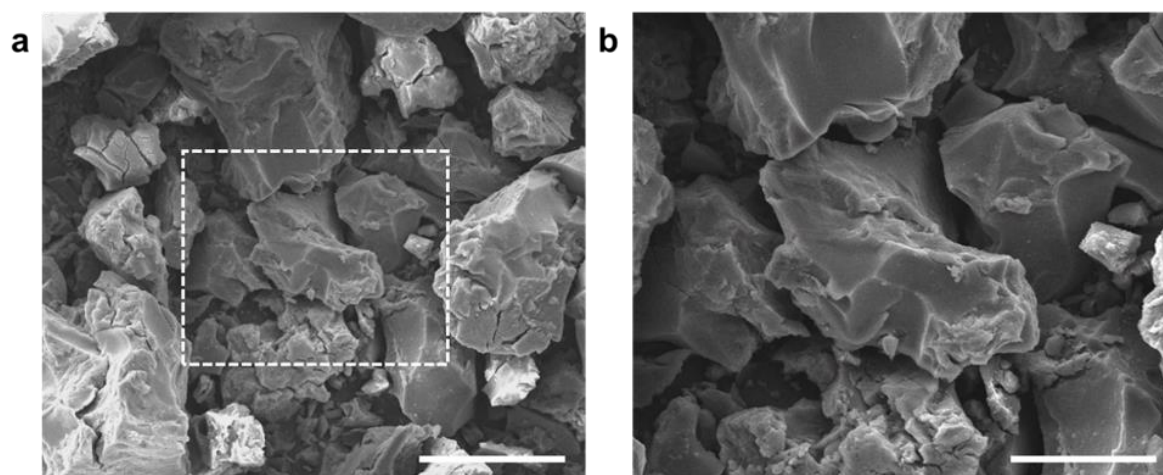


Figure 6.5 SEM images of the *p*-TCNQ at different magnification showing compact and irregular morphology: a, Lower magnification.(scale 100 μm) b, Higher magnification .(scale 50 μm).

Achieving the stability of free radicals at relatively high temperatures requires both kinetic stabilization through protection of the spin center with a large steric hindrance and thermodynamic stabilization through spin delocalization (resonance). In a *p*-TCNQ network, the free radicals originate from electron resonance and can be protected by a large steric hindrance in the network. The presence of an unpaired electron in *p*-TCNQ can be readily confirmed *via* solid-state electron spin resonance (ESR) spectroscopy. Figure 1B presents the ESR spectrum of *p*-TCNQ recorded at room temperature, which exhibits a sharp isotropic singlet ($g = 2.00186$) that is consistent with a carbon radical. The ESR spectrum clearly provides unambiguous evidence of the existence of free radicals in the *p*-TCNQ

framework at room temperature as well as low temperature (**Figure 6.6**). Interestingly, solid ^{13}C -NMR revealed unusual peaks at approximately 40 ppm related to the resonance-stabilized radical in the structure. After the trapped solvent and moisture were removed by annealing the material at 370 °C for two hours, the peak at ~40 ppm was stabilized (**Figure 6.3c**). This peak completely disappeared after annealing above 400 °C for two hours (**Figures 6.7a and 6.7b**), reflecting the transformation of the structure and the complete elimination of the radical. The solid-state ESR also supports this phenomenon of the annealing effect on the material (**Figures 6.8a and 6.8b**).

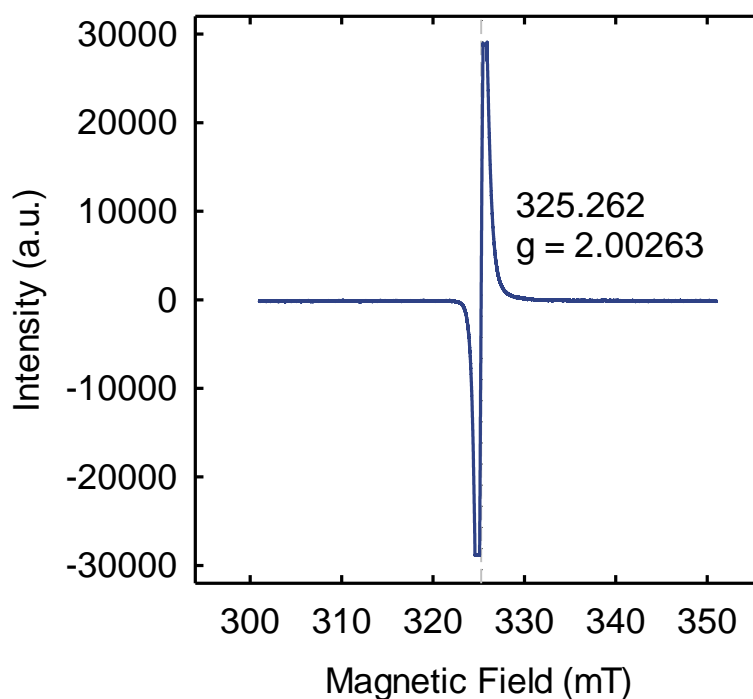


Figure 6.6. Solid-state ESR measured at -100 °C.

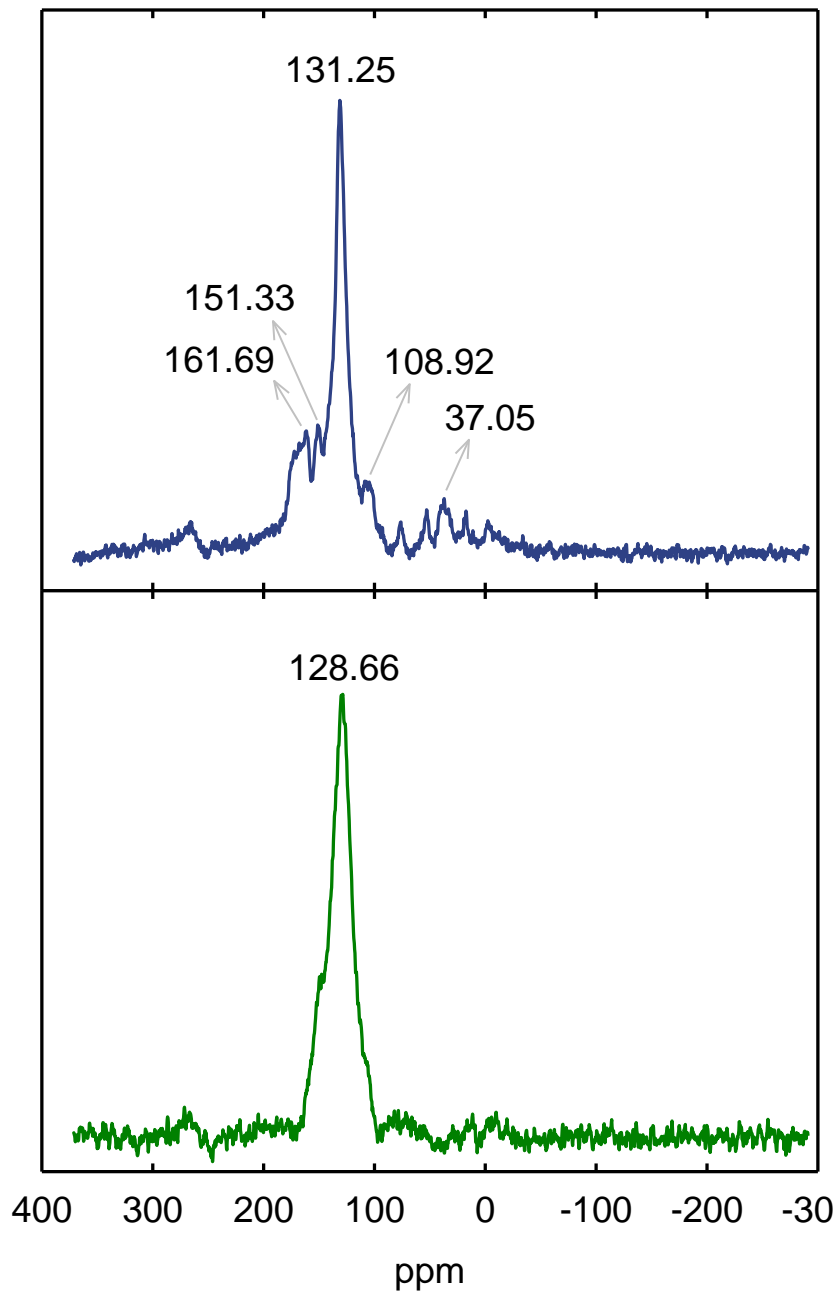


Figure 6.7. Solid-state NMR spectra: (a) as-prepared sample; (b) after annealing at 400 °C, which indicates the destruction of the structure and radicals.

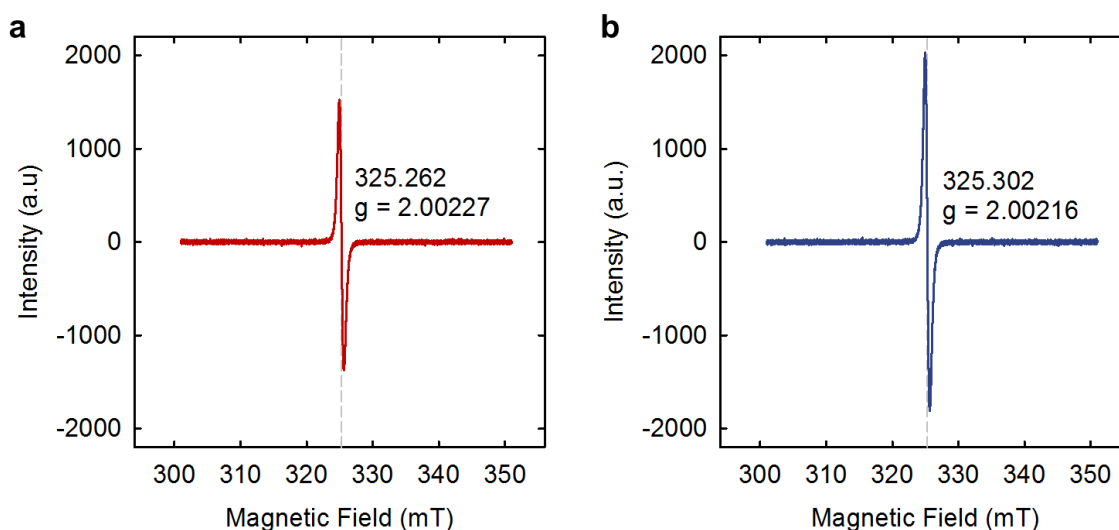


Figure 6.8. ESR spectra after annealing *p*-TCNQ above 400 °C: (a) at room temperature; (b) at -100 °C, showing the decrease in the intensity. These results are in good agreement with the solid-state ¹³C-NMR (Figure 6.7).

Depending on the degree of concentration, the presence of these radicals could induce long-range magnetic order through the π -conjugated network. The magnetic properties of the *p*-TCNQ framework were characterized using a Quantum Design SQUID-VSM. The background diamagnetic signal, which was estimated from the high-field results, was subtracted from all magnetic data (Figure 6.9). Figure 6.10 illustrates the field-dependent magnetization of samples recorded at 5 K and 300 K. Spontaneous magnetization with distinctive hysteresis was clearly observed even at 300 K, with non-zero coercivity and remanence. To test the stability of the magnetic moment in the *p*-TCNQ, the magnetization of the sample was measured after the sample had been stored under an N₂ atmosphere for three weeks, and the results did not indicate any noticeable degradation (Figure 6.11). Only a few species of molecule-based magnets have been reported to exhibit room-temperature magnetic order^{8,22}. Notable examples are the V-Cr Prussian analog²² and V(TCNE)_{x-2}⁸, in which the magnetic moments predominantly originate from the electron spins of transition ions. The CN moieties in the V-Cr Prussian analog mediate the magnetic coupling *via* superexchange, whereas the TCNEs in V(TCNE)_{x-2} provide spin, resulting in long-range magnetic order *via* direct coupling with the spins in the transition ions. My material, *p*-TCNQ, is a purely organic material that is free of metals, because the synthetic route does not involve any metal-containing precursors or catalysts. To rule out the possibility of the presence of any metallic impurities in the *p*-TCNQ framework, I performed ICP-MS to identify the trace metal contents in the material. The results are summarized in Table 6.2. The total concentration of all ferromagnetic metal impurities (Fe, Ni and Co) was found to be less than 0.030 ppm (close to negligible)

and insufficient to give rise to the magnetic moment ²³ observed in the *p*-TCNQ framework. Therefore, it can be safely stated that the observed ferromagnetism originates from the stable free radicals inherent in the *p*-TCNQ framework. Note that the $M(H)$ measured at 5 K increases almost linearly, even at relatively high fields. This behavior indicates the presence of non-interacting paramagnetic radicals along with robust ferromagnetism in my sample.

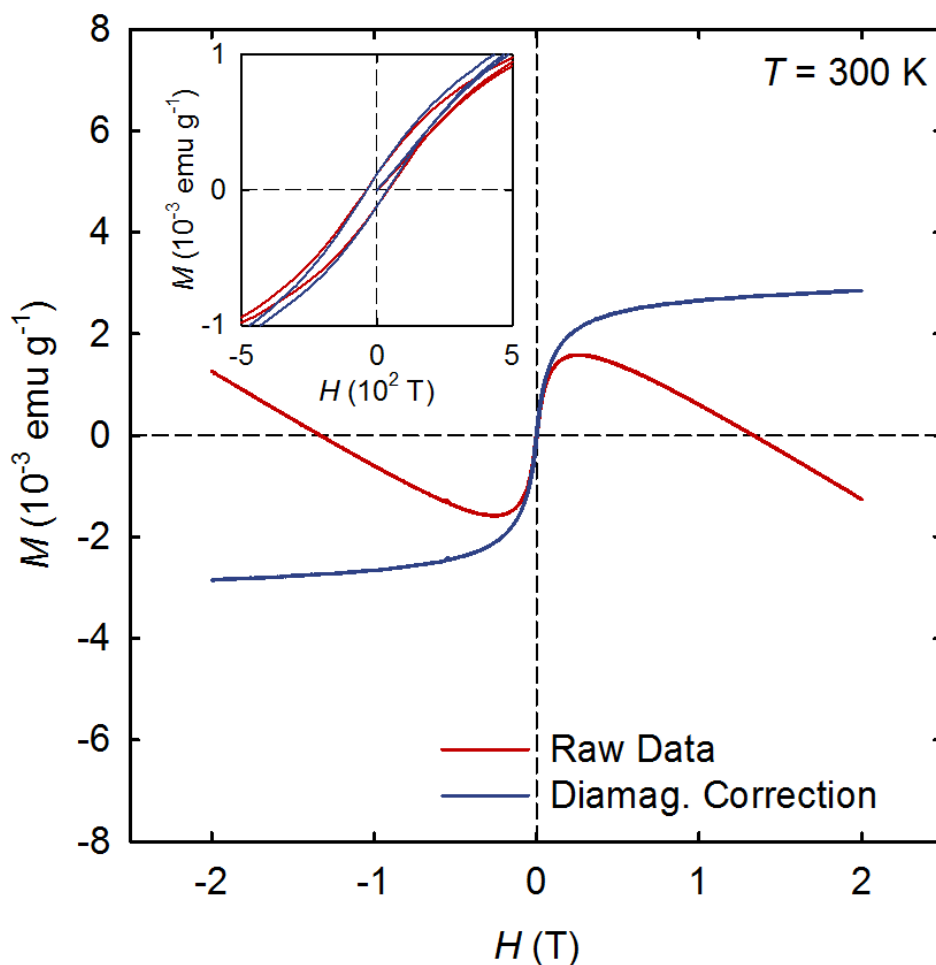


Figure 6.9. Magnetization as a function of field recorded at 300 K. Dark red line is the raw experimental data of magnetization. Dark blue line is magnetization after subtracting linear diamagnetic background. Inset displays low field hysteresis loop.

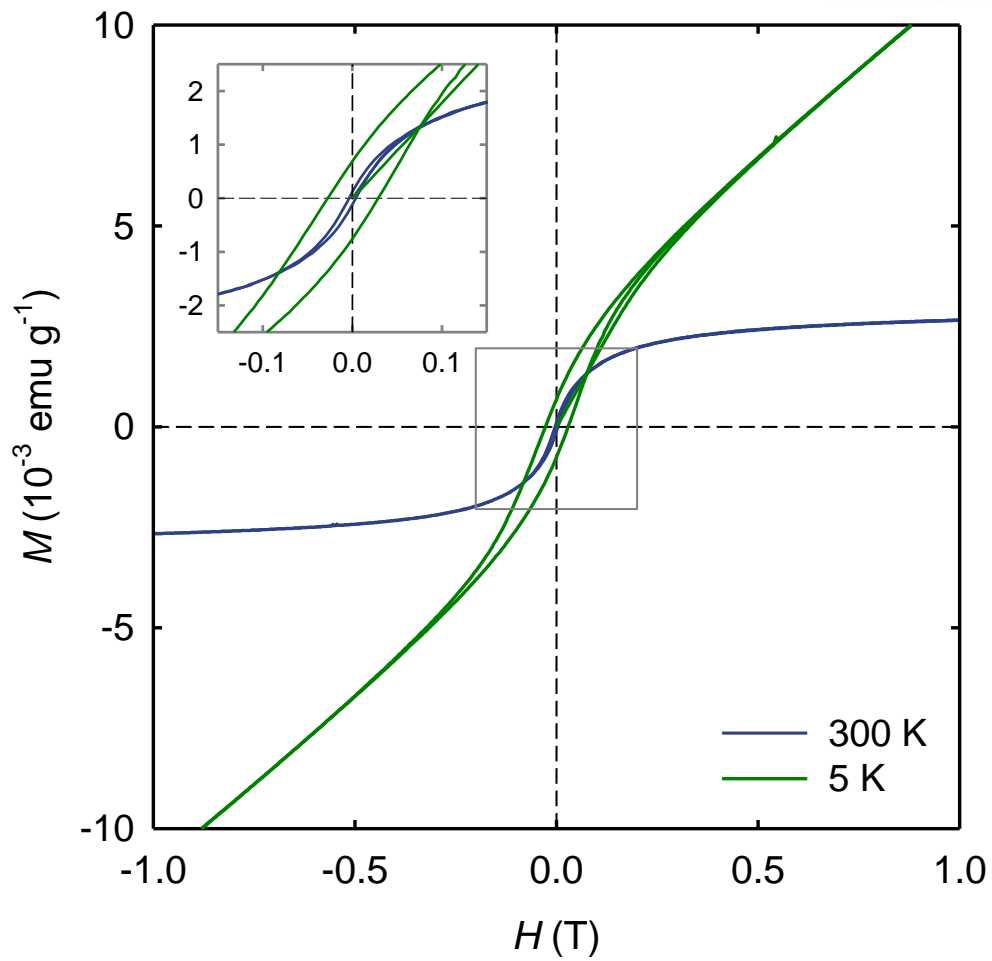


Figure 6.10. Magnetization as a function of the applied field (H), recorded at 300 K and 5 K. The linear diamagnetic background was subtracted from all data. Spontaneous magnetization was clearly observed, even at 300 K. The internal hysteresis loops are shown in the inset.

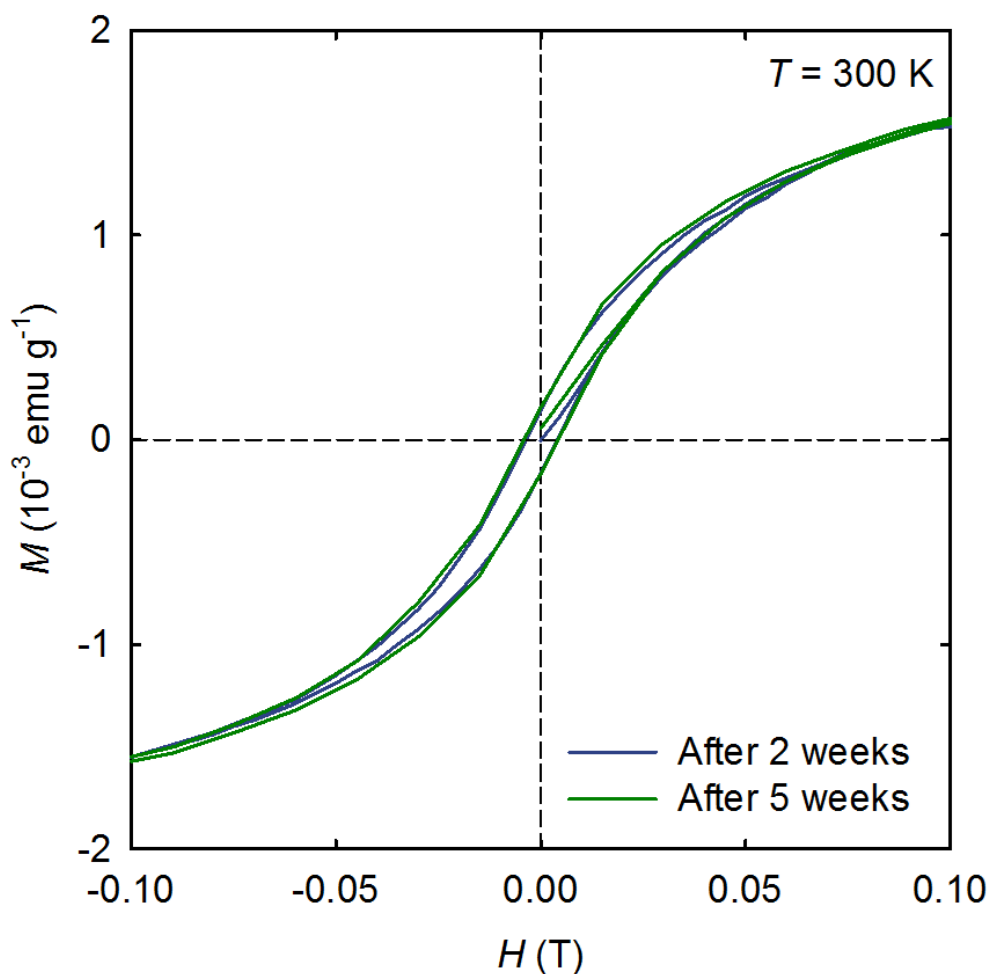


Figure 6.11. Magnetization as a function of field recorded at 300 K. Dark blue line is for data recorded two weeks after the synthesis of material and dark green line is for data recorded five weeks after the synthesis of material.

The temperature dependence of the field-cooled (FC) magnetization at $H = 1000$ Oe is depicted in Figure 6.12a. Surprisingly, spontaneous magnetization persists up to 400 K. The black line in **Figure 6.12a** illustrates the extrapolation of the critical temperature, $T_c \sim 495$ K. The value of T_c was estimated from the low-field $M(T)$ data by fitting these data to a functional form describing conventional critical behavior, $\propto (T_c - T)^\beta$ (**Figure 6.13**). This T_c value is substantially higher than that of any other molecule-based magnet. The value obtained for the critical exponent β was 0.48, which is close to that of the mean field theory.

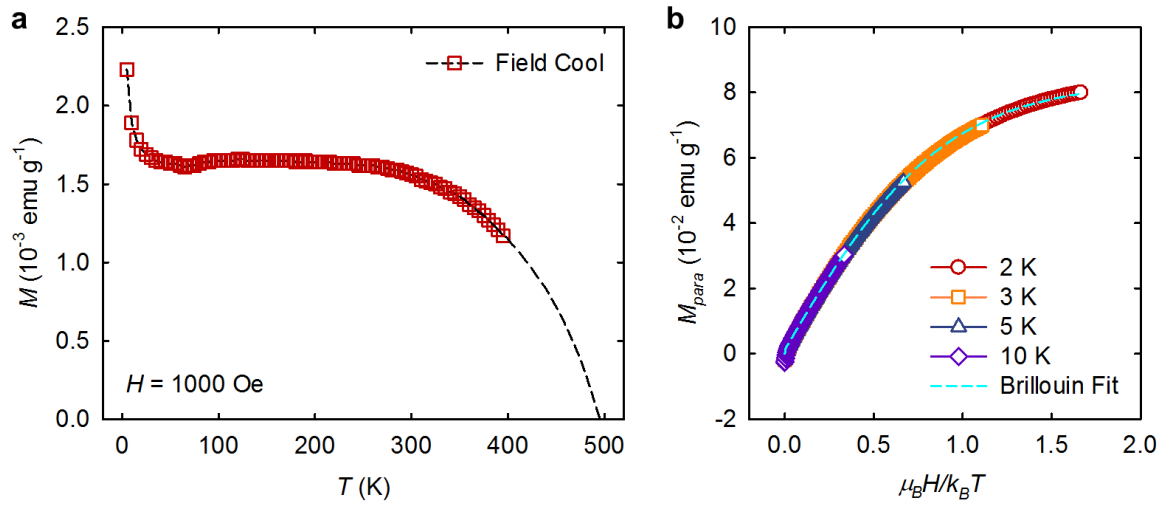


Figure 6.12. (a) Magnetization as a function of the temperature, recorded at 1000 Oe. Robust spontaneous magnetization persists up to 400 K. The estimated critical temperature is $T_c \sim 495$ K (Figure 6.14). The material also displays Curie-like behavior at low temperatures; (b) magnetization as a function of $\mu_B H/k_B T$ at various temperatures. The linear diamagnetic background and constant ferromagnetic component were subtracted from all data. The cyan line represents a fit to the Brillouin function with $J = S = 1/2$ under the assumption of $g = 2$. All curves collapse well into a single Brillouin function.

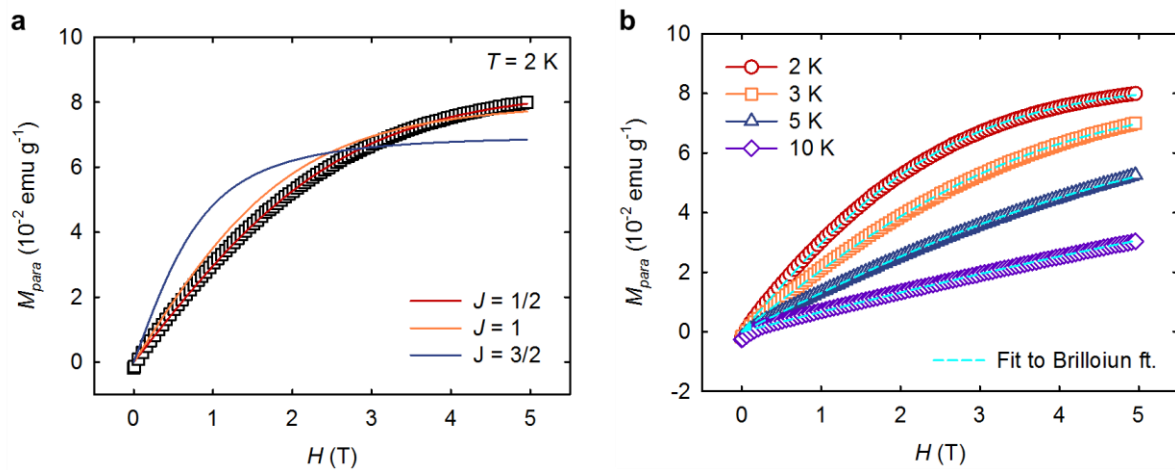


Figure 6.13. Determination of the angular momentum quantum number J via Brillouin function fit: (a) the estimated M_{para} component as a function of field H at 5 K (black symbols). Fitting to Brillouin function with $J = 1/2, 1, 3/2$ are indicated with solid lines, respectively. The g value was assumed to be 2 in fitting procedure. Only $J = 1/2$ produces excellent Brillouin function fit to the paramagnetic

component M_{para} ; (b) the estimated M_{para} component as a function of field H at different temperatures ($T = 2, 3, 5,$ and 10 K). Solid cyan curves are fits to Brillouin function with $J = 1/2$ and $g = 2$.

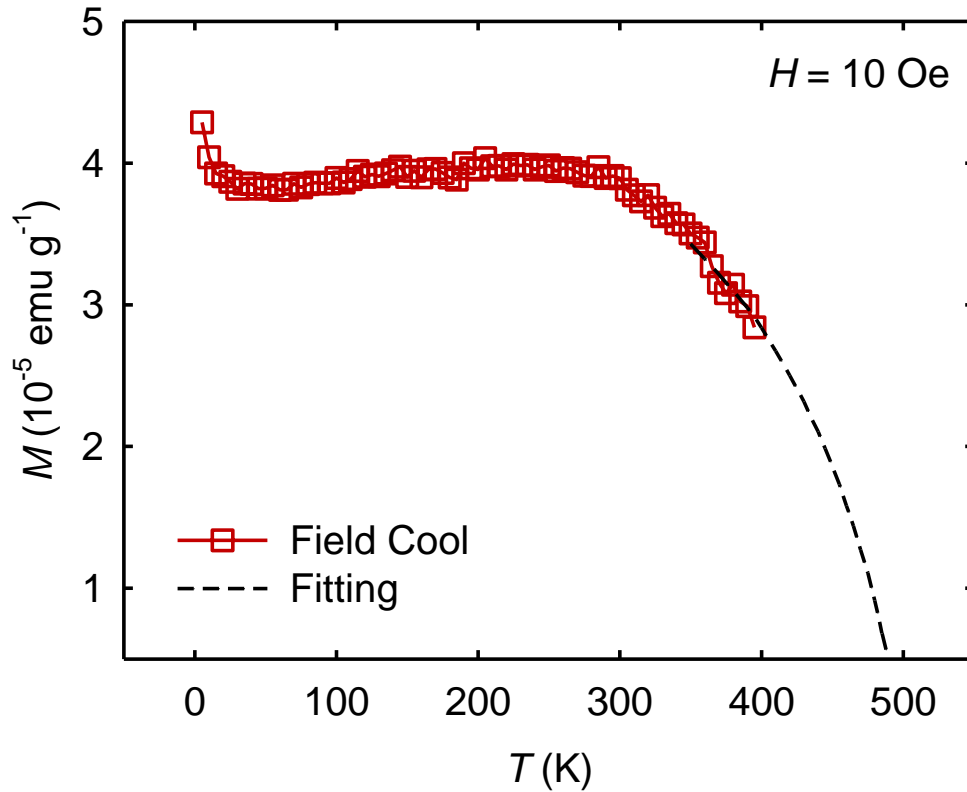


Figure 6.14. Field-cooled magnetization as a function of temperature measured at 10 Oe (dark red squares). Black line is fit to conventional critical behavior, $\propto (T_c - T)^\beta$ with recorded data between 350 K and 395 K. The estimated T_c is ~ 495 K. The best fitting parameter for the critical exponent β was 0.48, which is close to the value of the mean field theory.

Similar to $M(H)$ at 5 K, the low-temperature $M(T)$ data also display the typical signature of paramagnetic behavior (Figure 6.12a). Because the ferromagnetic component should saturate at a relatively low field, I can reasonably extract the paramagnetic component of $M(H)$, especially at very low T and very high H . Figure 6.12b displays the paramagnetic component of M_{para} measured at $T = 2, 3, 5,$ and 10 K. $M_{para}(H)$ was estimated by subtracting the ferromagnetic component, which was treated as a constant value, as well as the linear diamagnetic background. Using a scaled parameter of $\mu_B H / k_B T$,

all $M_{para}(H)$ curves measured at different temperatures can be effectively fit into a single Brillouin function as follows:

$$M = NgJ\mu_B \left[\frac{2J+1}{2J} \coth\left(\frac{2J+1}{2J} \cdot z\right) - \frac{1}{2J} \coth\left(\frac{z}{2J}\right) \right]$$

where $z = gJ\mu_B H / k_B T$, g is the g -factor, J is the total angular momentum number, k_B is the Boltzmann constant, and N is the number of spins. At all temperatures, the Brillouin function provides good fits only for $J = S = 1/2$; other values of S lead to significant deviations from the Brillouin function fit (**Figure 6.15**). The saturation magnetic moment for the ferromagnetic component, which was subtracted to produce the M_{para} component, was found to be $\sim 3.22 \times 10^{-3}$ emu g^{-1} . This value of the ferromagnetic moment is equivalent to $N \sim 3.59 \times 10^{19}$ spins per mol of the initial TCNQ unit of $C_{12}N_4H_4$ (where g is assumed to be 2). If normalize N , the fraction of interacting spins is $\sim 5.96 \times 10^{-5}$ mol $^{-1}$ (approximately one out of 16778 TCNQ units). The saturation paramagnetic moment estimated from the Brillouin function fit was 7.98×10^{-2} emu g^{-1} . This value of the magnetic moment is equivalent to the fraction of non-interacting spins, $\sim 1.48 \times 10^{-3}$ mol $^{-1}$ (approximately one out of 675 TCNQ units). Thus, the number of paramagnetic spins in my sample appears to be much higher than that of coupled ferromagnetic spins. Although the concentration of spins in the p -TCNQ network is very low, electron delocalization through the π -conjugated backbone could induce exchange coupling between the free radicals trapped in the network.

Table 6.2. Trace metal analysis of the impurities in the p -TCNQ framework determined by ICP-MS

Elements	Mg	Al	V	Cr	Mn	Fe	Co
Concentration (ppm)	0.00306	0.00390	0.00672	0.00401	0.000121	0.00619	0.0242
Elements	Ni	Cd	In	Pb	B	Ti	Zr
Concentration (ppm)	0.000288	0.0237	0.00514	0.00014	0.0894	0.0326	0.00132

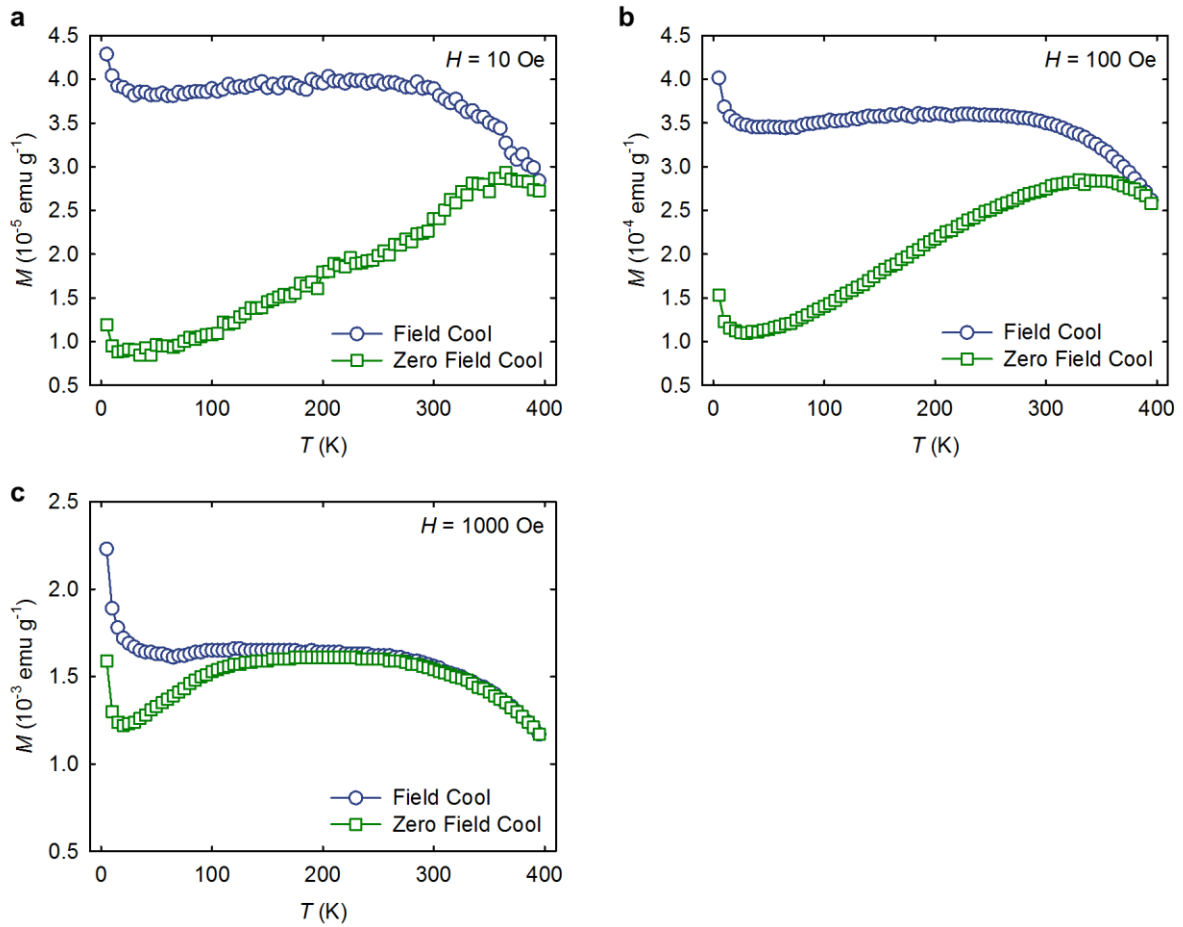


Figure 6.15. The temperature dependence of field-cooled (FC) vs. zero-field-cooled (ZFC) magnetizations. The measurements were done with applied fields of $H = 10$ (a), 100 (b), and 1000 Oe (c). The ZFC magnetizations were recorded after cooling of the sample in the absence of the magnetic field, while the FC magnetizations were recorded after cooling of the sample in applied magnetic fields (10, 100, and 1000 Oe). Upon reaching the lowest temperature of 5 K, magnetizations were measured on warming the sample in applied magnetic fields. The magnetization exhibited strong irreversibility, given by the divergence of the FC and ZFC magnetization curves below a bifurcation temperature (T_{irr}). The ZFC magnetization exhibited a maximum at a field-dependent temperature $T_{max} < T_{irr}$ and continuously decreased below this temperature. The bifurcation was shifted to lower temperature as H was increased. Strong irreversibility and the shift of T_{irr} to lower T with increasing H are signatures of spin glass like behavior. It is likely that my sample retains randomly distributed spin clusters leading to the glassy behavior.

6.7 Conclusions

In summary, I demonstrated a metal-free polymeric magnet fabricated *via* simple low-temperature processing. The highly stable free radicals achieved through the self-polymerization of TCNQ present as spin $\frac{1}{2}$ moments. The π -conjugated network in *p*-TCNQ might allow for ferromagnetic ordering even above room temperature. Designing and manipulating the spins in polymer networks *via* organic methodologies will provide alternative approaches for versatile future applications of plastic magnets.

6.8 References

- (1) Miller, J. S. Organic- and molecule-based magnets. *Mater. Today* **2014**, *17*, 224.
- (2) Blundell, S. J.; Pratt, F. L. Organic and molecular magnets. *J. Phys.: Condens. Matter* **2004**, *16*, R771.
- (3) Miller, J. S.; Epstein, A. J. Molecule-Based Magnets—An Overview. *MRS Bulletin* **2000**, *25*, 21.
- (4) Miller, J. S. Opportunities in Magnetic Materials. *Adv. Mater.* **1994**, *6*, 322.
- (5) White, R. M. Organic Molecular Soft Ferromagnetism in a FullereneC60. *Science* **1985**, *229*, 11.
- (6) Allemand, P.-M.; Khemani, K. C.; Koch, A.; Wudl, F.; Holczer, K.; Donovan, S.; Gruner, G.; Thompson, J. D. *Science* **1991**, *253*, 301.
- (7) Fujita, W.; Awaga; Kunio Room-Temperature Magnetic Bistability in Organic Radical Crystals. *Science* **1999**, *286*, 261.
- (8) Manriquez, J. M.; Yee, R. T.; Scott, M. R.; Epstein, A. J.; Miller, J. S. I., JOEL S. A Room-Temperature Molecular/Organic-Based Magnet. *Science* **1991**, *252*, 1415.
- (9) Takahashi, M.; Turek, P.; Nakazawa, Y.; Tamura, M.; Nozawa, K.; Shiomi, D.; Ishikawa, M.; Kinoshita, M. Discovery of a quasi-1D organic ferromagnet. *Phys. Rev. Lett.* **1991**, *67*, 746.
- (10) Mataga, N. Possible “ferromagnetic states” of some hypothetical hydrocarbons. *Theor. Chim. Acta* **1968**, *10*, 372.
- (11) Miller, J. S. Organic Magnets—A History. *Adv. Mater.* **2002**, *14*, 1105.
- (12) Esquinazi, P.; Spemann, D.; Hühne, R.; Setzer, A.; Han, K. H.; Butz, T. Induced Magnetic Ordering by Proton Irradiation in Graphite. *Phys. Rev. Lett.* **2003**, *91*, 227201.
- (13) Cervenka, J.; Katsnelson, M. I.; Flipse, C. F. J. Room-temperature ferromagnetism in graphite driven by two-dimensional networks of point defects. *Nat. Phys.* **2009**, *5*, 840.

- (14) Nair, R. R.; Sepioni, M.; Tsai, I. L.; Lehtinen, O.; Keinonen, J.; Krasheninnikov, A. V.; Thomson, T.; Geim, A. K.; Grigorieva, I. V. Spin-half paramagnetism in graphene induced by point defects. *Nat. Phys.* **2012**, *8*, 199.
- (15) Ferraris, J.; Cowan, D. O.; Walatka, V.; Perlstein, J. H. Electron transfer in a new highly conducting donor-acceptor complex. *J. Am. Chem. Soc.* **1973**, *95*, 948.
- (16) Coleman, L. B.; Cohen, M. J.; Sandman, D. J.; Yamagishi, F. G.; Garito, A. F.; Heeger, A. J. Superconducting fluctuations and the Peierls instability in an organic solid. *Solid State Commun.* **1973**, *12*, 1125.
- (17) Cl  ac, R.; O'Kane, S.; Cowen, J.; Ouyang, X.; Heintz, R.; Zhao, H.; Bazile, M. J.; Dunbar, K. R. Glassy Magnets Composed of Metals Coordinated to 7,7,8,8-tetracyanoquinodimethane: M(TCNQ)₂ (M = Mn, Fe, Co, Ni). *Chem. Mater.* **2003**, *15*, 1840.
- (18) Vickers, E. B.; Giles, I. D.; Miller, J. S. M[TCNQ]_y-Based Magnets (M = Mn, Fe, Co, Ni; TCNQ = 7,7,8,8-tetracyano-p-quinodimethane). *Chem. Mater.* **2005**, *17*, 1667.
- (19) Tengstedt, C.; de Jong, M.; Kanciurzevska, A.; Carlegrim, E.; Fahlman, M. X-Ray Magnetic Circular Dichroism and Resonant Photomission of V(TCNE)_x Hybrid Magnets. *Phys. Rev. Lett.* **2006**, *96*, 057209.
- (20) Prigodin, V. N.; Raju, N. P.; Pokhodnya, K. I.; Miller, J. S.; Epstein, A. J. Spin-Driven Resistance in Organic-Based Magnetic Semiconductor V[TCNE]_x. *Adv. Mater.* **2002**, *14*, 1230.
- (21) Ranganathan, A.; Heisen, B. C.; Dix, I.; Meyer, F. A triazine-based three-directional rigid-rod tecton forms a novel 1D channel structure. *Chem. Commun.* **2007**, 3637.
- (22) Ferlay, S.; Mallah, T.; Ouahes, R.; Veillet, P.; Verdaguer, M. A room-temperature organometallic magnet based on Prussian blue. *Nature* **1995**, *378*, 701.
- (23) H  hne, R.; Esquinazi, P.; Heera, V.; Weishart, H.; Setzer, A.; Spemann, D. The influence of iron, fluorine and boron implantation on the magnetic properties of graphite. *J. Magn. Magn. Mater.* **2008**, *320*, 966.

Acknowledgement

All praises to Almighty Allah, Who gave me the courage and strength to complete my doctoral research work and huge respect is for Holy Prophet (peace and blessings of Allah be upon him).

I am pleased to express my sincere gratitude, wholehearted appreciation to my advisor, Prof. Jong-Beom Baek for his guidance, kindness, encouragement and extremely helpful attitude throughout my tiresome doctoral research work, without his assistance and guidance the culmination of this project was almost a dream for me. My sincere thanks to my committee members, Prof. Myoung Soo Lah, Prof. Noejung Park, Prof. Joon Hak Oh and Prof. Hyung Joon Shin for their constant help and discussions with collaborative opportunities, their guidance will always help me in my future research work. Moreover, I would like to extend my heartfelt gratefulness to Prof. Jung-Woo Yoo (UNIST) and Prof. Kian Ping Loh (NUS, Singapore) for their fruitful discussion and guidance.

My very special thanks are to all CDCOF members. Especially I would like to mention, Dr. In-Yup Jeon who was very helpful right from the start of my carrier in UNIST, Ms. Seo-Yoon Bae who helped me to settle down in UNIST otherwise it would have been very hard task, Ms. Hyun-Jung Choi is superb human with extremely helpful attitude, Ms. Sun-Min Jung, she looks angry young girl but in reality she is very nice and kind hearted, Ms. Jeong-Min Seo is always ready to help me out, Mr. Seok-Jin Kim is a nice guy with helpful face and Mr. Ishfaq Ahmad, he joined our lab just recently. I would also like to express my thanks to former group members, Ms. Min-Jung Kim, Ms. Gyung-Joo Sohn and Ms. Yeon-Ran Shin for their help. I extend my thanks to Dr. Zhao and Dr. Palani for their scientific discussions. In short, their co-operation enabled me to overcome the problems which I faced during my research work.

In addition, I am very grateful to Mr. Muhammad Yousuf, Mr. Khaqan Shati, Mr. Muhammad Saleh and Mr. Mohsin in UNIST for their nice company all the time.

My special, cordial and whole hearted thanks to my family, parents, brothers and sisters, who always prayed for my success and bright future. Especially to my mother who always missed me during my

long period of study here. My special prayers for my late younger brother Mr. Suhail Mahmood (May Allah rest his soul in peace), he was always used to do my works in Pakistan.

I am highly obliged to my wife, Ms. Rabia Ibrahim, for her inexhaustible patience, inspiration, moral support and encouragement to finish my studies. Extreme love for my lovely son Mr. Rohaan Mahmood for giving me a lot of happiness in the tense situation and sleepless nights during my thesis writing and defense preparation.

Very special thanks to my friends, Prof. M. Tariq Mahmood (Korea University of Science and Technology), Dr. Mohib Ullah Shah (Brazil), Mr. Tariq Khan (China), Dr. Abdul Hameed (China), Dr. Rasool Khan (Peshawar) , Dr. Muhammad Imran (Peshawar) and Dr. Zahid for their unlimited moral support.

Finally, I am thankful to all UNIST faculty and staff members for providing me a research friendly environment and providing each and every facility for the completion of my project.

Javeed Mahmood

List of publications

1. **Mahmood, J.**; Lee, E. K.; Jung, M.; Shin, D.; Jeon, I.-Y.; Jung, S.-M.; Choi, H.-J.; Seo, J.-M.; Bae, S.-Y.; Sohn, S.-D.; Park, N.; Oh, J. H.; Shin, H.-J.; Baek, J.-B. Nitrogenated holey two-dimensional structures. *Nat. Commun.* 2015, 6, 6486. (Highlighted in CNBC, KBS, Chosun Daily and more than 333 Global News Hits).
2. **Mahmood, J.**; Kim, D. W.; Jeon, I.-Y.; Lah, M. S.; Baek, J.-B. Scalable synthesis of pure and stable hexaaminobenzene trihydrochloride, *Synlett*, 2013, 24, 0246-0248.
3. Jeon, I.-Y.; Shin, Y.-R.; Sohn, G.-J.; Choi, H.-J.; Bae, S.-Y.; **Mahmood, J.**; Jung, S.-M.; Seo, J.-M.; Kim, M.-J.; Chang, D.-W.; Dai, L.; Baek, J.-B. Edge-carboxylated graphene nanosheets via ball milling, *PNAS*, 2012, 109, (15), 5588–5593.
4. **Javeed Mahmood**, Minbok Jung, Dongbin Shin, Hyun-Jung Choi, Jeong-Min Seo, Jung Min Park, Dongwook Kim, Jung-Woo Yoo, Myoung Soo Lah, Noejung Park, Hyung-Joon Shin, Jong-Beom Baek, 2D C₃N structure obtained from carbonized single crystals, submitted.
5. **Javeed Mahmood**, Hyun-Jung Choi, Gyung-Joo Sohn, Sun-Min Jung, Jeong-Min Seo, Jungmin Park, Jung-Woo Yoo, and Jong-Beom Baek, Fe-Cocooned C₂N-h₂D structures as efficient oxygen reduction catalysts. *In process of submission*.
6. **Javeed Mahmood**, Sun-Min Jung, Seok-Jin Kim, Jungmin Park, Jung-Woo Yoo, and Jong-Beom Baek, C₂N-h₂D network polymer-encapsulated cobalt oxide catalyst for hydrogen evolution, *Chemistry of Materials*, accepted.
7. **Javeed Mahmood**, Jungmin Park, Hyun-Jung Choi, Jeong-Min Seo, Jung-Woo Yoo, Jong-Beom Baek, Organic ferromagnetism from self-polymerized TCNQ, submitted.
8. **Javeed Mahmood**, Eun Kwang Lee, Joon Hak Oh, Jong-Beom Baek, Synthetically designed polymer with extremely high charge carrier mobility, manuscript in process of preparation.

